ABSORPTION SPECTROSCOPY OF RUBIDIUM IN AN ALKALI METAL DISPENSER CELL AND BLEACHED WAVE ANALYSIS

THESIS

JAMES M. ROSENTHAL, 2nd Lt, USAF

AFIT-ENP-MS-15-M-102

DEPARTMENT OF THE AIR FORCE

AIR UNIVERSITY

AIR FORCE INSTITUTE OF TECHNOLOGY

Wright-Patterson Air Force Base, Ohio

AFIT-ENP-MS-15-M-102

ABSORPTION SPECTROSCOPY OF RUBIDIUM IN AN ALKALI METAL DISPENSER CELL AND BLEACHED WAVE ANALYSIS

THESIS

Presented to the Faculty

Department of Engineering Physics

Graduate School of Engineering and Management

Air Force Institute of Technology

Air University

Air Education and Training Command

In Partial Fulfillment of the Requirements for the

Degree of Master of Science in Applied Physics

James M. Rosenthal, BA

2nd Lt, USAF

March 2015

AFIT-ENP-MS-15-M-102

ABSORPTION SPECTROSCOPY OF RUBIDIUM IN AN ALKALI METAL DISPENSER CELL AND BLEACHED WAVE ANALYSIS

James M. Rosenthal, BA

2nd Lt, USAF

Committee Membership

Glen P. Perram, PhD
Chair

Lt Col Anthony L. Franz, PhD
Member

David E. Weeks, PhD
Member

AFIT-ENP-MS-15-M-102

Abstract

An absorption spectrum of a rubidium alkali metal dispenser (AMD) cell was obtained in order to determine the system's suitability for use in a diode pumped alkali laser (DPAL) and use in high-temperature spectroscopic studies. The AMD produced a concentration of $3.65 \pm 0.16 \times 10^{10}$ cm^{-3}, which is in the ideal range for Beer's Law region absorption spectroscopy, but too low to make a high-power DPAL in a 10 cm cell with a poor Q resonator. Before AMDs can be used to determine pressure broadening and shifting coefficients, issues concerning contamination and producing rubidium vapor at pressure must be resolved.

A separate portion of this study focused on a sealed rubidium Pyrex cell with neon buffer gas. A continuous wave titanium sapphire beam was focused into the cell with various lenses to maximize pump intensity through the cell. Images were taken of the side fluorescence of the cell to determine the bleached regions. The total horizontal propagation of the bleached region for each image was proportional to the pump laser power and the inverse of the rubidium vapor density. Disparity between the bleached volume estimated from the beam parameters and the theoretical bleached volume suggested the beam intensity had a strong radial dependence. When the pump wavelength was changed, visible side fluorescence occurred in regions where the laser intensity was at least 0.125 times the saturation intensity and therefore not in the regions where the decay was determined by Beer's Law.

Acknowledgements

I would like to thank Dr. Glen Perram for all of his advice and guidance through my research process, and Dr. Christopher Rice and Dr. James Williamson for all their hours of assistance in the lab. I would also like to thank Michael Ranft and Gregory Smith for lending and fixing equipment I needed, and fellow students Wooddy Miller and Paul Moran for partnering with me at various stages of the data collection. Finally, I have to thank my parents and my sister for all of their support and advice.

Table of Contents

Page

List of Figures

ABSORPTION SPECTROSCOPY OF RUBIDIUM IN AN ALKALI METAL DISPENSER CELL AND BLEACHED WAVE ANALYSIS

I. Introduction

Due to its high output power, the diode pumped alkali laser (DPAL) has recently emerged as a strong candidate for a high-powered laser for military applications. The diode pumped alkali laser is a three level laser system consisting of the transitions between the ground states and the first excited states of an alkali metal vapor [1]. Interaction between electronic spin and orbital angular momentum introduces fine structure splitting in the excited state, resulting in two separate excited states with a slight energy disparity (henceforth referred to as the quantum defect). The interaction between electronic angular momentum and nuclear spin also introduces hyperfine splitting, but these peaks are very close to one another and will usually blend together in a pressure-broadened DPAL system. For a laser with an alkali metal as the gain medium, the theoretical quantum efficiency is around 98%, higher than most high power lasers. The transitions are also close to the frequencies of existing diode technology, so high-power pump sources are easily obtainable for these systems. In a rubidium DPAL system, the alkali metal is optically pumped from the ground state to the upper (J = 3/2) first excited state (this is known as the D_2 transition). A buffer gas (often a rare gas or a hydrocarbon) causes the alkali metal to spin-orbit relax to the lower (J = 1/2) first excited state. The alkali metal vapor then lases back to the ground state (this is known as the D_1 transition). For rubidium, the D_2 line is near 780 nm and the D_1 line is near 795 nm. For a DPAL to lase, the optical pump must bleach the entire alkali metal cell, that is, excite the medium

such that the population inversion reaches zero. After the losses incurred in this process, any excess pump power results in system gain.

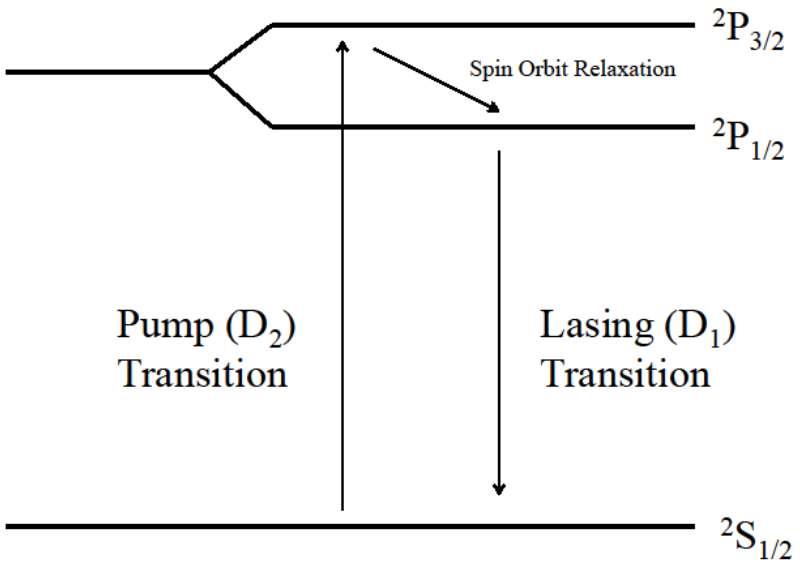

Fig. 1. Transition model for a diode pumped alkali laser.

This laser system was first demonstrated by Krupke *et al.* in 2003 [1]. Krupke used rubidium as the alkali metal sample and 525 torr of helium and 75 torr of ethane as the buffer gases. The experiment involved heating a metallic sample of rubidium to around 120^{o}C to obtain a concentration on the order of 10^{13} molecules/cm^3 of rubidium vapor via evaporation. Krupke pumped the system with a continuous wave (CW) titanium sapphire source and obtained a relatively high slope efficiency of 54%. Hydrocarbon buffer gases result in very high spin orbit relaxation rates for alkali metal transitions, and therefore require adding lower partial pressures of buffer gas allowing

lower pressure-broadening of the rubidium spectral peaks than those of the rare gases, thereby maximizing the gain. However, hydrocarbons react with alkali metals to produce hydride precipitates and soot, which cloud cell windows and interfere with the optical path. For these reasons, there has been some investigation into exclusive use of noble gases as DPAL buffer gases. In 2008, Wu *et al.* demonstrated a comparable DPAL system using only helium as the buffer gas and demonstrated a slope efficiency of 21% [2]. The system was further characterized by Sulham in 2010 using a pulsed pump source, determining the ideal temperature of a rubidium DPAL cell 12.7 cm long to be approximately 120^{o}C [3].

The DPAL concept has increasingly been considered as a suitable candidate for the Airborne Laser (ABL) program [3]. The lasers most suitable for the ABL program are the ones capable of producing powers on the order of megawatts and the ones that produce minimal heat and contaminants. The original laser system used by ABL was the Chemical Oxygen Iodine Laser (COIL), which utilized the energy from the chemical reaction between oxygen and iodine to pump the required energy transition [3]. Although this system was capable of producing output powers of the order of megawatts, the laser posed two issues. The first issue concerns the requirement of chemical reagents aboard the aircraft needed to power the system; when the chemicals were exhausted, the laser could no longer be used until the aircraft landed and was resupplied. The second issue is that of transportation of reactive chemicals to and across the battlefield, which could pose a danger if a leak were to occur. Another possibility for the ABL is the Diode Pumped Solid State Laser (DPSSL) [3]. This system does not have the chemical issues of the COIL, but there are difficulties in preventing a solid system from overheating. Upon their

discovery, DPALs have emerged as another suitable candidate for the ABL. DPALs can produce the high intensities needed and only require electric energy [3]. DPALs still pose maintenance issues, as alkali metals are highly reactive and the aforementioned precipitates will build in the cells and require frequent cleaning and maintenance. The use of reactive solid alkali metal would also pose a risk if a leak were to occur on board an aircraft.

A possible solution to this problem would be to replace the solid alkali metal with an alkali metal dispenser (AMD). An AMD is a narrow strip of an alkali salt such as Rb_2CrO_4 with an embedded conducting resistor such as nickel wire. When a current travels across the resistive wire, it heats to approximately 700^{o}C, providing the thermal energy for an oxidation-reduction reaction in the salt, causing it to emit an alkali metal vapor. Alkali salts are stable and will not react at atmospheric temperatures and pressures, so none of the safety measures needed with pure solid alkali metal would be required.

AMDs can also be used to further characterize alkali metal spectra in non-laser systems. In past studies, AMDs have been used exclusively at near-vacuum pressures [4] [5] [6]. The AMD system's performance must be evaluated at typical DPAL operating pressures before the system can be used to obtain a pressure-broadened spectrum or create a DPAL with a buffer gas, but the system also has applications in Doppler spectroscopy. The nature of an AMD setup allows the alkali salt to be heated independently of the cell temperature, making such an apparatus ideal for studies concerning alkali metal vapors of varying temperatures. Use of an AMD for alkali metal vapor would also allow for a more detailed characterization of a DPAL system. Previous

DPAL systems using liquid alkali metal have had alkali metal vapor concentration dependant on the vapor pressure, which is a function of temperature, whereas with an AMD, alkali metal density and cell temperature can be controlled as two independent variables, allowing an optimal temperature for a given vapor density and given gain cell to be found.

The suitability of alkali metal dispensers as the alkali metal vapor source for a DPAL can be tested by obtaining spectra from a rubidium AMD at vacuum and at pressure. Assuming sufficient alkali metal vapor concentrations maintained for long enough periods of time at a wide range of buffer gas pressures, a rubidium AMD optically pumped laser is to be designed and optimized. Assuming the other case with insufficient alkali metal vapor concentrations, an alternate, conventional sold alkali metal cell with buffer gas is to be substituted for the AMD system; laser power output and absorption spectra from this alkali metal cell is to be characterized and compared to that of the AMD results.

The second half of this study involved taking images of side fluorescence in standard (non-AMD) alkali metal cells. For a DPAL to lase, the entire length of the gain medium must be bleached, and this only occurs when certain conditions are met in regards to temperature, pump power, spot size, and wavelength. A collection of images of pump propagation through an open alkali metal cell would reveal much about the transmission and about absorptive and emissive processes of photons in a DPAL.

II. Rubidium Doppler-Broadened Spectroscopy and Rubidium Production in 10 torr Helium in an Alkali Metal Dispenser Cell

Background

Fine structure arises from the interaction between the electronic spin and the electronic orbital angular momentum [7] [8]. Total electronic angular momentum is given by $J = L + S$, where L is the orbital angular momentum and S is the electronic spin, which will always be ½ in a one-electron system. The spin and orbital angular momenta can be either parallel or antiparallel, with all of the possible J values at intervals of 1 from $J = L - S$ to $J = L + S$.

Hyperfine structure arises from the interaction between the nuclear spin and the total electronic angular momentum. For each fine structure line, there are several different hyperfine lines for different nuclear spins. The total angular momentum F is given by $|J - I| \leq F \leq |J + I|$, where I is the nuclear spin. The selection rules dictate that $\Delta F = \pm 1, 0$, allowing up to three transitions for every possible ground state (the initial F state is designated F'' and the final F state is designated F').

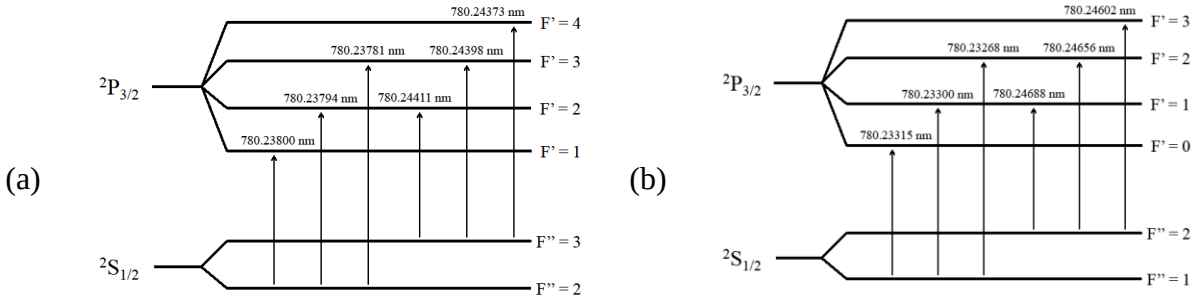

Fig. 2. Possible hyperfine transitions of the D_2 line for rubidium [9] [10]. (a) Possible initial and final states and transition wavelengths of ^{85}Rb. (b) Possible initial and final states and transition wavelengths of ^{87}Rb.

Rubidium exists in nature as two stable isotopes, ^{85}Rb with a natural abundance of 0.72, and ^{87}Rb with a natural abundance of 0.28. For ^{85}Rb, I = 5/2, allowing six possible transitions for the D_2 line, from F'' = 2, 3 at $^2S_{1/2}$ to F' = 1, 2, 3, 4 at $^2P_{3/2}$. For ^{85}Rb, I = 3/2, also allowing six possible transitions for the D_2 line, from F'' = 1, 2 at $^2S_{1/2}$ to F' = 0, 1, 2, 3 at $^2P_{3/2}$. The wavelengths for each of these twelve transitions are given in Table 1 in Appendix A. At near vacuum pressure, the Doppler broadened rubidium absorption spectrum is given by Beer's Law. Pitz *et al.* [8] give Equation 1 for the Beer's Law absorption cross section for each hyperfine component,

$$\sigma_{hfs} = \left(\frac{g_{J'}}{g_{J''}}\right)\left(\frac{\lambda^2}{8\pi}\right) A_{(^2P_{3/2}\rightarrow{}^2S_{1/2})} S_{F''\rightarrow F'} g(\nu) f_{F''} f_{iso}, \tag{1}$$

where g_J is the electronic angular momentum degeneracy for the upper and lower states, λ is the transition wavelength from Table 1, A is the spontaneous emission Einstein coefficient, $S_{F''\rightarrow F'}$ is the hyperfine line strength, $g(\upsilon)$ is the Doppler lineshape, f_{iso} is the isotope relative natural abundance, and $f_{F''}$ is the distribution of ground F states, given by their degeneracies and the Maxwell-Boltzmann energy distribution. The product of the cross section with the cell length and the rubidium concentration gives the unitless quantity absorbance. The values of the necessary parameters for rubidium were taken from the literature [9] [10]. For temperatures of around 120^{o}C, the Doppler width of the transition is 0.00117 nm. This indicates that the transitions of the same isotope sharing the same lower (F'') state exceed their respective spacing by about an order of magnitude such that the individual peaks cannot be resolved. Therefore, a spectrum of the twelve transitions appears as only four peaks.

When a buffer gas is added to the cell, collisions between the molecules cause the system to become pressure-broadened, which results in a Lorentzian lineshape, which is often much wider than the Doppler broadening at near-atmospheric pressures. For the rubidium D_2 transition at 120^{o}C, the Lorentzian FWHM becomes wider than the Doppler FWHM at 31.2 torr of helium and above, so homogeneous broadening will dominate the system. Therefore, for the pressure-broadened rubidium system in this study, all twelve hyperfine lines appeared to be one peak. The pressure broadening rate for the rubidium D_2 line is 18.9 MHz/torr for helium [11].

Alkali metal dispenser systems are most commonly used for deposition of alkali metal to create photosensitive surfaces under vacuum conditions [4], but they also have spectroscopic applications. An AMD consists of a strip of alkali salt (usually Rb_2CrO_4), a reducing agent, and a conducting resistive wire that heats when subjected to an applied current. When the current heats a sample to about 700^{o}C, the AMD produces gaseous alkali metal. This process is more efficient than evaporating and collecting pure solid alkali metal, but this method poses other issues; gaseous contaminants such as CO_2, CO, N_2, and H_2 may also be produced when the current is applied [4]. These species may react with the cathode surface, necessitating the use of a getter (often a zirconium-aluminum alloy) to deplete contaminant concentrations, but for rubidium spectroscopy experiments, such measures are unnecessary as contaminant concentrations are not high enough to pressure-broaden or otherwise have a significant effect on the alkali metal spectral lines. Another possible source of contamination is the stainless-steel chamber that houses the AMD, as stainless-steel outgasses hydrogen gas at a rate of approximately 10^{-12}

torr/s/cm^2 [12]. Hydrogen gas reacts with rubidium vapor to form rubidium hydride (RbH).

Previous studies of alkali metal dispensers only observed operation at vacuum, and most reported exponential decreases in alkali metal vapor concentration with respect to time and reduced capacity of the AMD strips to produce alkali metal vapor after prolonged use. A study by della Porta *et al.* demonstrated the alkali metal generation rates of a cesium AMD by ionizing the emitted vapor and observing the induced current [4]. The cell was heated at 375^{o}C overnight while connected to a vacuum system to eliminate contaminant gases. The results indicated twice the rate of alkali metal vapor production at 850^{o}C than at 750^{o}C and showed that after two to three hours, alkali metal vapor production had fallen by an order of magnitude. A different study by Eichenbaum *et al.* also using a cesium AMD instead determined the alkali metal vapor production rate to be nearly constant indefinitely, only depleting after 16 hours of use for a sample at 1200^{o}C, the highest temperature attained in the study [5]. An experiment by Moore *et al.* used a rubidium AMD with the current applied in 3-second pulses and a 20-second cool down between pulses [6]. Like the previously cited works, Moore observed a linear rise in alkali metal vapor production when the current was applied and an exponential decay in alkali metal vapor population when the current was switched off.

Output laser power is a function of gain cell temperature. The traditional DPAL model uses a heater to melt solid alkali metal and produce a vapor by means of evaporation. Because the number density of the alkali metal vapor is also a function of temperature, previous studies have not been able to obtain an accurate characterization of an alkali metal vapor based on temperature alone. In 1968, Gallagher *et al.* investigated

the effects of temperature on rubidium and cesium collision cross sections using a two-temperature system; a metal sample was heated to produce the alkali metal vapor in one chamber, connected to a chamber at a different temperature for mixing with an inert gas [13]. A similar concept could be used to test DPAL performance with alkali metal vapor concentration independent of temperature. Use of an AMD would be ideal in this case, as the cell temperature does not determine alkali metal vapor concentration. These results could be compared against the ideal DPAL temperature found in Sulham's study to determine if the optimal temperature for power output for a given gain cell is different when the alkali metal vapor density is controlled as a separate variable [3].

According to Krupke, for a DPAL cell of length on the order of centimeters, the ideal rubidium vapor density is on the order of 10^{13} cm^{-3} [1]. At this concentration, the gain is high enough to bleach the cell and result in single pass lasing. An AMD cell that could reach this density would be a strong candidate for use in a DPAL. Lower concentrations on the order of 10^{10} cm^{-3} would be in the Beer's Law domain, where the intensity would be well below the saturation intensity, indicating that the AMD system is well suited for spectroscopic studies, such as high-temperature kinetics and determining pressure-broadening and shifting rates of buffer gases. Determining the maximum attainable alkali metal vapor concentrations of an AMD system would determine which of these areas of study the system would be better suited for.

Experimental Setup

The alkali metal dispenser chamber was mounted on a breadboard. This system consisted of two primary chambers, an upper chamber and a lower chamber. The ends of

the alkali metal dispenser strip were tightened onto two conducting rods, which were sealed into the larger lower chamber such that any emitted rubidium vapor would convect into the upper chamber and the optical path of a pump laser. The larger lower chamber was connected to two valves: one to a Varian Turbo-V 250 vacuum pump and one to a helium supply. The system was wrapped in a Briskheat BIH701040L heating pad with a T-type thermocouple, both connected to a Watlow EZ-ZONE PM Express controller, and the system was covered in insulating material.

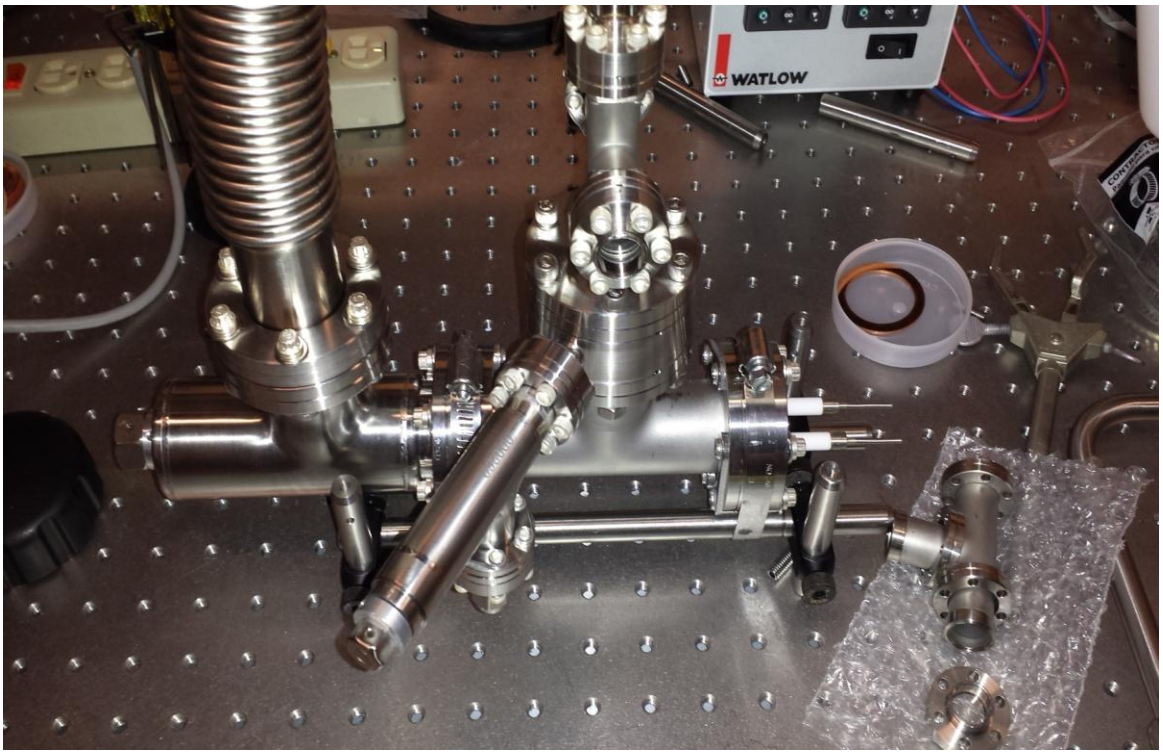

Fig. 3. Image of the alkali metal dispenser chamber with the heater and insulation removed. The center chamber was connected to the Varian Turbo-V 250 vacuum pump by the valve on the left, and the window for the optical path was directly above the AMD location. The two conducting metal rods on the right were attached to an Agilent Technologies N5744A power supply.

A photograph of the AMD system was shown in Figure 3 and diagrams of the AMD system from three different perspectives were shown in Figure 4. All figures were

shown without the heating pad or insulation in order to show a better view of the apparatus.

(a)

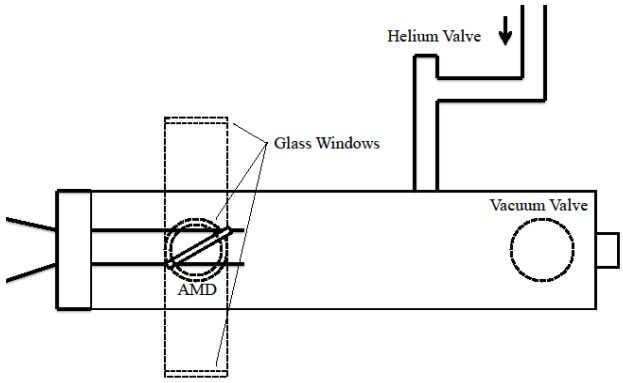

(b)

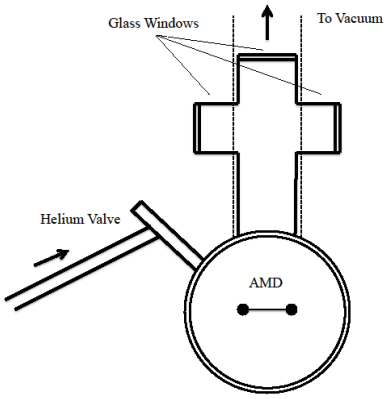

(c)

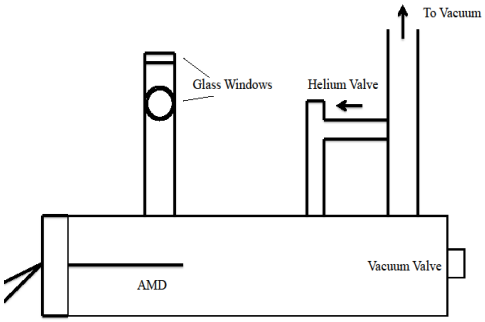

Fig. 4. Diagram of the AMD system. The AMD strip was inserted into the center of the lower chamber attached to a pair of conducting metal rods connected to the power supply. The lower chamber was connected to an optical path, a vacuum pump, and a helium valve. (a) Bird's eye view. (b) Front view. (c) Profile view.

To produce rubidium vapor under near vacuum conditions, an Agilent Technologies N5744A power supply was connected to the AMD and set to 7.50 amperes at 1.5 volts (always set such that current was the limiting factor). After each new AMD was attached to the metal strips, this power was applied for 30 seconds with the chamber exposed to the vacuum pump in order to remove any potential contaminants on the strip. While still connected to the vacuum, the cell was then set to 120^{o}C for an overnight bake out. Afterwards, the chamber remained sealed until exhaustion of each respective rubidium AMD, which was about 20 minutes of use each. An MKS Baratron 690A11TRA pressure meter and an Agilent Technologies XGS-600 pressure meter were used to verify that the pressure within the cell reached a pressure on the order of 10^{-6} torr. An additional MKS Baratron 690A11TRA pressure meter was connected by the helium valve for the experiments at higher pressure.

The nickel wire in the AMD acted as a resistor, producing temperatures of around 700^{o}C when subjected to the current from the power supply. Running 7.50 amperes through the strip produced enough thermal energy for the salt to undergo the oxidation-reduction reaction that released rubidium vapor. This heat caused the alkali metal dispenser strip to glow a bright orange via Planckian thermal radiation as seen in the image in Figure 5.

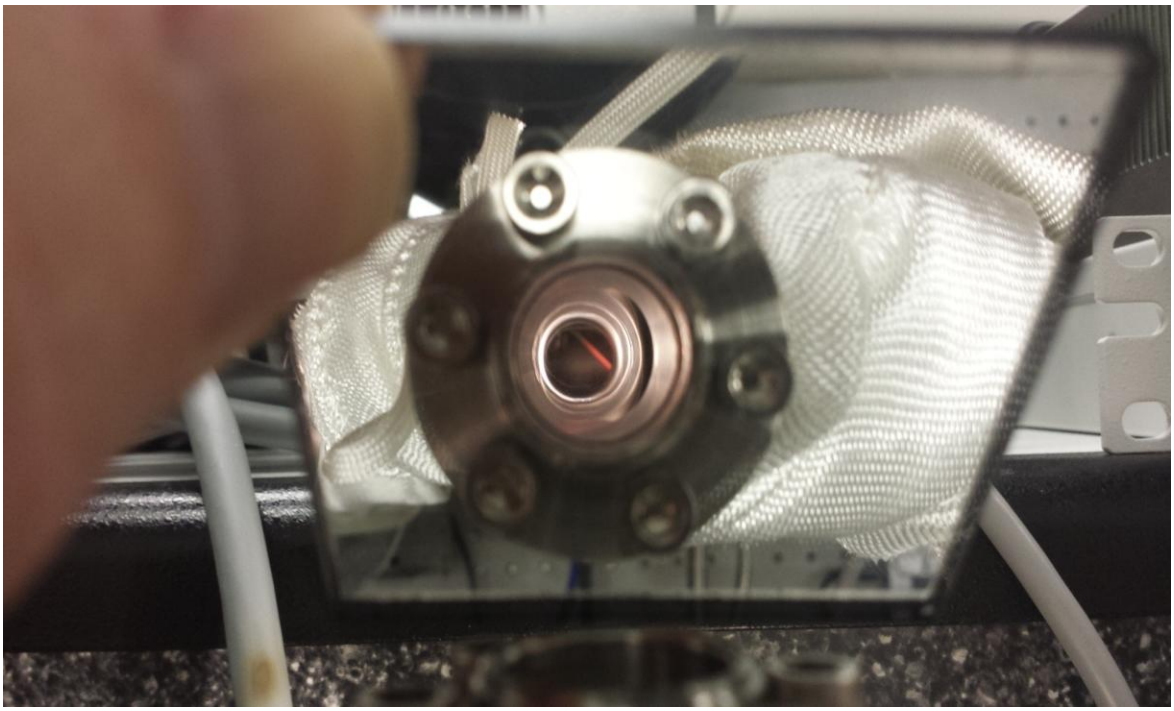

Fig. 5. The rubidium chromate AMD inside the chamber as seen from the top window. The cell was pumped to vacuum and a current of 7.5 amperes was run through the AMD strip. Due to its resistance, the AMD glowed a bright orange color as it reached temperatures of around 700^{o}C.

The hyperfine lines were found using laser absorption spectroscopy with a Matisse TX tunable continuous wave titanium sapphire laser. The Matisse had a tuning range from 700 nm to 990 nm, a maximum power of 1.4 W, and a spectral linewidth of 10 MHz. The beam propagated through a sapphire window, directing a much weaker reflection into a High Finesse WS-7 wavemeter. A series of Thor Labs PF10-03-P01 high reflecting mirrors directed the laser into a beam splitter. One half of the beam propagated through the alkali metal dispenser cell and then to a Hamamatsu S2281-01 photodiode. The other half of the beam propagated directly to a photodiode to obtain baseline intensity readings for normalization. Both of the photodiodes were connected to Hamamatsu C9329 preamplifiers set to the middle setting, which were connected to

Stanford Research Systems SR350 lock-in amplifiers, which were connected to a chopper placed in the beam path before the beam splitter.

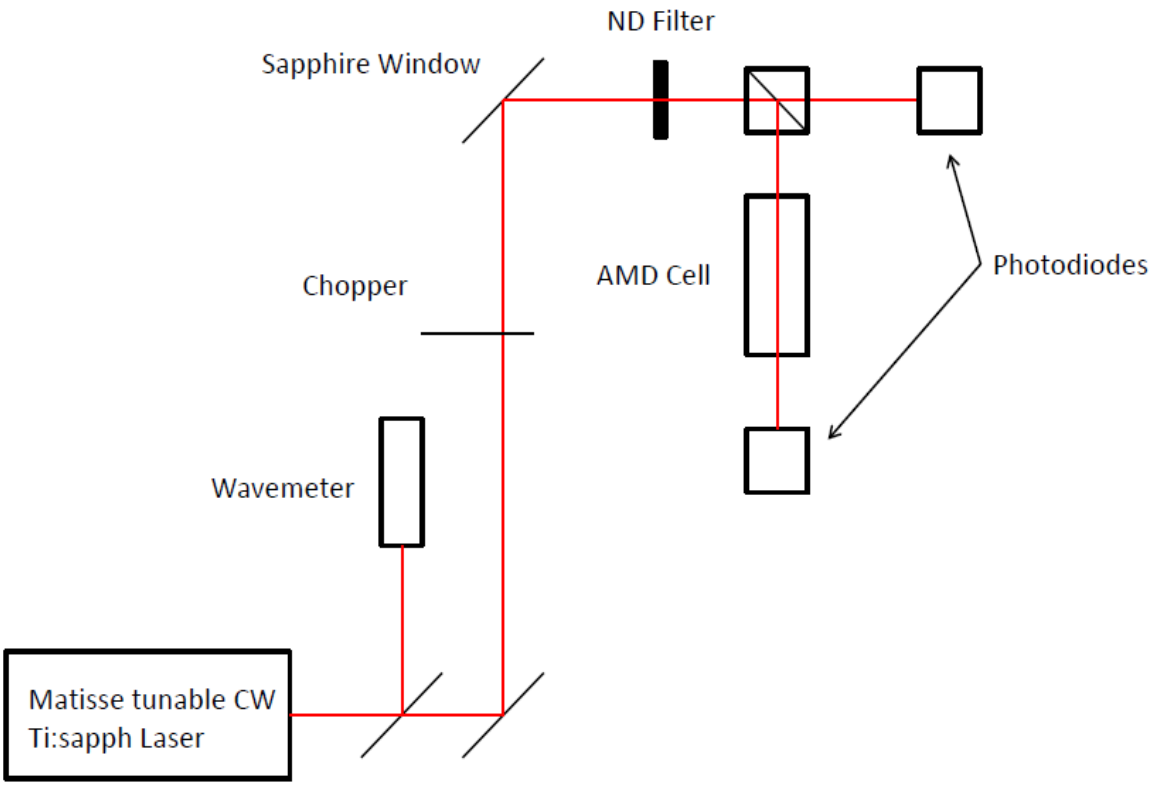

Fig. 6. Apparatus for obtaining the rubidium absorption spectrum. The beam from the Matisse tunable CW Titanium Sapphire laser was measured by a High Finesse WS-7 wavemeter. The second surface reflection of the beam was taken from a sapphire window and then the beam travelled through a neutral density filter for a total attenuation of approximately $10^{6.5}$. The beam was then split before two Hamamatsu photodiodes, with one half of the beam travelling through the rubidium cell.

The Hamamatsu photodiodes returned a nonlinear voltage response for incident intensities of over 10 mW/cm^2. To keep the beam intensity from exceeding this limit, a

number of measures were taken to lower the incident intensity on the detector. The Matisse was set to about 800 mW for all absorption spectrum measurements in this portion of the study. One of the high reflecting mirrors in the beam was replaced with a sapphire window, with an iris in place such that only the second surface reflection propagated through the AMD cell. A neutral density (ND) filter was also placed in the beam path, reducing the beam power by approximately 6.5 orders of magnitude; the resulting laser intensity was low enough for the photodiode voltage to be proportional to the incident laser intensity.

The laser was repeatedly tuned over the D_2 wavelength at approximately 50 MHz/s. Each scan required about 2 minutes. The short scan time was important because quick degradation of rubidium concentration within the cell introduced a temporal variable to the observed absorption. The dependence on time had to be minimized in order to obtain a valid absorption spectrum as function of pump frequency alone. At each spectral peak, fewer photons would propagate through the rubidium vapor, and this data would be observed as a decrease in intensity incident on the photodiode and the data was saved with respect to the wavelength measured from the wavemeter.

For the scans taken at higher pressures, first an initial voltage run and overnight bake out were carried out with each new rubidium AMD. Next the helium valve was opened to allow the chamber to reach the desired pressure, and then was sealed off. The rubidium was then introduced to the cell by running current through the AMD for 1 to 10 minutes at a time and a scan was run with the Matisse with the photodiode setup to detect any alkali metal absorption lines. This procedure was repeated at various helium

pressures and at various currents to determine the effect of these parameters on rubidium vapor concentration.

Results

AMD was subjected to a 7.5 ampere current at 1.5 volts for 5 minutes under vacuum conditions, and the cell temperature was set to 100^{o}C. A scan of the tunable Ti:Sapph laser lasting about 2 minutes over the rubidium D_2 line produced the absorption spectrum given in Figure 7. The scan was taken at low background pressure on the order of 10^{-6} torr (this pressure does not include the partial pressure of the rubidium or any other species introduced by the AMD), therefore Doppler broadening dominated the spectrum, with a width of 0.00117 nm. The peaks had FWHM values of around 600 MHz, which was not small enough to resolve the peaks between the final F states of the hyperfine transitions. Therefore, each of the four peaks in Figure 7 were actually three separate, closely-spaced peaks, one for each of the $\Delta F = 0, \pm 1$ branches. Fewer photons reached the detector for absorbances of greater than 2.5, resulting in noisy peaks for the ^{85}Rb features. The best SNR was obtained for the ^{87}Rb features with $F'' = 1$.

This observed absorption spectrum was compared to a theoretical model from Equation 1 plotted at the frequencies given in Table 1. All the values for physical parameters of the model were taken from the literature, and only the rubidium concentration (n) was unknown. The value for n was varied and matched with the data such that the smallest peak with the best SNR (^{87}Rb at $F'' = 1$) for the theoretical model matched that of the experimental model. With this value applied to the equation, the model also matched the ^{87}Rb peak at $F'' = 2$, confirming that the model was accurate.

The recorded values of the ^{85}Rb peaks were less than the predicted values due to the poor signal-to-noise ratio in the detectors at very low incident intensities. There was also a shift of approximately 60 MHz (corrected in Figure 7) between the observed and theoretical values, which was within the reported wavemeter uncertainty of 60 MHz.

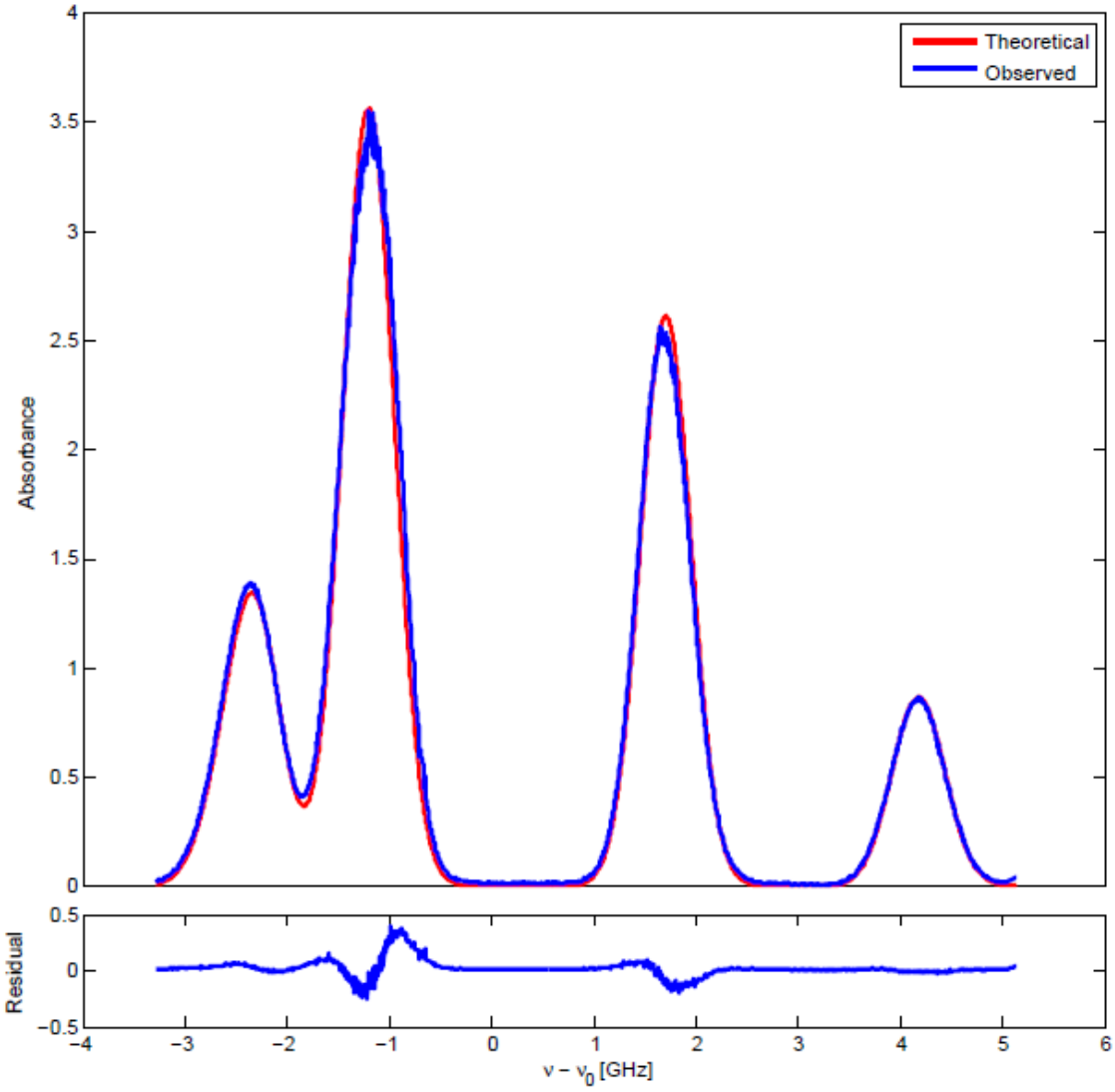

Fig. 7. The observed absorption spectrum of the D_2 line of rubidium in blue and the corresponding theoretical model in red for ν_0 = 384.23 THz. The features were Doppler-broadened with widths of 600 MHz. Each of the four peaks here consisted of three separate peaks for $\Delta F = 0, \pm 1$. Since both ^{87}Rb peaks matched the expectation, the model was accurate. The actual and theoretical wavelength values differed by about 60 MHz, which was within the uncertainty of the wavemeter.

The theoretical model fit the data with an R^2 value of 0.9925 and corresponded to a rubidium concentration of $n = 3.65 \pm 0.16 \times 10^{10}$ cm^{-3}, which indicates that the AMD system would be better suited for high-temperature kinetics spectroscopic studies than for making a DPAL. Krupke's results suggested that n should be at least on the order of 10^{13} cm^{-3} to achieve threshold with only a single or double pass [1], and the AMD system's concentration result was too small to achieve a slope intensity around 50% with a poor Q resonator (a higher Q resonator results in losses and therefore poor gain).

Several scans at near-vacuum pressure were run under various other conditions. When the cell underwent a Matisse scan while the AMD current was still running, the increase in rubidium density resulted in a transmission too low below the detection limit of the photodiodes. When the current ceased, the spectrum almost immediately returned to a spectrum comparable to that of Figure 7. In most cases the rubidium vapor would disappear from the cell within an hour of running a short burst of current through the AMD, a finding which was consistent with the times reported in the previous AMD studies [4] [5] [6].

The helium valve was opened enough to let in 769 torr of helium, enough needed for the spin-orbit relaxation rate necessary for lasing. After running the AMD for 5 minutes, a Matisse scan of the cell showed a flat spectrum with no pressure-broadened or Doppler-broadened rubidium features. A visual verification of the chamber at pressure with a 7.5 ampere current indicated that the AMD strip gave off no visible thermal radiation as it had done under vacuum conditions.

The current on the power supply for the AMD circuit was raised by several amperes (the voltage was also adjusted such that current was always the limiting factor). When the current increased, the previously observed orange glow became visible again. The pressure was adjusted to several levels between 0 and 100 torr, and at each pressure, the current required to produce the equivalent visible thermal radiation as produced under vacuum conditions was recorded. Figure 8 shows that as pressure increased in the cell, the differential of current required to maintain the same AMD temperature decreased.

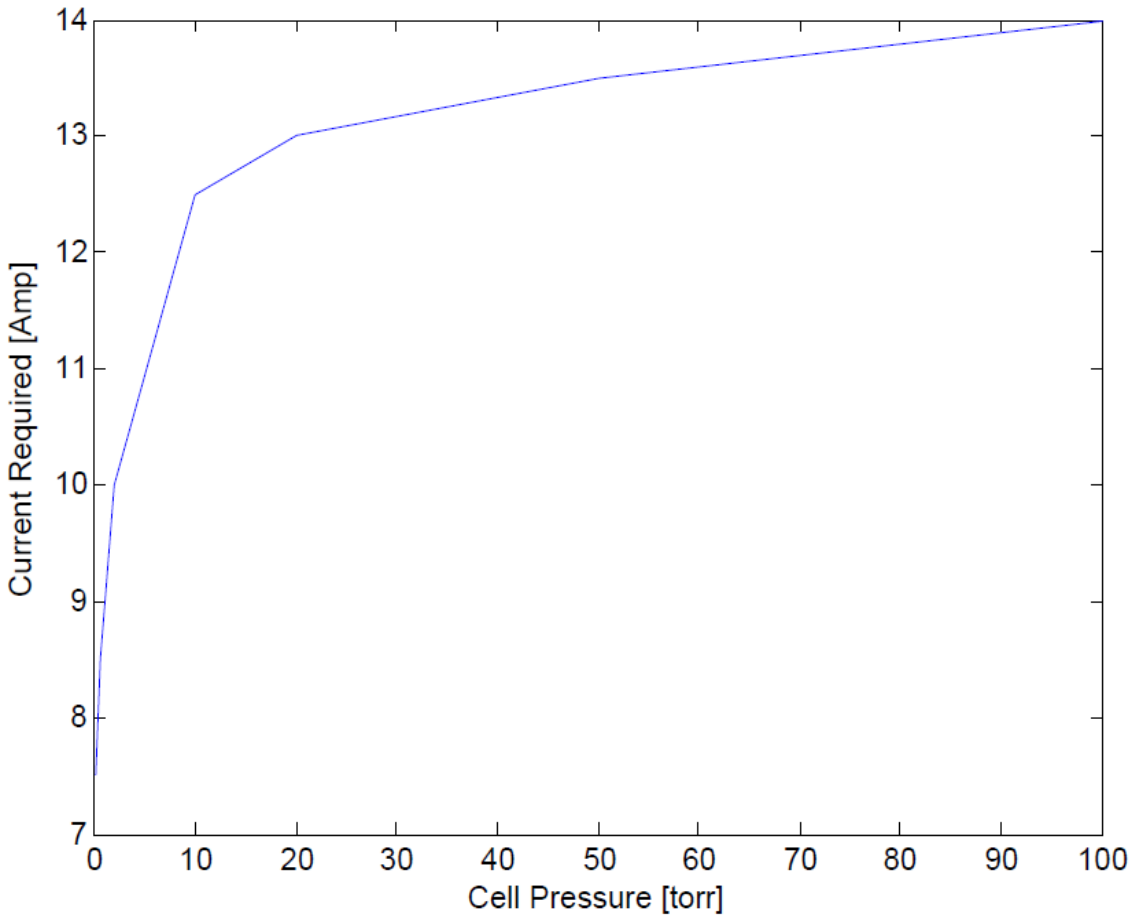

Fig. 8. The applied current required to reach the optimal thermal radiation in the AMD at each helium pressure in the AMD cell. The required current scaled logarithmically with the cell pressure, as the first several torr required several amperes to compensate, but the next 100 torr only required a few additional amperes to compensate.

100 torr helium was added to the cell and a 14 ampere current was run through the AMD. Despite confirming beforehand that the AMD was emitting visible thermal radiation, a Matisse scan indicated no discernible rubidium spectral features. Several additional measures were taken in an attempt to produce a rubidium spectrum under helium pressure. The current was run through the AMD under vacuum pressure and then 1 torr helium was added to the cell afterwards; although the Doppler-broadened features were apparent under vacuum conditions when the Matisse was tuned to line center, the features immediately disappeared upon the introduction of any helium to the chamber. A Matisse scan was run with 13 amperes of current still running through the AMD, at 10 torr helium; peak absorbance of 2 was observed in the spectrum, but the absorption features immediately disappeared when the power to the AMD was turned off. This procedure was repeated at 14 amperes and 100 torr, but no spectral features were observed even when the scan was taken when the current to the AMD was still being applied. The helium valve most likely introduced reagents such as oxygen, which quickly reacted with all the rubidium.

After the use of many AMD strips, the amount of rubidium vapor in the chamber would diminish more quickly than it had previously (under Doppler conditions). Figure 9 shows the drop in rubidium absorption at the beginning of the study.

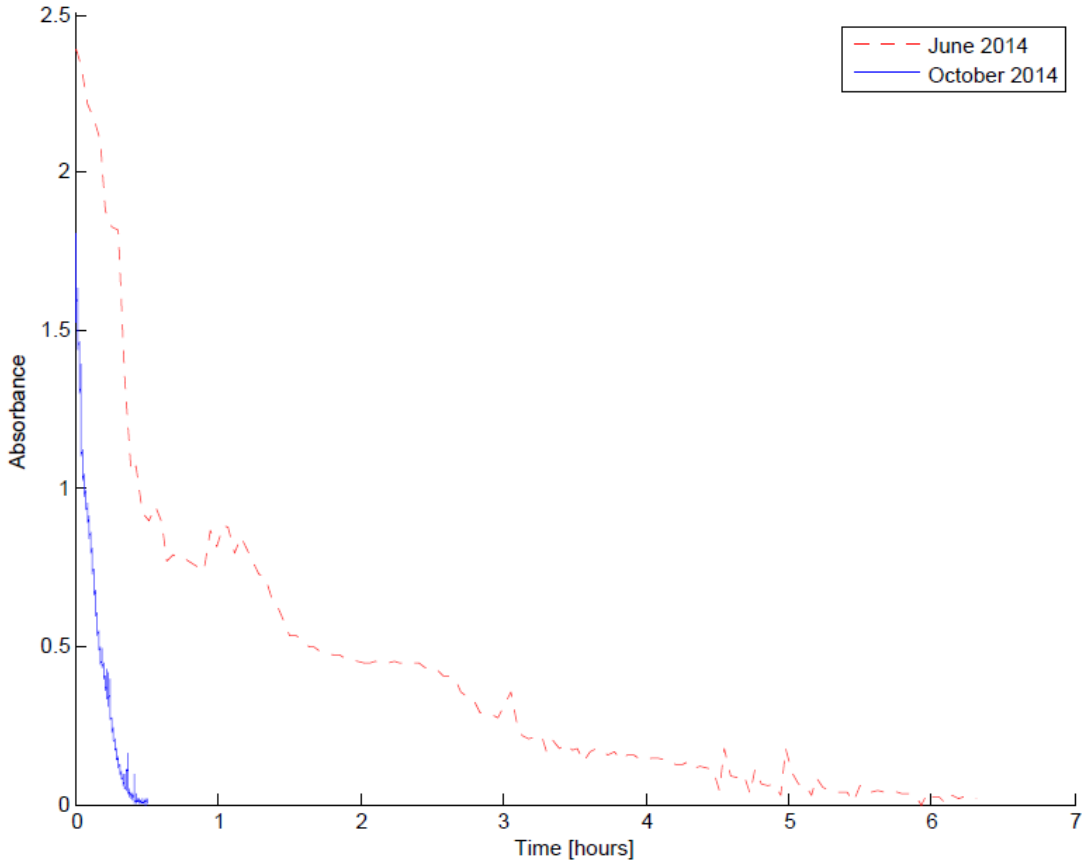

Fig. 9. The depletion of rubidium in the cell (once the AMD current was turned off) recorded by Dr. Christopher Rice at the beginning of this study and recorded again four months afterwards. For a given Matisse wavelength at a Rb spectral peak, the absorbance was recorded over time.

As with the previous AMD studies [4] [5] [6], once the current was shut off, the concentration of rubidium vapor (which was proportional to the absorbance) decreased exponentially with time. It took about 25 minutes for the amount of rubidium vapor to diminish by half, and about 6 hours for the concentration to become negligible. After four months of using the AMD system for absorption spectroscopy experiments and depleting about 10 AMD strips, the rubidium depletion was exponential as it was before, but the concentration decayed much more rapidly. The concentration had fallen by half after

about 6 minutes, and it had disappeared entirely after about 25 minutes. This increase in decay rate was most likely the result of cell contamination, which was evident in Figures 10 and 11.

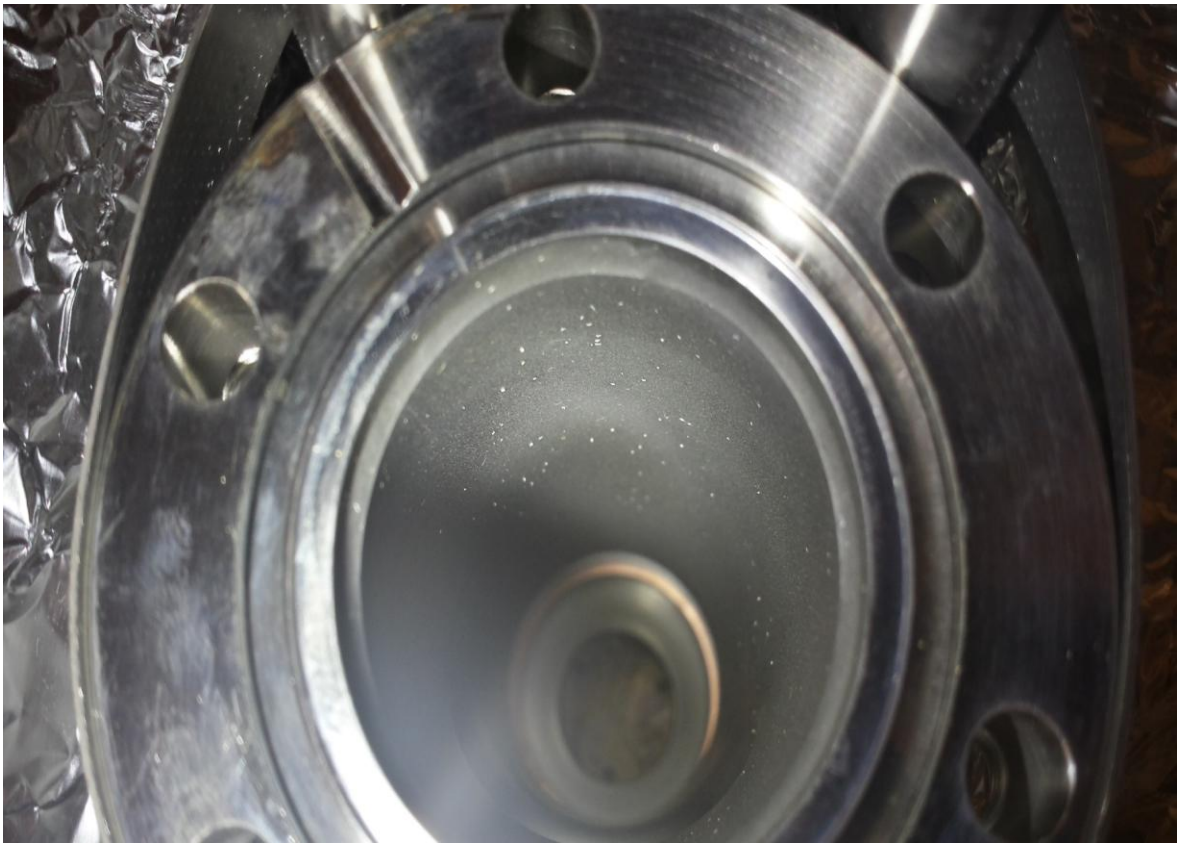

Fig. 10. The interior of the AMD chamber after the depletion of approximately 10 AMD strips over the course of several months. White specks had formed around the inside of the chamber. Due to Outgassing of the stainless-steel chamber, these were probably alkali metal hydrides, formed from rubidium vapor from the AMD and hydrogen from the stainless-steel.

Over several months of absorption experiments, white precipitates formed on the inside of the AMD chamber as seen in Figure 10, and contaminant buildup occurred on the copper surfaces of the valves as seen in Figure 11. The white precipitates were most likely rubidium hydride, formed as a result of the stainless-steel chamber outgassing

hydrogen [12]. These contaminants possibly reacted with any introduced rubidium and reduced the vapor concentration.

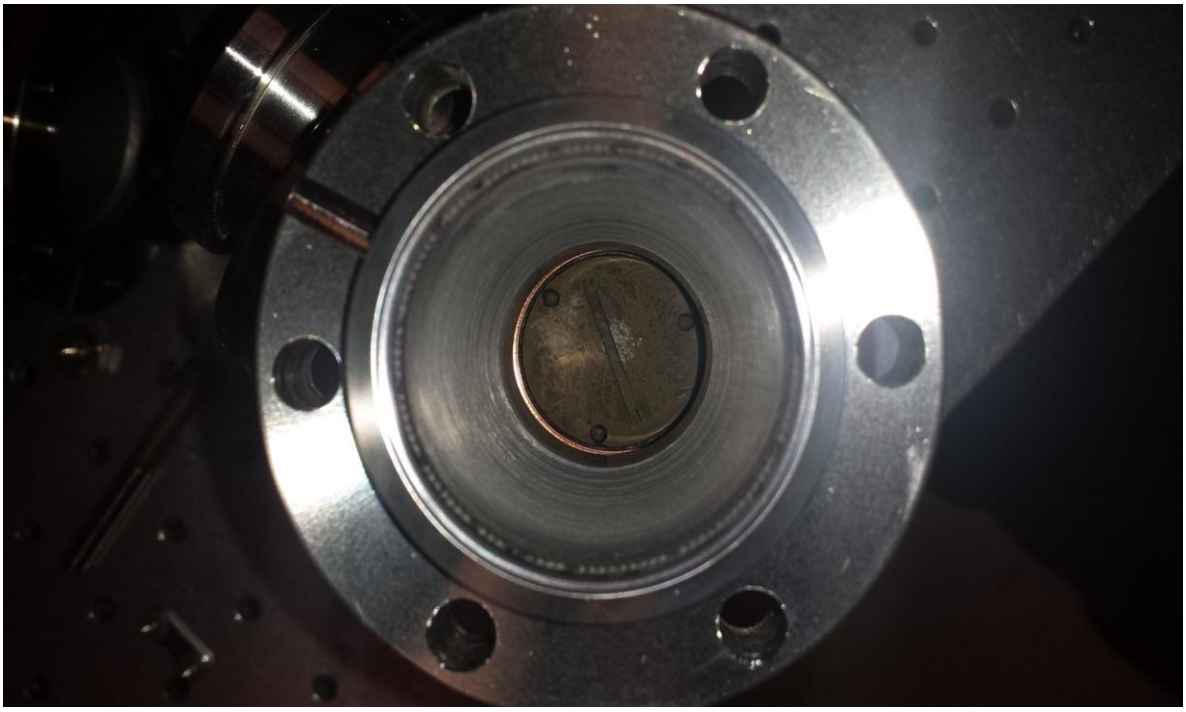

Fig. 11. The interior of the AMD cell showing the copper surface of the vacuum valve after the depletion of approximately 10 AMD strips over the course of several months. Subjecting the copper to heat resulted in contaminant buildup of the surface and these contaminants most likely reacted with alkali metal vapor and contributed to the rapid loss of concentration. Sonication of the chamber in an acetone bath removed some of the contamination, but a visible amount remained.

Conclusions

Although the use of alkali metal dispensers poses fewer hazards than using solid alkali metal, AMDs are currently not an ideal candidate for creating a lasing medium for a high-power laser. Although these dispensers have applications in high-temperature spectroscopy, the results indicate that several issues must be overcome before such a system can be used to create a DPAL.

An issue for making an AMD DPAL is the low rubidium concentration observed, at a maximum of $3.65 \pm 0.16 \times 10^{10}$ cm^{-3} under vacuum conditions, accounting for uncertainties in the temperature and effective gain medium length. For a 10 cm cell, this density gives a gain several orders of magnitude below the gain threshold obtained by Krupke [1]. This concentration would not be able to create a high-power laser in a poor Q resonator. One possible solution to this issue would be to use a highly reflecting output coupler or a longer AMD cell, although a cell too large would be impractical on an aircraft. Another possible solution to this issue would be to use a larger alkali metal dispenser with much more rubidium. Such dispensers would need to be capable of producing about 1,000 times the amount of alkali metal vapor. The fact that the observed absorbances were much higher when the AMD current was continuously run presents another possibility for creating the necessary concentration. It may be possible to continue running the current through the alkali metal dispenser while optically pumping the rubidium vapor. This would also require a much larger dispenser, as the results indicated that the type of AMD used in this experiment was unable to produce rubidium vapor at all at helium pressures of 100 torr or above. This solution would also have to address the issue of AMD lifetime, as the dispensers used in this experiment could no longer produce rubidium vapor after 20 to 30 minutes of use. It would be impractical to have a DPAL that would require such frequent AMD replacement, so the AMD used would have to remain viable for much longer.

Rubidium concentrations on the order of 10^{10} cm^{-3} allow incident pump lasers of powers around 1 W to remain in the Beer's Law domain throughout a cell of around 10 cm length. Therefore, AMDs are ideal for absorption spectroscopy experiments, and the

ability to control cell temperature independently of rubidium concentration gives the opportunity to observe homogeneous and inhomogeneous broadening rates as a function of temperature. If buffer gas could be added to chamber along with the rubidium vapor, pressure-broadening and pressure-shift rates could be determined for that buffer gas.

However, the aversion of the alkali metal vapor to buffer gas in the AMD chamber is an issue that must be resolved for both the AMD DPAL system and the high-temperature buffer gas kinetics spectroscopy. The helium added to the system both reduced the capability of the AMD to reach the necessary high temperatures (although this phenomenon was alleviated by applying a stronger current) and extinguished any preexisting alkali metal vapor. Because the noble gases are extremely nonreactive, this suggests that trace amounts of other species contaminated the cell when the helium was added. Atmospheric oxygen would react readily with alkali metal vapor by the reaction $4Rb + O_2 \rightarrow 2Rb_2O$, and only about 10^{10} cm^{-3} O_2 would be required to remove the rubidium in the cell. In a conventional DPAL system, the vapor is created via evaporation of the liquid alkali metal, and a significant bank of additional alkali metal would quickly replace any vapor that would react with contaminants. With an AMD, no additional alkali metal is added to the system after the initial current is run. As mentioned before, a possible solution to this problem would be to continuously run current through the AMD, which would require an AMD that could produce alkali metal vapor both at a much greater rate and for a much longer time than the ones used in this study.

Another issue with using an AMD to create a DPAL and to observe spectra involves the high amount of contaminants produced by such a system. Although conventional DPALs also produce contaminants, alkali metal dispenser strips contain

non-alkali species, which may collect on the chamber walls. The results indicated that the rubidium became depleted at a greater rate during the later trials, suggesting that the buildup of contaminants may have contributed to the rubidium vapor reactions. An AMD DPAL would have to be cleaned regularly and would require maintenance and replacement of any parts with contaminated surfaces.

These issues suggest that improvements to the AMD DPAL concept would have to be made in regards to both alkali metal vapor producing ability and system usability before the concept could be considered a strong alternative to the conventional DPAL model. The AMD system will be a powerful tool for obtaining pressure-broadening and pressure-shift rates once the reactivity and contamination issues are resolved.

This study also indicated that there is more research to be done in the use of alkali metal dispensers for both optical and non-optical purposes. All previous studies involving AMDs were performed at vacuum conditions, so future studies should focus on the use of AMDs under pressure in order to obtain a more sophisticated characterization. In particular, the ability of a thermally and chemically inert gas such as helium to prevent a resistor such as rubidium chromate from heating in response to an applied current is a matter that should be investigated further.

III. Bleached Rubidium Cell Analysis

Background

The second portion of this study focused on side fluorescence in DPAL (non-AMD) cells. Several studies have succeeded in demonstrating diode pumped alkali lasers using various pump intensities, alkali metal vapor concentrations and buffer gases. To achieve lasing in a rubidium cell, Krupke *et al.* used a CW titanium sapphire laser at 500 mW with a spot diameter of about 400 μm (approximately 100 W/cm^2). The cell contained 75 torr of ethane to achieve the necessary spin orbit relaxation rate and 525 torr of helium, which pressure-broadened the line to about 10 GHz (the pump laser had a 50 GHz linewidth). The cell was heated to 120^oC to achieve a rubidium density of about 1.7 $\times 10^{13}$ cm^{-3}. Krupke was able to achieve lasing at the D_1 line at a slope efficiency of 54% [1]. Although they have lower spin-orbit relaxation rates, noble gases are preferable to hydrocarbons as buffer gases, as rare gases do not produce soot. Wu observed a comparable result to Krupke's, using only helium as the buffer gas. Wu used a CW titanium sapphire laser at 2.7 W with a spot diameter of about 220 μm (approximately 1.8 kW/cm^2). The cell contained 2050 torr of helium, pressure-broadening the line to about 40 GHz (the pump had a 50 GHz linewidth). With a rubidium density of 2.2 $\times 10^{14}$ cm^{-3} at 170^oC, Wu was able to achieve a slope efficiency of 21% [2]. A similar result was obtained by Zhdanov *et al.* using 600 torr of ethane. Zhdanov used a 17.5 W pump laser with a spot diameter of about 500 μm at 103-106^oC to achieve a slope efficiency of 60% [14]. These parameters are displayed in Table 2 in Appendix A.

Through observing the side fluorescence and determining the bleached regions of an alkali metal cell, it can be determined whether or not similar conditions to previous successful DPAL models were met and whether or not lasing occurs when neon buffer gas is used (as an alternative to helium). Side fluorescence can be observed when the medium inside a cell absorbs and then emits radiation. When a two-level system is bleached, it signifies that the population in the excited state equals that of the ground state, accounting for the ratio of degeneracies. For the rubidium system observed in this study, the degeneracies indicate that in a bleached system, twice the rubidium is in the excited state than the ground state. Once a region of an alkali metal cell is bleached, that region will not absorb any more photons from an optical pump until the excited atoms relax back into the ground state.

For the rubidium D_2 line at 120^{o}C, at pressures of over 62.3 torr, a Lorentzian distribution will dominate the spectral lineshape. Collisional processes between the alkali metal vapor and the buffer gas broaden and shift the spectral features. The pressure broadening rate of the rubidium D_2 line for the neon used in this study is γ_L = 9.47 MHz/torr and the shift is δ = - 2.44 MHz/torr [11].

Saturation of a medium has an effect on the propagation of a laser though that medium. The saturation intensity I_{sat} is given by,

$$I_{sat} = \frac{h\nu A}{\sigma(\nu)} \tag{2}$$

where h is the Planck Constant, v is the frequency of the radiation, A is the spontaneous emission Einstein coefficient of the upper state, and $\sigma(v)$ is the cross section calculated in

Equation 1 as a function of frequency. The saturation intensity is not a physically observed intensity, but rather a collection of parameters that have the same dimensions as intensity when grouped together. As radiation propagates through a cell, the intensity decreases with respect to propagation distance *z* by the following differential equation,

$$\frac{dI}{dz} = \frac{-\sigma n I}{1 + I / I_{sat}} \tag{3}$$

where I is the intensity, σ is the cross section calculated in Equation 1, n is the population density of the resonant species, and I_{sat} is the saturation intensity from Equation 2. The parameter I/I_{sat} is referred to as the degree of saturation, S. It follows from Equation 3 that I_{sat} can be defined as the intensity at which the absorption is halved. Equation 3 simplifies to other expressions when at high or low intensity,

$$I << I_{sat} \rightarrow \frac{dI}{dz} = -\sigma n I \rightarrow I(z) = I_0 e^{-\sigma n z} \tag{4}$$

$$I >> I_{sat} \rightarrow \frac{dI}{dz} = -\sigma n I_{sat} \rightarrow I(z) = I_0 - \sigma n I_{sat} z \tag{5}$$

and these differential equations can be solved to give the Beer's Law expression for exponential decay for the $I << I_{sat}$ (optically thick) case and linear decay for the $I >> I_{sat}$ (bleached) case. A partially bleached cell will exhibit either of these behaviors at different horizontal distances z in the cell. After the beam passes from the bleached region to the Beer's Law region, exponential decay almost immediately lowers the transmitted intensity to near zero. Side fluorescence can only be observed from areas in a cell that are bleached, otherwise there will not be enough remaining photons to excite the medium. For a saturated sample with a homogeneously broadened spectrum, Equation 3

indicates that the absorbance will be lowered more at the center of each spectral peak than at either side of the peak. This results in saturation broadening, which will decrease the peak absorbance by a factor of $(1 + S)$ and increase the FWHM by a factor of $(1 + S)^{1/2}$ [15].

In a previous study, Lewis constructed a theoretical model of the laser intensity of a partially bleached cell by a 20 GHz bandwidth pump laser as function of wavelength and propagation distance. Lewis predicted that the intensities would decrease linearly with horizontal propagation at roughly the same rate for all frequencies in the pump bandwidth, although frequencies farther off resonance have higher saturation intensities and the intensity would decrease more slowly after reaching this threshold [16]. Assuming the rubidium cell does not lase, it is useful to compare a partially bleached cell to Lewis's model and confirm that they match and that saturation broadening is observed.

Experimental Set Up

The cell used was a 5 cm transparent Pyrex cell that contained solid rubidium and 500 torr neon buffer gas. The cell was placed in a metal heater block with four Watlow C1J6-L12H heating rods and a T-type thermocouple connected to the Watlow controller. One of the four corners of the cell was removed, exposing the clear Pyrex surface. Aluminum foil was used to increase thermal transfer, but much heat was still lost from the exposed parts of the cell due to contact with the air.

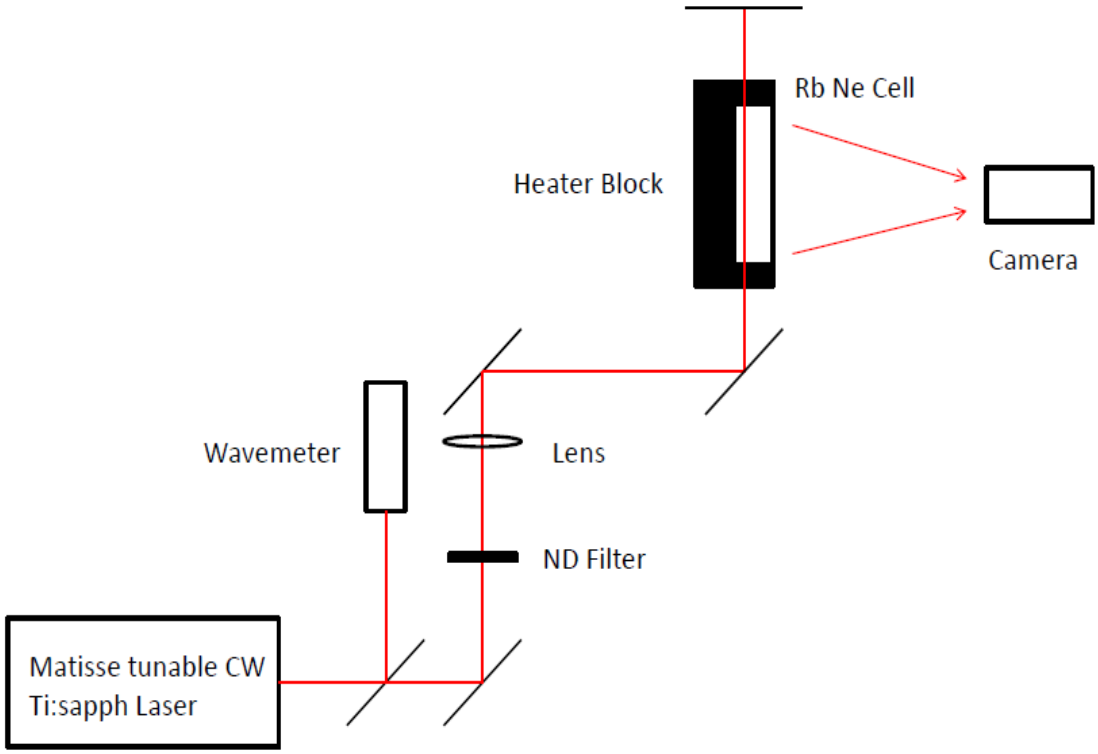

Fig. 12. The Experimental apparatus for the bleached wave analysis. The beam from the Matisse tunable CW Titanium Sapphire laser was measured by a High Finesse WS-7 wavemeter. The beam propagated through a 5 cm Rb cell with Ne buffer gas and onto a beam stop, and the Marlin camera captured images of the side fluorescence. For readings of different powers, filters of neutral density 0.5, 1.0, 1.5, or 2.0 were placed after the first mirror. If a lens was used for a particular setup, that lens was always placed at an optical path distance from the center of the cell equivalent to the focal length of that lens (this image shows the position of the 25 cm lens).

The beam from the tunable Matisse laser was tuned to the Rb D_2 line center at 780.24 nm and directed through the rubidium cell. A Marlin IEEE 1394 camera (and at later points in the study a Manta G-609 camera) was placed perpendicular to the optical path and directed at the open region of the cell. The mirrors were adjusted such that the beam traveling through the cell was always horizontal with respect to the image taken in

order to accurately obtain horizontal distance from horizontal pixel distance in the images.

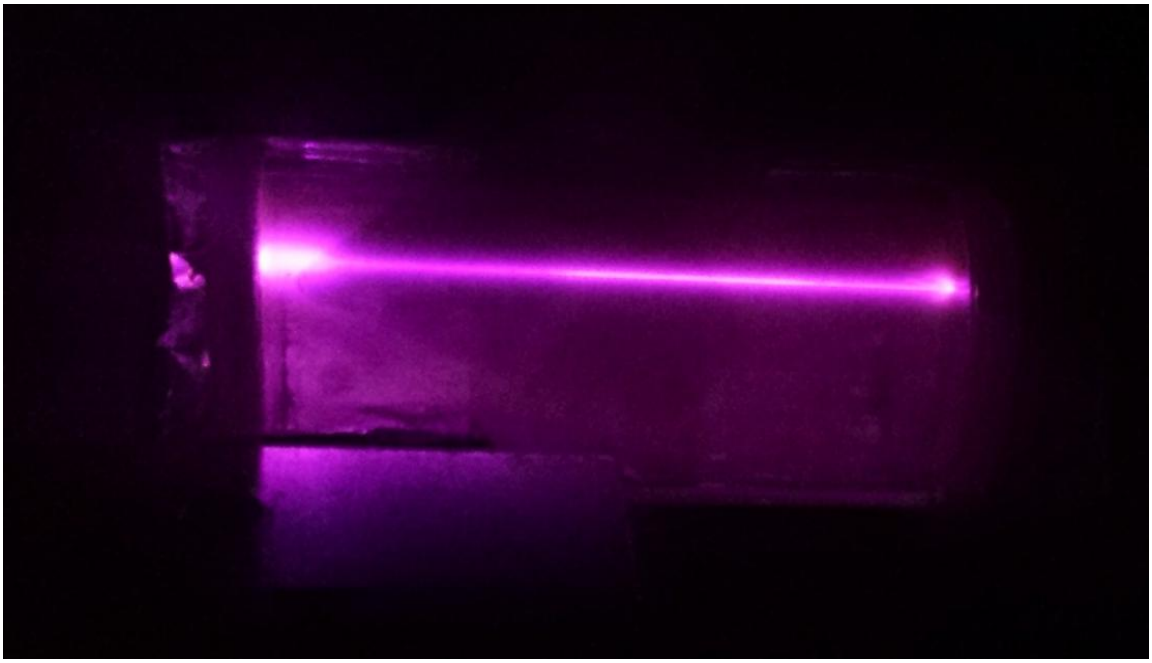

Fig. 13. Image of the rubidium Pyrex cell with neon buffer gas with an unattenuated, focused beam from the Matisse tunable laser (this image was taken with a commercial color camera, not the mounted Marlin camera used for indentifying the intensity indices at each point in the cell). The region where the rubidium vapor was bleached exhibited side fluorescence, resulting in a visible purple glow.

Multiple images were taken for different combinations of beam parameters. The cell produced rubidium by evaporation of rubidium metal, so rubidium density was varied by adjusting the cell temperature. Incident laser power was adjusted by placing various neutral density filters before the cell. Incident powers of 500 mW, 168 mW, 50 mW, 16 mW, and 5 mW were attained using neutral densities of 0, 0.5, 1.0, 1.5, and 2.0 respectively. The images were taken with 25 cm and 15 cm lenses focusing the beam, in addition to trials with no lens; if a lens was used, it was placed at a distance of a focal

length away from the center of the cell. The wavelength of the Matisse pump beam was also adjusted to obtain data at a range of frequencies around the D_2 line.

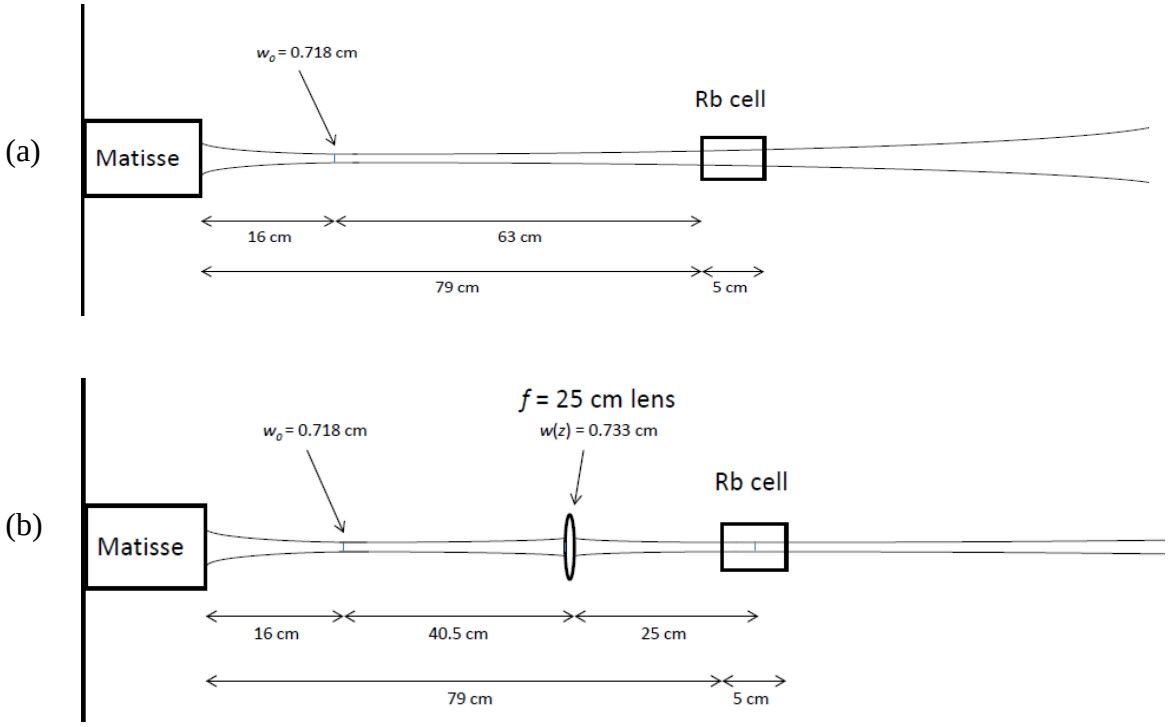

Fig. 14. Diagrams of the spot size as the beam propagated through the optical path for the trials with no lens (a) and with the 25 cm focal length lens (b). Values measured with a MMH-2S ModeMaster were used to determine the spot sizes calculated at each point in the diagrams.

Contamination of the Pyrex cell wall was an issue at temperatures above 120^{o}C; excessively heating the rubidium sample caused solids to form on the surfaces, obstructing the camera's view of the beam propagation. Images were captured as quickly as possible, especially at the higher temperatures, to minimize the formation of precipitates on the surfaces. Despite the contaminants, for each image of the bleached cell, the point at which the bleached region ended in the cell was always apparent. The horizontal limit of propagation was recorded for each configuration (this limit was apparent in Figures 16 and 17).

Results

An MMH-2S ModeMaster was used analyze the beam and determine the beam waist and M-squared: $2w_0$ = 1.437 mm and M^2 = 1.07 (the beam waist w_0 is shown in Figure 14). Using these values and the location of the beam waist, the spot size $w(z)$ at each distance z was calculated for trials with no lens and trials with lenses of focal lengths of 15 cm and 25 cm.

The Matisse reached powers of up to 1.4 W and a 25 cm lens was used to focus the spot size down to 200 μm (achieving approximately 1 kW/cm^2). These parameters were comparable with those of previous studies (see Table 2 in Appendix A), the only notable difference being the neon buffer gas in this study. A rubidium D_1 line filter (reducing the power of the D_2 line frequency by a factor of 200) was used on the resulting beam after the cell with the output directed into the WS-7 wavemeter, but no stimulated emission at 795 nm was observed.

Using the same photodiode and detector setup as was used in the alkali metal dispenser portion of this study, a pressure-broadened absorption spectrum shown in Figure 15 was obtained at 50^{o}C. The model shown in Figure 15 was matched against the data in the same manner as was done in the Doppler-broadened case to indicate the rubidium vapor concentration. Due to hardware limitations, a continuous scan of the larger pressure-broadened spectrum could not be obtained and had to be piece together from smaller scans.

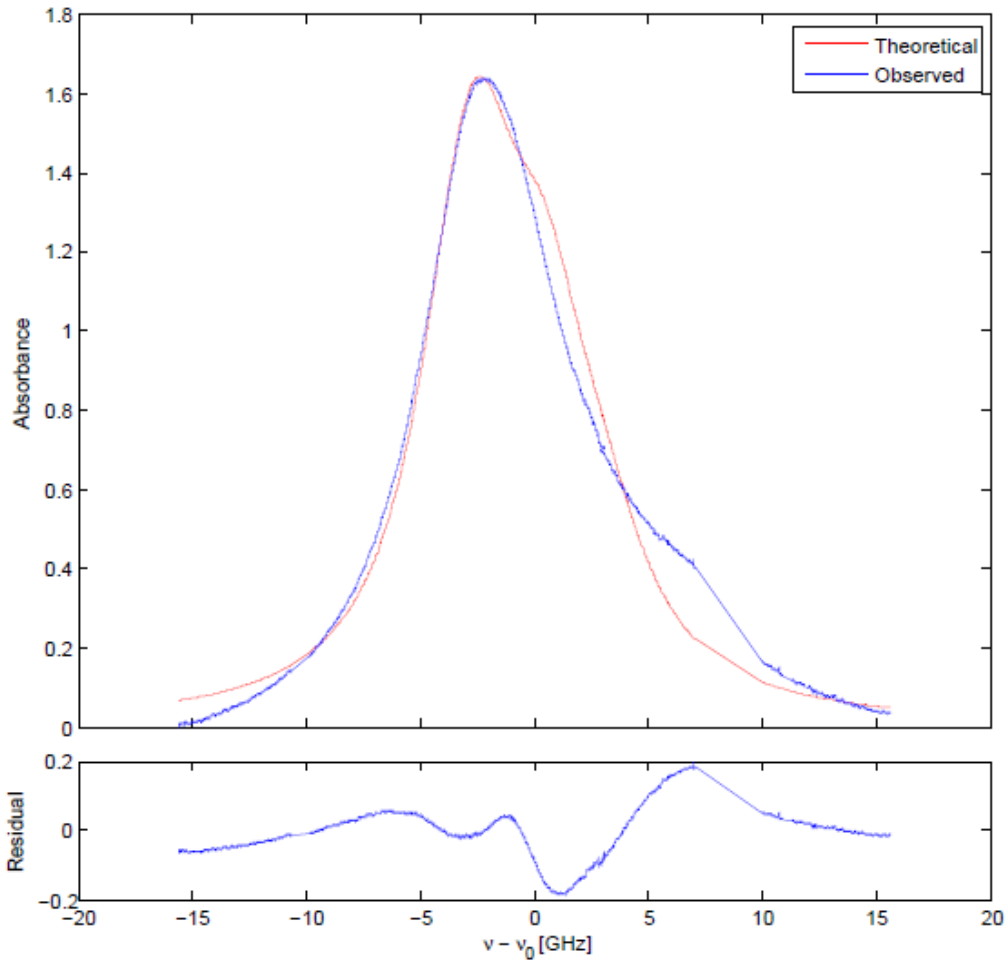

Fig. 15. Pressure-broadened absorption spectrum of the rubidium Pyrex cell with neon buffer gas at 50°C. The observed spectrum in blue is plotted against the theoretical model in red for ν_0 = 384.23 THz. The four peaks that were observed in the Doppler-broadened case were pressure-broadened into a single feature. The peak absorption indicated a rubidium vapor concentration of 1.9×10^{11} cm^{-3}. The limited scan range of the Matisse resulted in a discontinuous region around 10 GHz. There also a shift of approximately 600 MHz (corrected in the figure), which is about 10 times the reported error on the wavemeter.

The model fit the absorption spectrum with an R^2 value of 0.9823 and it indicated a rubidium vapor concentration of 1.9×10^{11} cm^{-3}, which was approximately an order of magnitude lower than the vapor pressure formula suggested for rubidium at 50°C. A quarter of the heater block had been removed in order to obtain a clearer view for the camera, so it was likely that the temperature given by the thermocouple was not the

actual temperature of the Pyrex cell, and a temperature difference of about 15^{o}C to 20^{o}C would account for the difference in observed rubidium vapor concentration.

The images taken with the Marlin camera were analyzed in order to determine the bleached regions and beam intensities in the cell for each configuration. Examples of the trial with no lens are shown in Figures 16 and 17. The widths of the bleached regions were not always apparent due to contamination on the Pyrex surfaces. This study instead focused on determining the total bleached length with respect to each of the parameters. For each of the following cases, total bleached length is defined as the horizontal distance *z* from the first window of the cell to the point at which fluorescence was no longer observed. In many of the cases, the laser bleached the entire length of the cell; if this was the case, the total bleached length was recorded as 50 mm, the total length of the cell.

Due to the contaminated surfaces and absorption and reemission of photons within the rubidium vapor, there was an uncertainty of about a millimeter in the determination of the horizontal limit of propagation in each frame. Two methods were used to determine this limit. The first method (used for the majority of the study) was to choose the first pixel at which the two pixels immediately below and above had no difference in intensity. The second method (used at the end of this study) was to record the intensity as a function of horizontal length and indentify the bleached region at which intensity decreased linearly with distance. The linear region was then extrapolated to determine the point at which the line would intersect the baseline, and this point was chosen as the horizontal limit of propagation. These two methods usually produced values within 5 pixels of one another when comparing bleaching as a function of rubidium concentration and pump power.

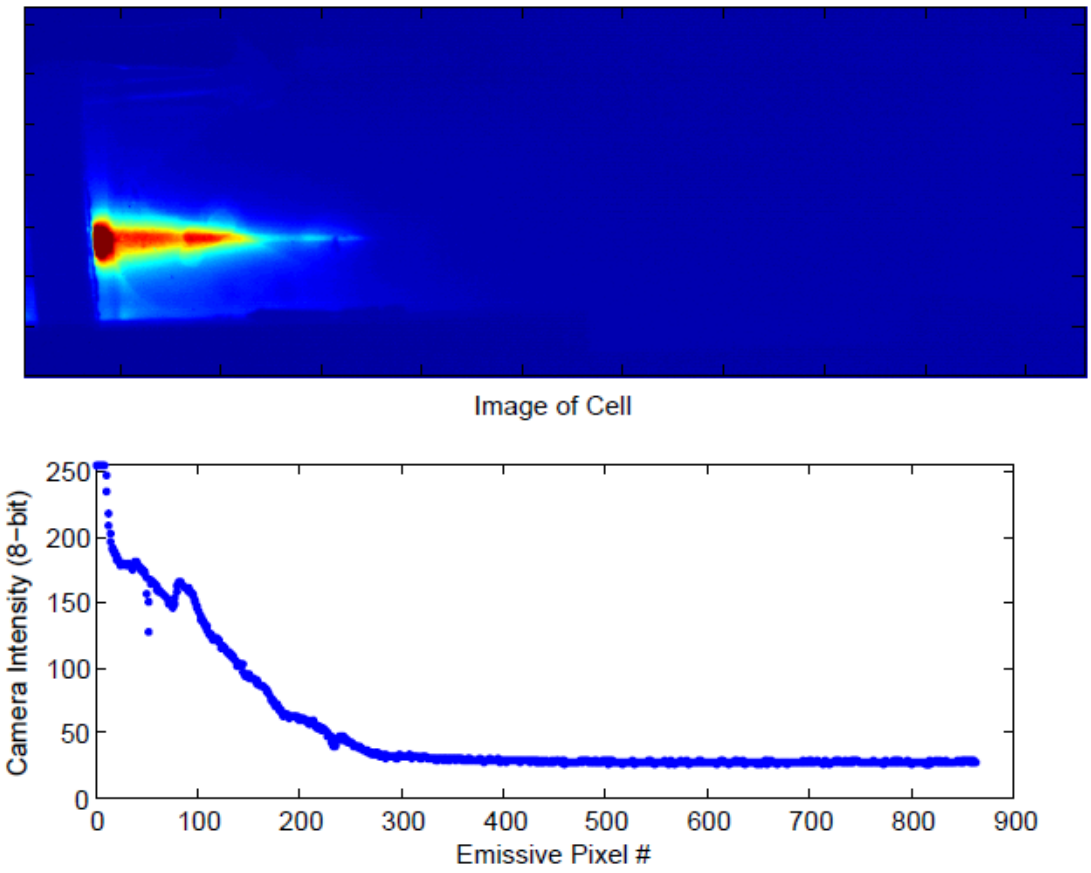

Fig. 16. Image of 168 mW beam propagation from left to right with no lens in the Pyrex cell at 120^{o}C taken with the Marlin camera. 17.5 pixels in the image are the equivalent of 1 mm. There was a wider bleached area near the beginning of the cell and the intensity tapered off before the middle of the cell. Contamination on the Pyrex windows made the apparent beam intensity around pixel 90 decrease. The decrease in intensity at beam center matches the linear model in Equation 5.

Figure 16 showed a linear decrease in intensity in the region where side fluorescence occurred, indicating that the cell was bleached in this region. Once the intensity approached the baseline, there was a very rapid transition to exponential decay given by Beer's Law.

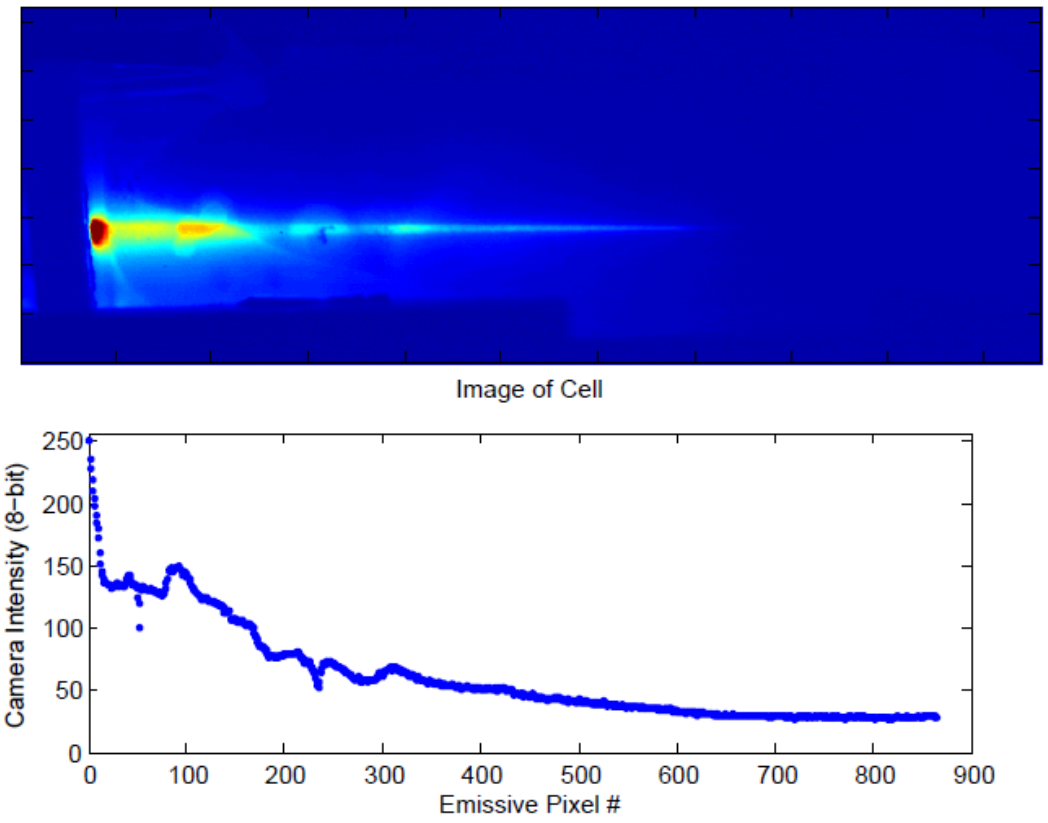

Fig. 17. Image of 168 mW beam propagation from left to right with no lens in the Pyrex cell at 105°C taken with the Marlin camera. 17.5 pixels in the image are the equivalent of 1 mm. There was a wider bleached area near the beginning of the cell and the intensity tapered off before the end of the cell, at a lower rate than that of the case with higher rubidium concentration. Contamination on the Pyrex windows made the apparent beam intensity around pixel 90, 190, and 290 decrease. The decrease in intensity at beam center matches the linear model in Equation 5.

The total bleached horizontal distances were recorded for no lens, a 15 cm lens, and a 25 cm lens, at temperatures from 85°C to 150°C in intervals of 5°C, and with neutral density filters of 0.5, 1.0, 1.5, and 2.0. The propagation distance is plotted with respect to rubidium density for the no lens trial in Figure 18.

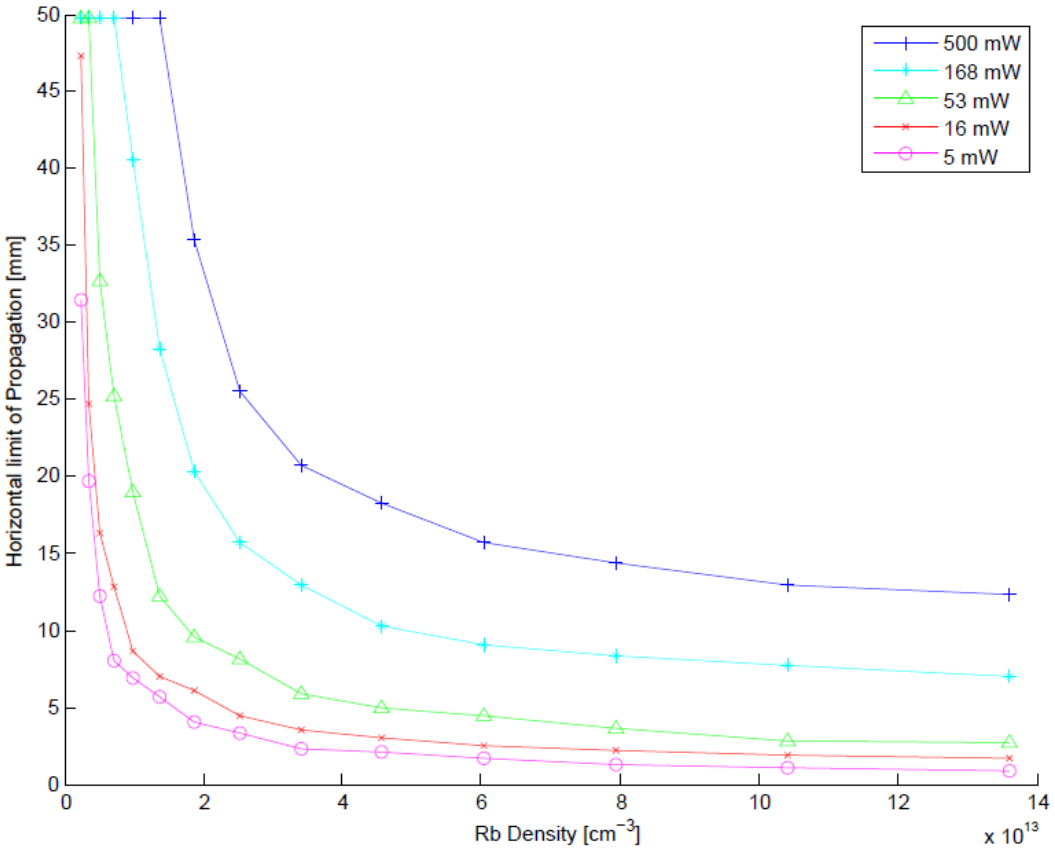

Fig. 18. The horizontal limit of beam propagation with respect to rubidium vapor concentration for a system at various powers and using no lens. For beams that propagated through the entire cell, the horizontal limit was recorded as 50 mm.

The trend clearly showed the propagation as a function of the inverse of the rubidium density. The same data is plotted in Figure 19 with instead the inverse of the rubidium density on the x-axis.

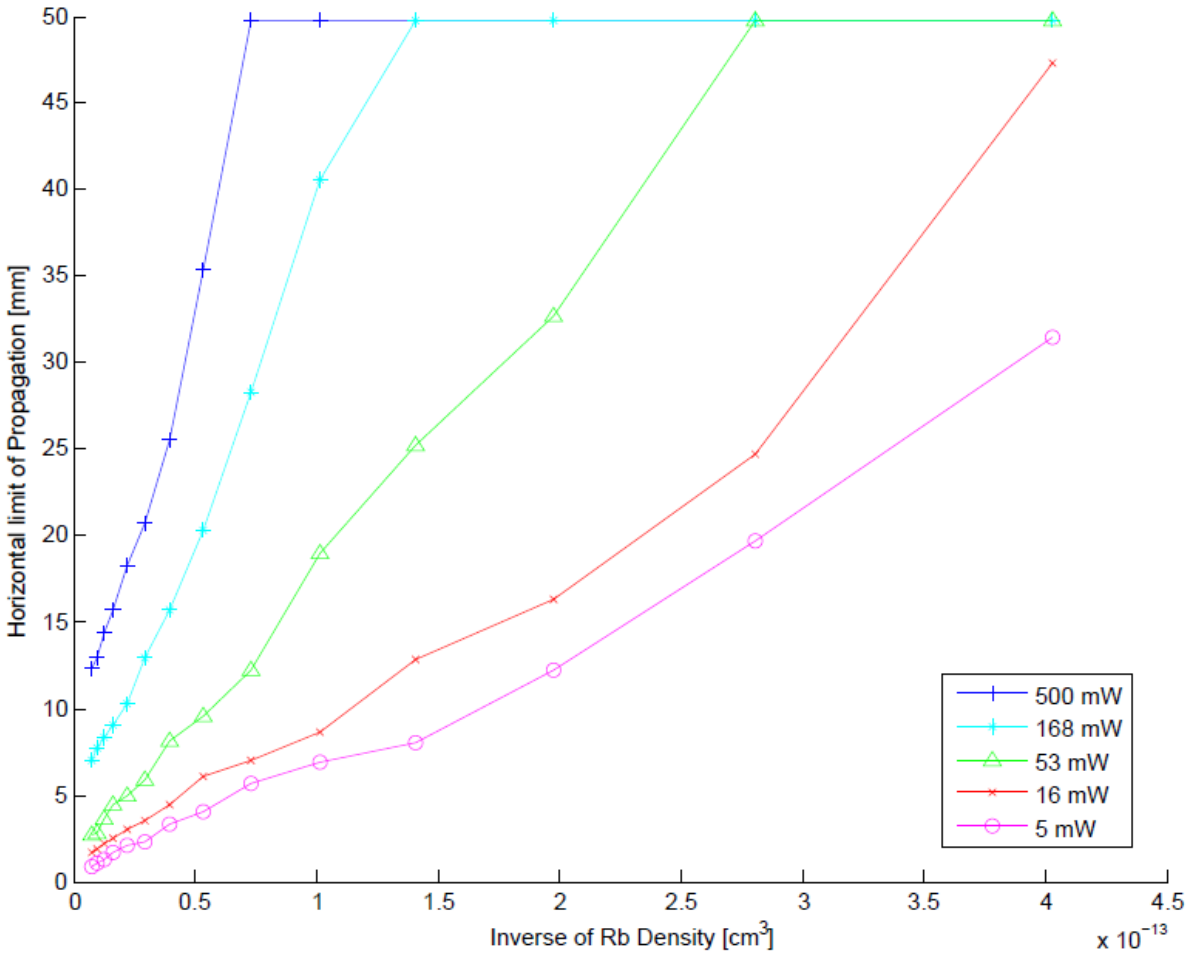

Fig. 19. The horizontal limit of beam propagation with respect to the inverse of rubidium vapor concentration for a system at various powers and using no lens. For beams that propagated through the entire cell, the horizontal limit was recorded as 50 mm.

The propagation distances with respect to inverse density were shown to be roughly linear, as was expected from Equation 5. The propagation distance as function of power is plotted in Figure 20.

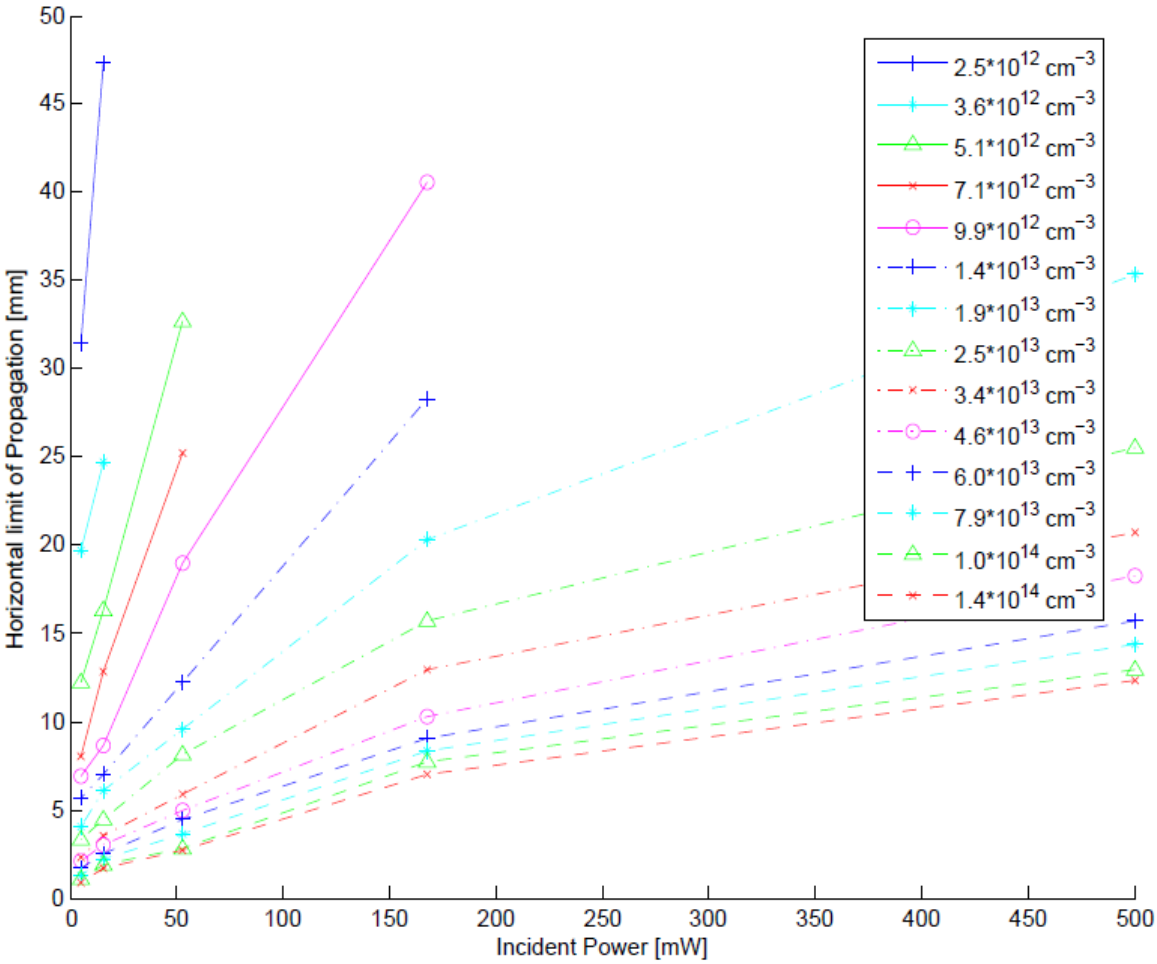

Fig. 20. The horizontal limit of beam propagation with respect to Matisse power for a system at various rubidium densities and using no lens. Due to sharp propagation limit cutoffs at higher powers, the points where the pump laser bleached the entire cell were removed from the plot.

The plot with respect to power was mostly linear, although the higher pump laser powers did not return propagation distances as high as were expected. Plots of the same parameters as Figures 18 through 20 for the 15 cm lens trials and the 25 cm lens trials can be found in Appendix B. To compare the different lens trials, the slopes of the linear regression fits of the propagation distances with respect to inverse density and power must be found.

From Equation 5, in the bleached region of an absorption cell,

$$I(z) = I_0 - \sigma n I_{sat} z \tag{5}$$

can be used to determine the distance of propagation. Since I_{sat} includes a factor of σ in the denominator, this equation can be rewritten as

$$I(z) = I_0 - nh\nu Az \tag{6}$$

in terms of the Einstein coefficient A and frequency ν. At the horizontal limit L where bleaching no longer occurs, $I(L) \approx 0$. Therefore, at this point,

$$L(n) = \frac{I_0}{nh\nu A}, \tag{7}$$

which can be used to find L as a linear relation of $1/n$ with the other parameters held as constant. Equation 7 can be rewritten as

$$L(P_0) = \frac{1}{\pi w^2 nh\nu A}(P_0), \tag{8}$$

where P_0 is the incident power and w is the beam radius, and now the equation gives L as a linear relation of incident power, assuming w does not vary with respect to L. The coefficients in Equations 7 and 8 indicate the slopes of the lines in Figures 19 and 20 respectively, and these slopes can be quantified with a linear regression fit. The slopes from Figure 19, along with the respective slopes from the 15 cm lens case and the 25 cm lens case, were plotted together in Figure 21.

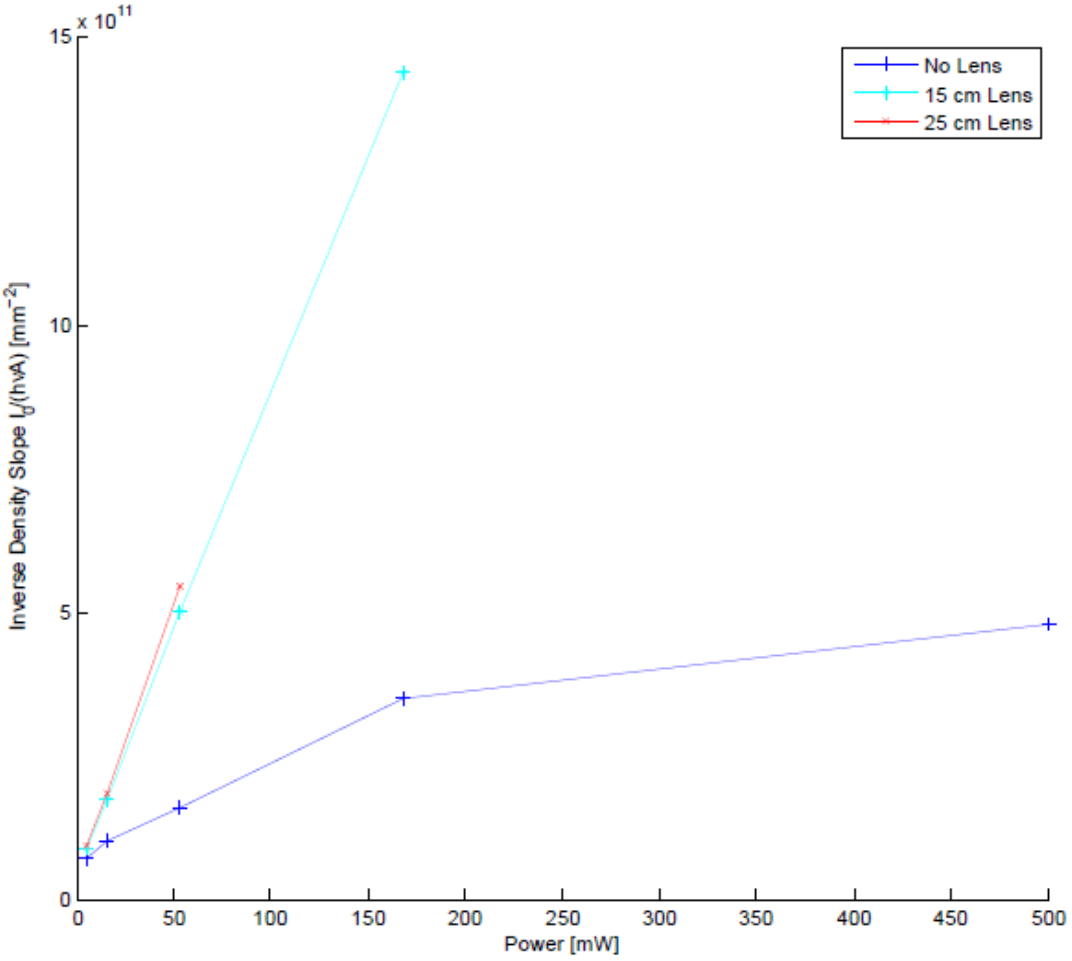

Fig. 21. The slopes of the linear fits of each of the lines in Figure 19, plotted with respect to Matisse power. The respective slopes were also found for the 15 cm lens and 25 cm lens cases and plotted alongside the no lens case.

For the data taken with lenses, the horizontal propagation of the beam was 2 to 3 times larger than that of the no lens trial for a given power. The case with no lens was not as linear with the high pump powers, but there weren't enough data points with the 15 cm and 25 cm lens data (with the lenses at higher pump laser powers, often the entire cell was bleached) to indicate whether or not these cases would have exhibited a similar drop

off at higher powers. The slopes from Figure 20, along with the respective slopes from the 15 cm lens case and the 25 cm lens case, were plotted together in Figure 22.

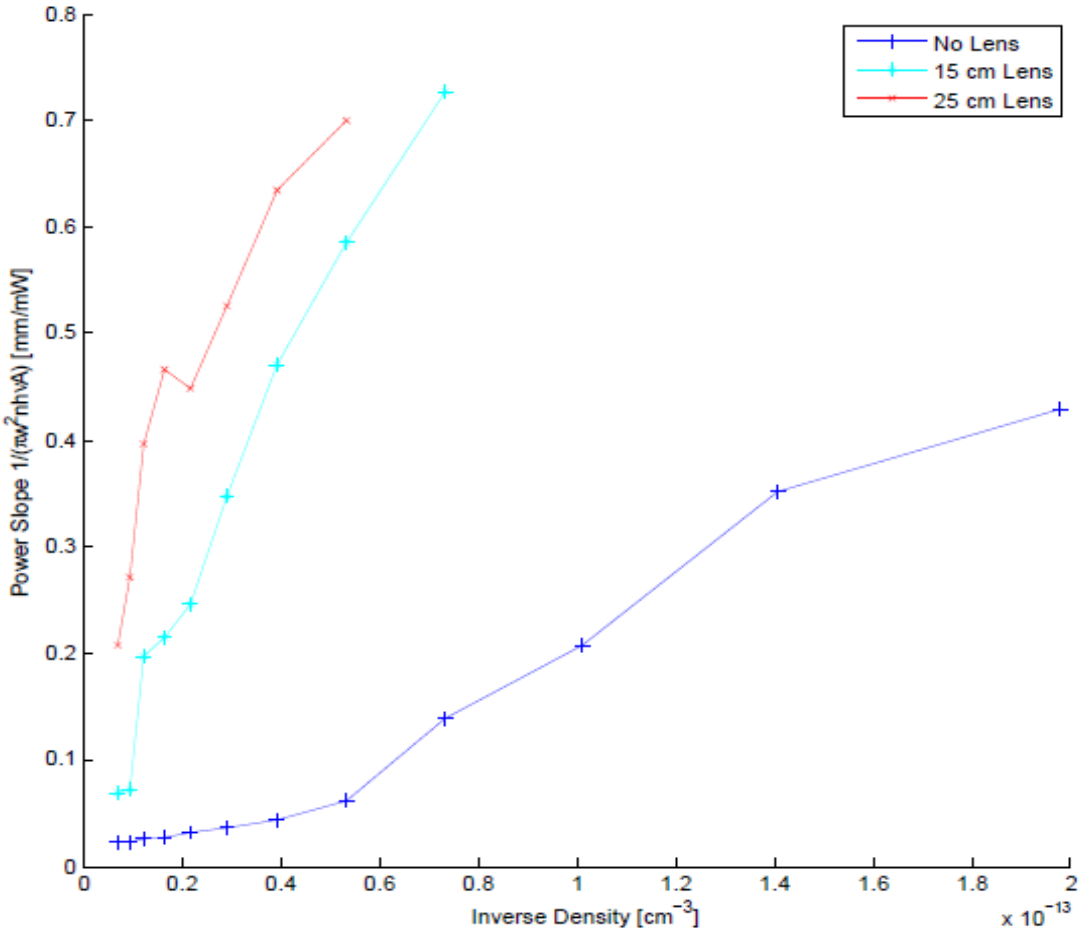

Fig. 22. The slopes of the linear fits of each of the lines in Figure 20, plotted with respect to Matisse power. The respective slopes were also found for the 15 cm lens and 25 cm lens cases and plotted alongside the no lens case.

For the data taken with lenses, the horizontal propagation of the beam was 3 to 5 times larger than the no lens case for a given density.

In general, the horizontal distance of the limit of beam propagation was proportional to the Matisse power and proportional to the inverse of rubidium vapor

concentration. These findings were consistent with the expected results, as the number of rubidium atoms in the beam path should be proportional to the rubidium vapor concentration and the number of photons available to excite the rubidium atoms should be proportional to the laser power. The biggest deviation from linearity in this model was in the cases concerning the 15 cm lens (as seen in the Figures in Appendix B), especially with the comparison between Matisse power and propagation distance. This could be explained by the fact that the 15 cm beam had the sharpest focus of all three cases, and therefore the volume did not scale linearly as a function of propagation distance.

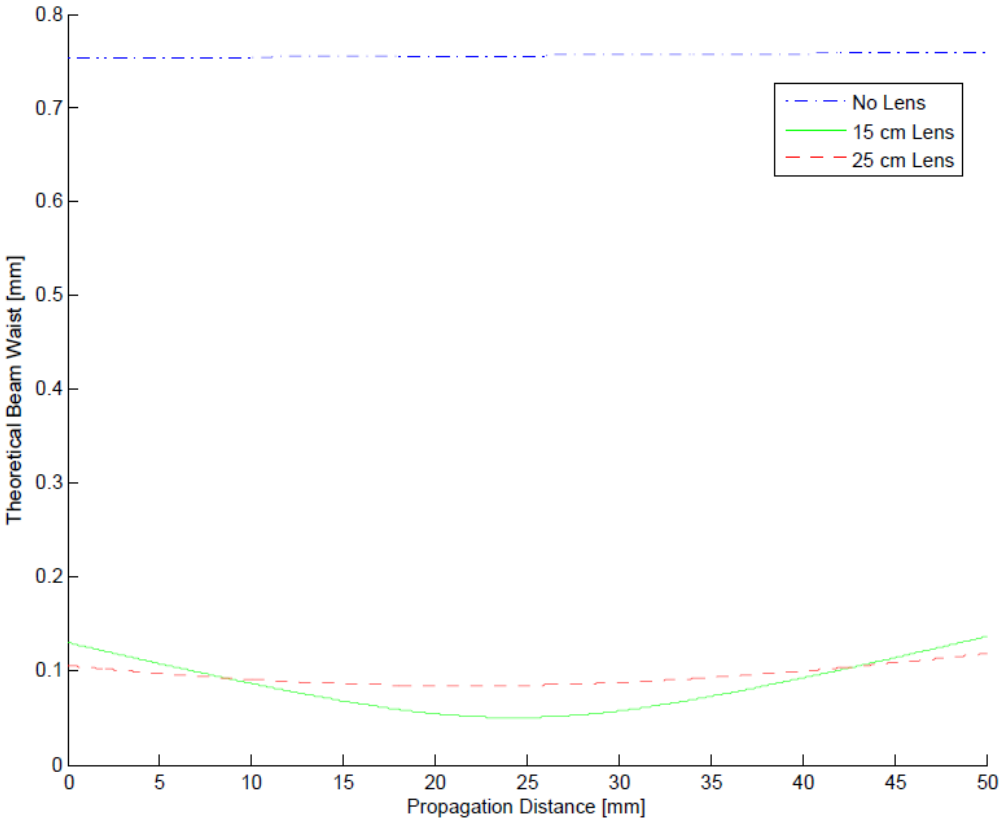

Fig. 23. The spot size, according to the values from the ModeMaster at each horizontal position in the cell for both lenses used, as well as the no lens case. With no lens, the beam divergence was almost linear with a total change of less than 2%. The 25 cm lens resulted in a spot size that was mostly uniform around 100 µm. The 15 cm lens resulted in a much smaller radius in the center than at the edges, reaching a minimum around 50µm, which might not be a feasible spot size to attain due to aberrations in the lens.

In order to compare the bleached distances between cells with different lenses focusing the beam, it was necessary to calculate the total bleached volume as a function of propagation distance. To do this accurately, the Matisse beam parameters had to be known. The values taken from the MMH-2S ModeMaster ($2w_0$ = 1.437 mm and M^2 = 1.07) were used to plot the spot size at each point in the 5 cm cell in Figure 23, and the corresponding intensity (for a 500 mW beam) in Figure 24.

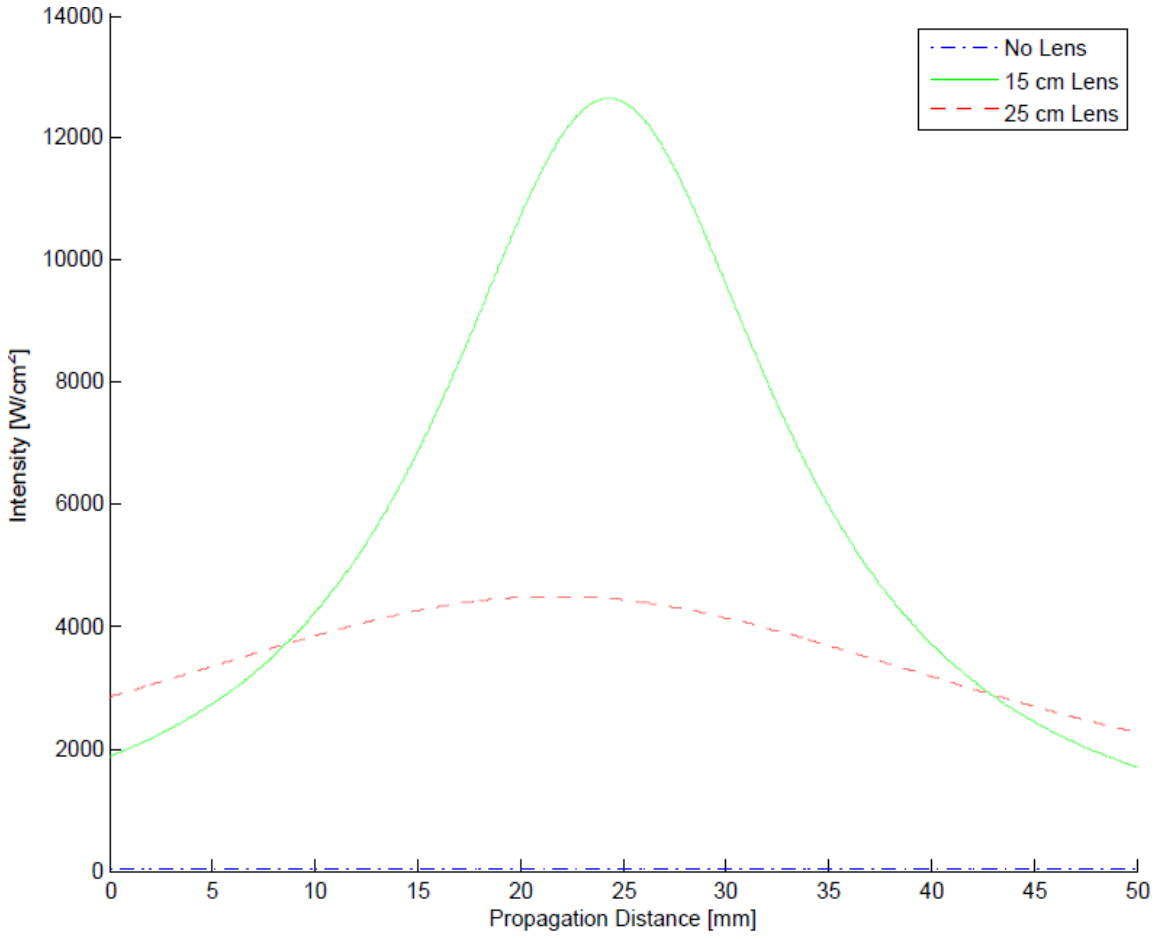

Fig. 24. The beam intensity, according to the values from the ModeMaster, at each horizontal position in the cell at beam center for a Matisse power of 500 mW for both lenses used, as well as the no lens case. With no lens, the change in intensity was at least 30 times lower than that of the other two cases at every point. The 25 cm lens resulted in a peak intensity of 4 kW/cm^2 and the 15 cm lens resulted in a peak intensity of 12.5 kW/cm^2, which might not be feasible due to aberrations in the lens.

Assuming the $w(z)$ model was valid for this system, the intensity for each point at beam center could be calculated. The Matisse had a Gaussian shape with the peak at the center. For a given power, the intensity at each horizontal point (assuming no absorption) at radial beam center ($r = 0$) could be determined by dividing the power by the area given by the spot size.

Although the images taken of the cell were not clear enough for the total bleached volumes to be determined from direct observation, these volumes could be calculated from the horizontal limit of propagation of the beam center. If a hypothetical beam had identical power to the Gaussian beam, but instead of a Gaussian shape had, at each horizontal distance, a uniform distribution of intensities all equal to the intensity at the beam center ($r = 0$), all points on the cross sectional slice of the beam (of radius $\sqrt{2} \times w$) would propagate to the same final point in the cell. These two hypothetical beams would have the same total power, and they would have equivalent potential to bleach a volume containing the same number of rubidium atoms. Given equivalent rubidium concentrations, these two beams would bleach equivalent volumes. Therefore, calculating the total bleached volume for each horizontal distance for the hypothetical uniform intensity case also determines the total bleached volume for the actual Gaussian case. The total bleached volume for each lens configuration is plotted in Figure 25.

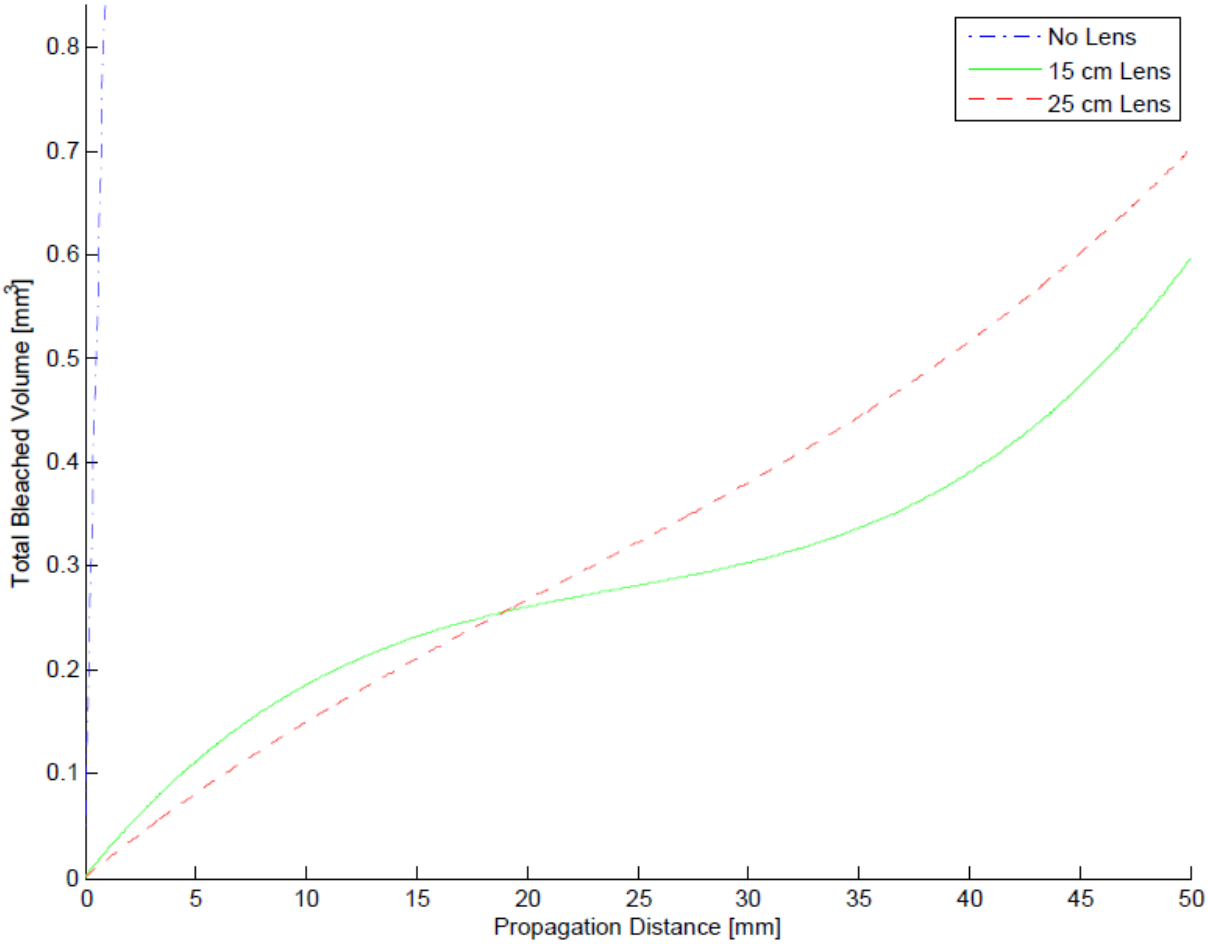

Fig. 25. The total bleached volume for all of the bleached space up to a point, according to the values from the ModeMaster, at each horizontal position in the cell for both lenses used, as well as the no lens case. With no lens, there is significantly more bleached volume than with the lens cases. The 25 cm lens resulted in a nearly linear increase in volume with distance and the 15 cm lens resulted in a much sharper increase in volume near the edges, which would more significantly skew the propagation data for the 15 cm lens.

This result suggested that using the 15 cm lens results in the smallest total bleached volume, which was not the case according to Figures 21 and 22, which showed that the 25 cm lens was the most effective lens for bleaching more distance in the cell. This indicated that the 15 cm lens was most likely not achieving as small a spot size as an ideal 15 cm lens could, probably a result of aberrations. Using these results for volume as a function of distance, the plots of the distance as a function of inverse density and power

for each of the lens configurations were converted into plots of total bleached volume instead of distance. The results for the no lens case were plotted in Figures 26 and 27 and the results for each of the lenses can be found in Appendix B.

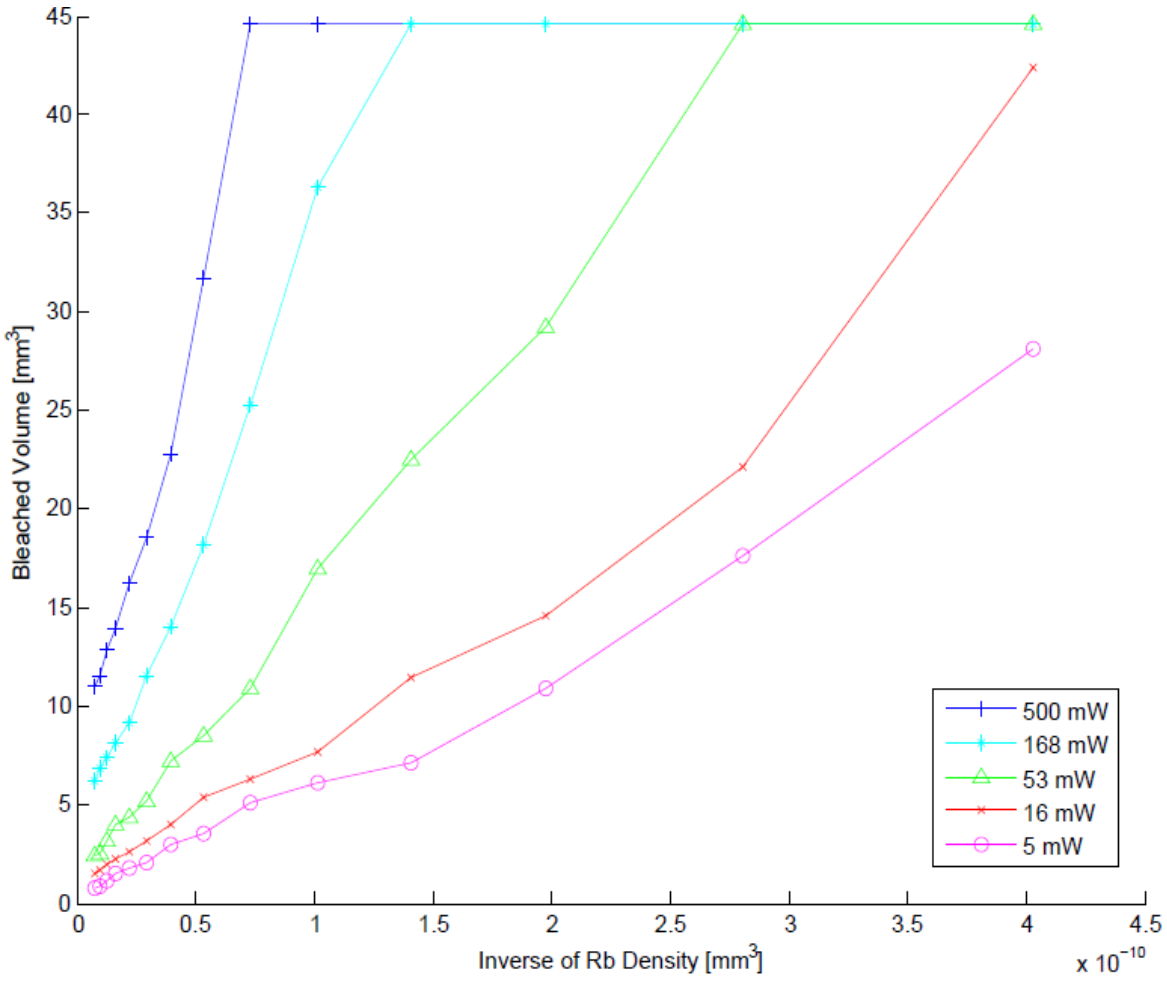

Fig. 26. The total bleached volume with respect to the inverse of rubidium vapor concentration for a system at various powers and using no lens. For beams that propagated through the entire cell, the horizontal limit was recorded as 50 mm, which corresponds to about 45 mm^3 bleached volume.

The bleached volume grew linearly with respect to the inverse of the rubidium vapor density. The change in area with respect to distance was almost uniform for the no

lens case, so Figure 26 was almost identical to Figure 19. Figure 27 indicated a similar result.

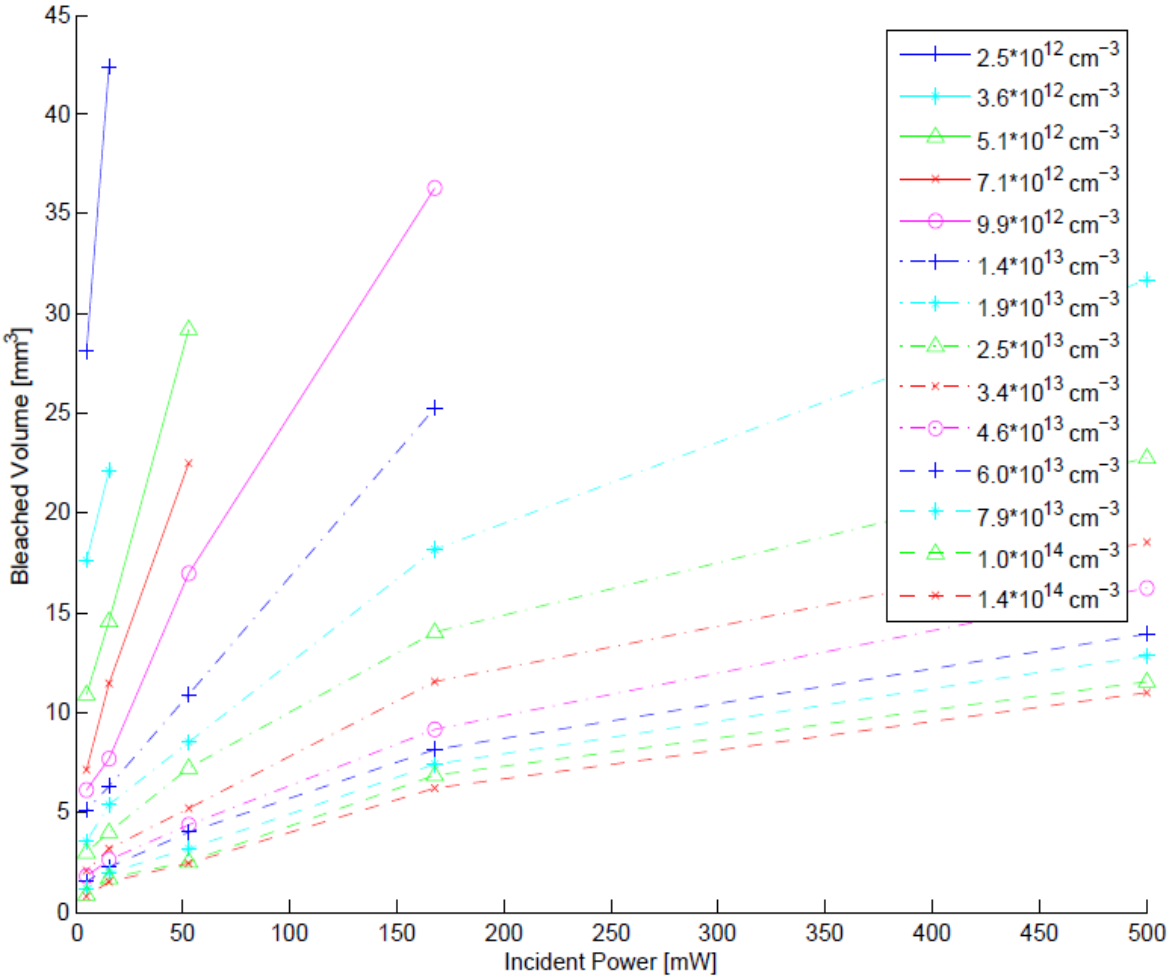

Fig. 27. The total bleached volume with respect to Matisse power for a system at various rubidium vapor concentrations and using no lens. Due to sharp propagation limit cutoffs at higher powers, the points where the pump laser bleached the entire cell were removed from the plot.

The distance versus bleached volume curves from Figure 25 for the no lens and 25 cm lens configurations were nearly linear, so their respective plots against inverse density and inverse power showed no significant change. The plots for the 15 cm case

became even less linear than before, indicating that the lens most likely could not focus the spot size to as small an area as the model predicted.

The data indicated that for the no lens case at 500 mW, the laser bleached a volume containing about 6×10^{11} Rb atoms. Theoretically, the Planck-Einstein relation and the spontaneous emission coefficient of rubidium indicated that at 500 mW, the laser only had enough power to bleach a volume containing 5×10^{10} Rb atoms. The most likely explanation for this discrepancy was that the temperature inside the Pyrex cell was lower than the temperature of the heater block, so the bleached volumes did not contain as many atoms as calculated. It was also possible that some of the regions that exhibited side fluorescence were not completely bleached, so despite a large observed region emitting radiation, there was only a small bleached volume.

With all the plots in terms of total bleached volume, the values for the different lens configurations could be compared with one another. The results for the lowest power in Figure 26 for each lens case were taken (so that all of the propagation distances would fall within the interior of the cell) and plotted in Figure 28, and the results for the highest density in Figure 27 for each lens case were taken (again, so that all of the propagation distances would fall within the interior of the cell) and plotted against one another in Figure 29.

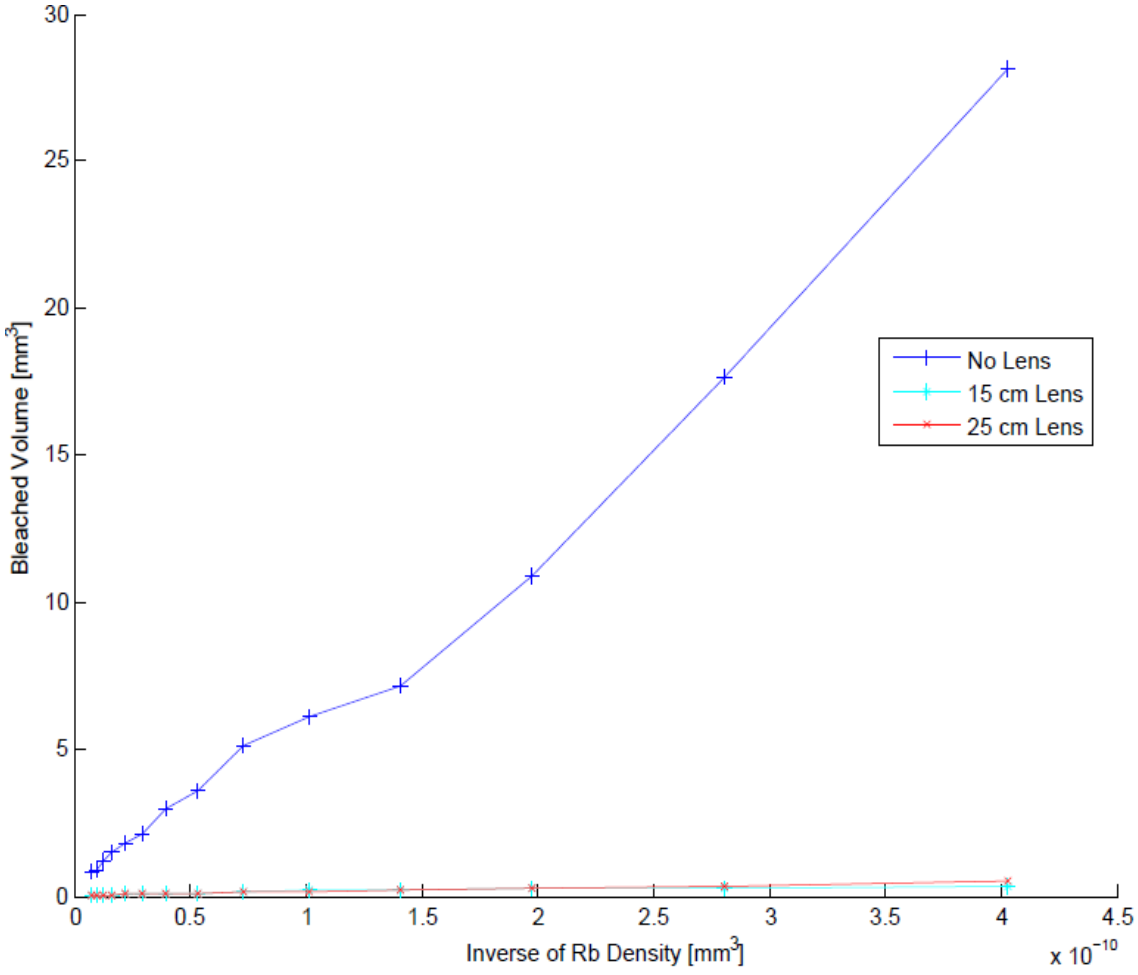

Fig. 28. The total bleached volume within the cell for a Matisse power of 5 mW as a function of the inverse of rubidium density for each of the lens trials.

The data suggested that the no lens case bleached around 40 times as much volume as the equivalent cases with either of the lenses. Figure 29 indicated a factor about half as large.

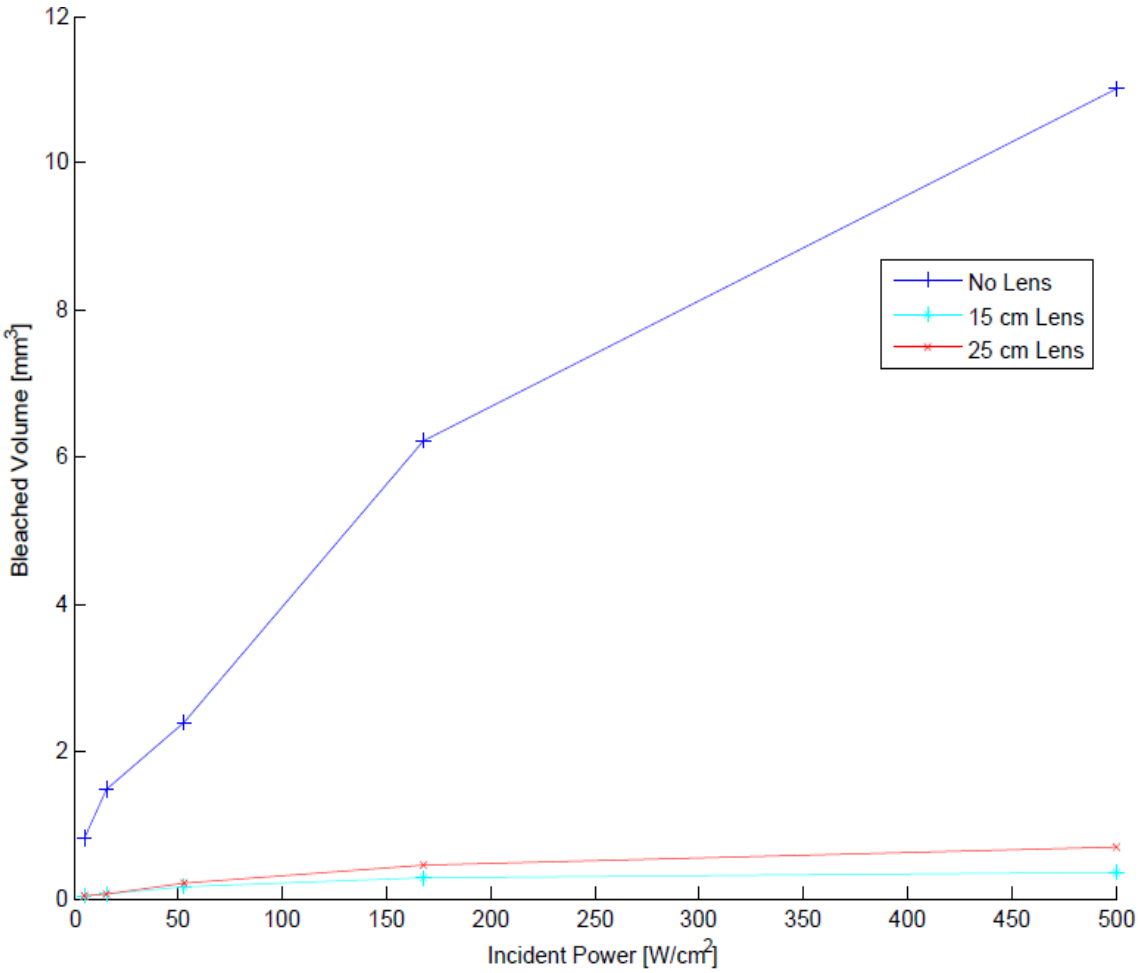

Fig. 29. The total bleached volume within the cell for a rubidium concentration of 1.4×10^{14} cm^{-3} as a function of the inverse of incident Matisse power for each of the lens trials.

The data suggested that the no lens case bleached around 20 times as much volume as the cases with the lenses. Visual confirmation of the images taken indicated that indeed more volume gave off side fluorescence when no lens was used. A possible explanation for these observations is that this model only took the intensity at beam center into account, when there is also radial dependence to consider; the beam diverges and is weaker at greater distances from the center, and the $w(z)$ approximation may not be valid in this case. Another possible explanation for these observations is that the regions

exhibiting side fluorescence were not always the same regions as those that were completely bleached, and to more closely determine the conditions under which bleaching occurs, the effects of changing the pump wavelength must be observed.

When the Matisse wavelength was changed, the propagation distance through the cell changed, indicating a change in saturation intensity. The propagation distance is plotted with respect to wavelength in Figure 30.

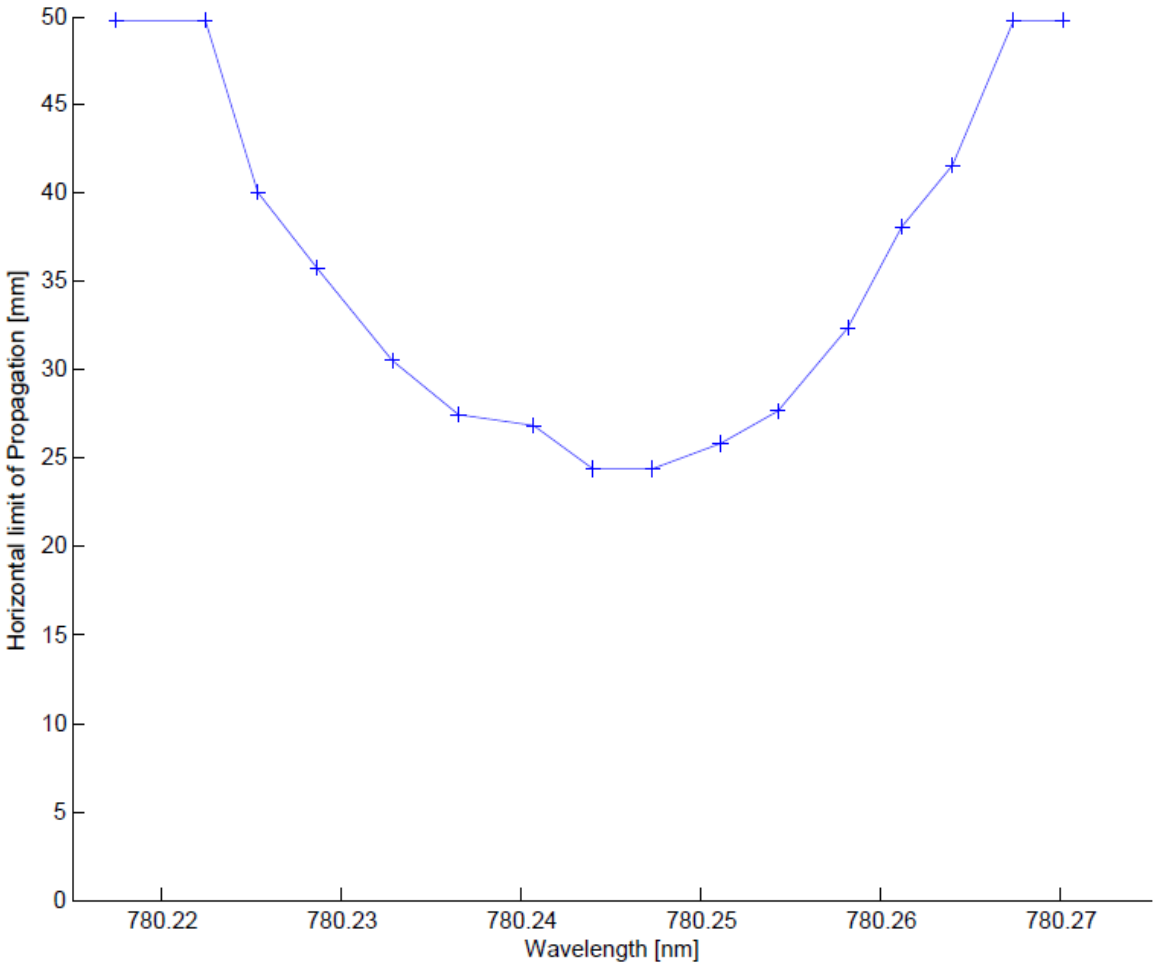

Fig. 30. The horizontal limit of beam propagation with respect to Matisse wavelength for a system at a rubidium concentration of 2.5×10^{13} cm^{-3}, a pump power of 500 mW, and using no lens. For beams that propagated through the entire cell, the horizontal limit was recorded as 50 mm.

These results suggested that the rate on average at which the laser intensity decreased as a function of horizontal propagation distance was higher at transition line center than off-center. Lewis's model indicated that in the bleached region of an absorption cell, the rate at which the intensity decreased would be constant with respect to the frequency (not including the linear variation with the frequency, which only changed by about 0.01% in this case). The intensity differential would only change once the intensity dropped closer to the saturation intensity and transitioned into the Beer's Law region [16]. In this case, there was visible side fluorescence in different regions when the frequency of the Matisse was adjusted; therefore, side fluorescence did not only occur in the bleached regions of the cell, but also in the transition region between the bleached portion and the Beer's Law portion. This provides an explanation for the excessively large volume exhibiting side fluorescence with the no lens case; not all of the volume exhibiting side fluorescence was completely bleached.

Figure 30 must be fit to a model to determine the conditions under which the rubidium vapor cell emitted side fluorescence with respect to laser intensity and saturation intensity. From Equation 2, I_{sat} is given by,

$$I_{sat} = \frac{h\nu A}{\sigma(\nu)} \tag{2}$$

and from Equation 3, the change in intensity of the beam with respect to horizontal distance as it propagates through the cell is given by,

$$\frac{dI}{dz} = \frac{-\sigma n I}{1 + I / I_{sat}} \tag{3}$$

indicating exponential decay for $I_{sat} >> I$ and linear decay for $I >> I_{sat}$. Using these equations, the saturation intensity with respect to wavelength in the cell used is plotted in Figure 31(a) and the intensity with respect to propagation distance at several different Matisse wavelengths is plotted in Figure 31(b).

(a)

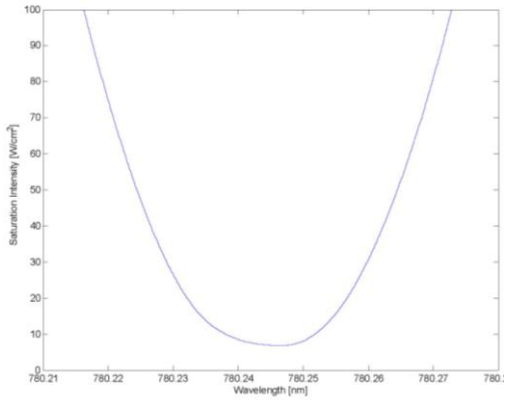

(b)

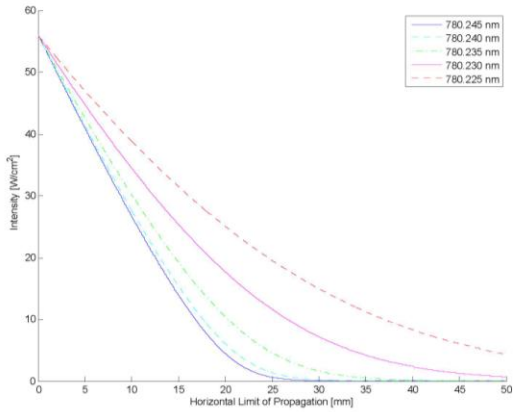

Fig. 31. Intensity and saturation intensity inside the rubidium Pyrex cell with neon buffer gas at 120°C. (a) The saturation intensity with respect to wavelength was proportional to the inverse of the absorption cross section (disregarding the 0.01% change in wavelength). (b) The intensity of the beam at I_0 = 56 W/cm^2 as it propagated through the cell for five different wavelengths. Taking the pressure shift into account, 780.245 nm was closest to line center and 780.225 nm was farthest from line center.

From Figure 31, at λ = 780.245 nm, I_{sat} was approximately 7 W/cm^2, so the intensity through the cell decreased linearly until it reached this point and then transitioned into exponential decay. I_{sat} became larger off line center, and the transition region between the bleached region and the Beer's Law region became much wider; at λ = 780.225 nm, the intensity was neither definitively linear nor exponential for the entire length of the cell.

The cell would not emit side fluorescence in a region determined by Beer's Law. Equation 3 became approximately exponential when I fell below I_{sat} by about an order of magnitude. A model was fit to Figure 30 for all the wavelengths and propagation distances at which $I > I_{sat}/8$ and the results were plotted alongside each other in Figure 32.

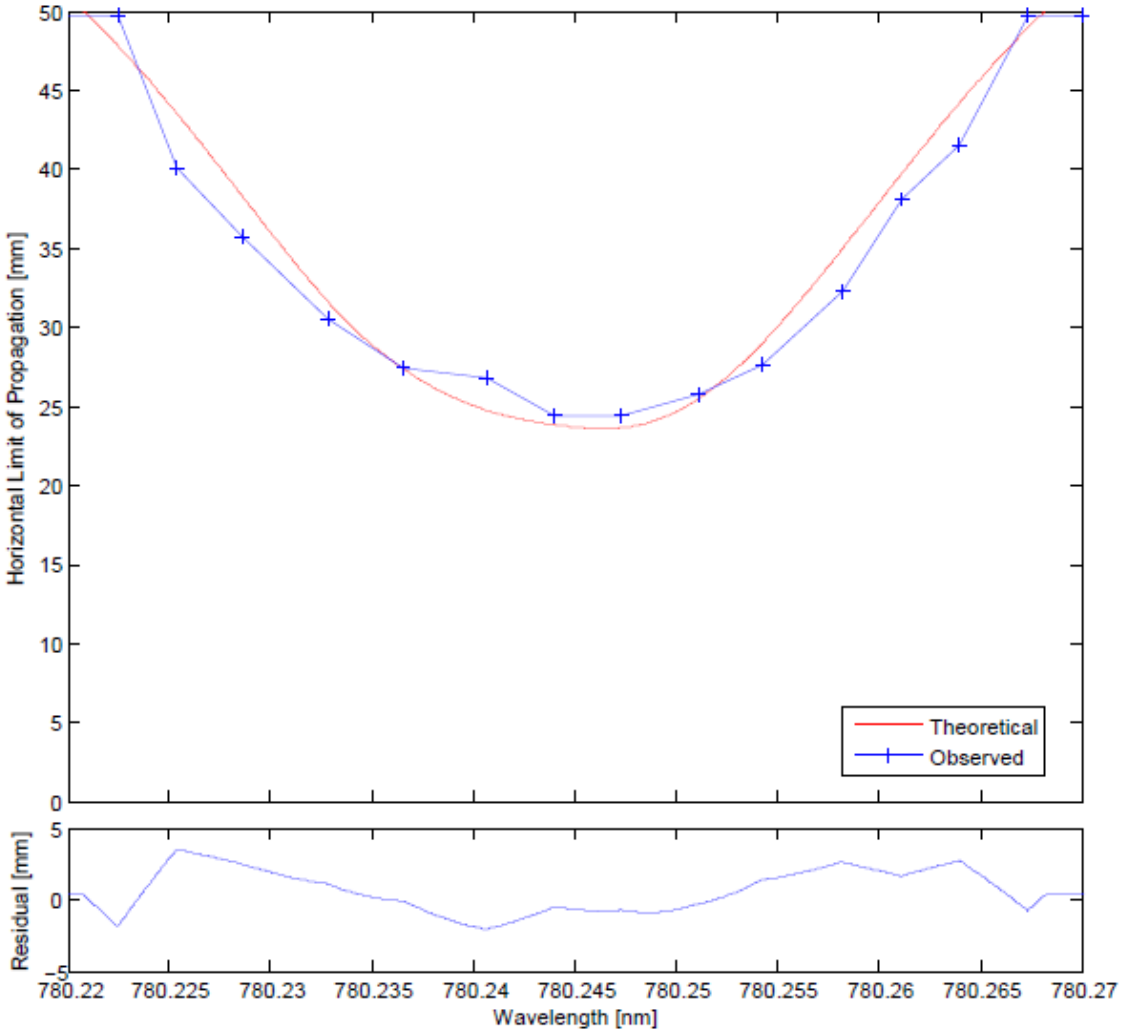

Fig. 32. The horizontal limit of beam propagation with respect to Matisse wavelength from Figure 30 plotted alongside a theoretical model for all the points in the cell at which I_{sat} was at least 8 times larger than I. In both, two distinct hyperfine components were observed at 780.24 nm and 780.245 nm.

The model fit the beam propagation data with an R^2 value of 0.9832, indicating that indeed the cell did not emit side fluorescence in the Beer's Law region and that the approximation $I = I_{sat}/8$ for the boundary of the Beer's Law region was accurate. It indicated a rubidium vapor concentration of 3.65×10^{12} cm^{-3}, which was approximately an order of magnitude lower than the vapor pressure formula suggested for rubidium at 120°C. Steck's rubidium vapor pressure curve indicated that the concentration at this temperature would be closer to 2.5×10^{13} cm^{-3} [9] [10], indicating that the cell was about 15°C colder than the thermocouple in the heater block. The previous results in study regarding the total number of possible bleached atoms also indicated that the temperature of the cell was lower than that of the heater block, and these results were plausible because the missing edge of the heater block allowed greater heat loss to the environment.

Data was collected with the same experimental apparatus using a cell with only the ^{87}Rb isotope and no buffer gas with a Manta G-609 camera. By observing the linear regions in the intensity curves and using linear fits in each frame to determine the distance at which the intensity reached zero, this value was used as the total bleached distance and is plotted with respect to pump wavelength for the $F'' = 1$ peak in Figure 33. The same algorithm used for Figure 32 was used to calculate the theoretical horizontal bleached distance, and the results indicated that the rubidium density in the cell was 2.45 $\times 10^{12}$ cm^{-3} with $R^2 = 0.9955$. In this case, for the method to yield an accurate fit, instead of designating a cutoff intensity proportional to I_{sat}, a constant value of 0.1 W/cm^2 was used. This method resulted in a higher R^2 value and a smoother curve than that of Figure 32.

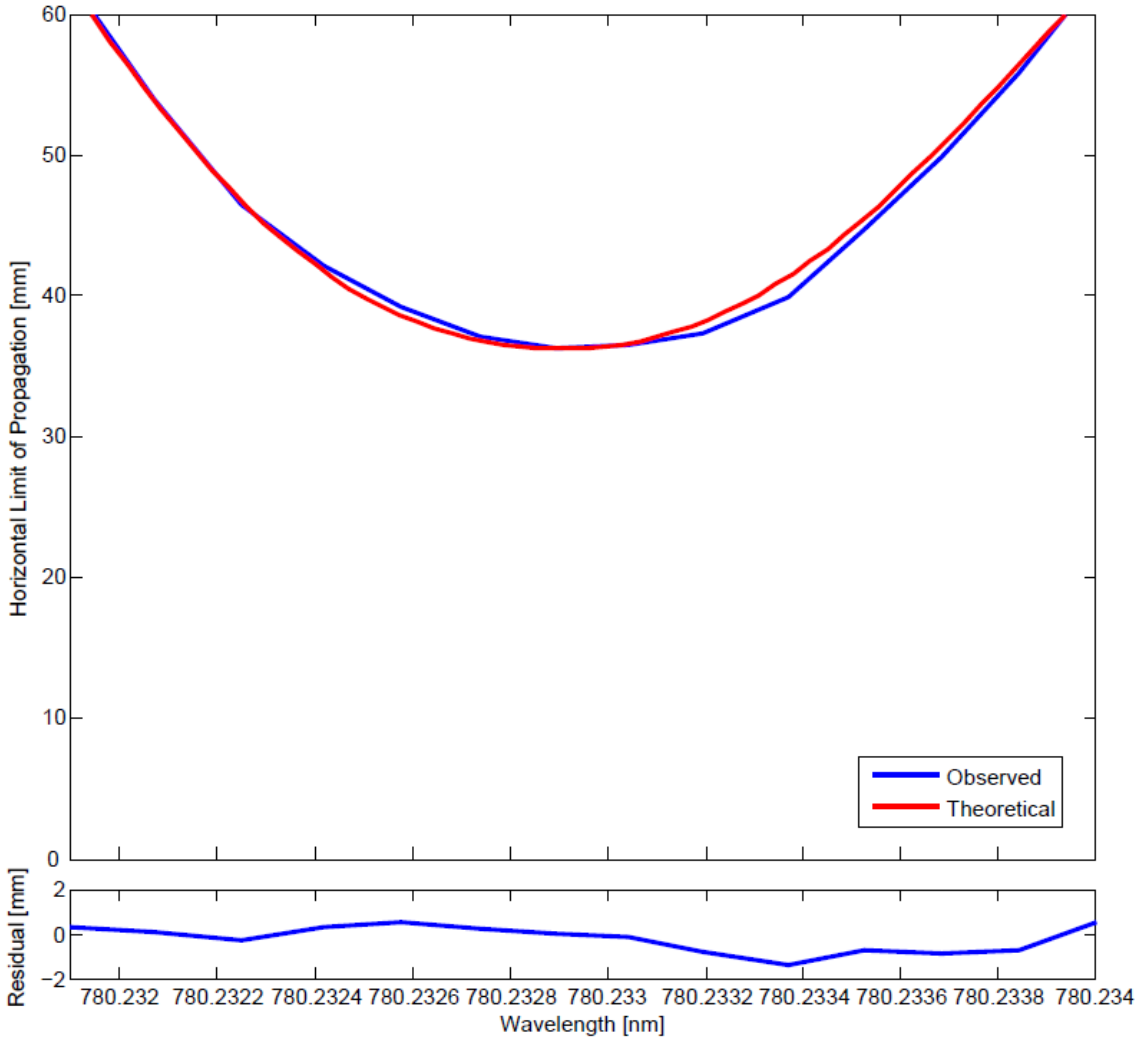

Fig. 33. The horizontal limit of beam propagation (extrapolated from the linear decrease in intensity of the bleached region) with respect to Matisse wavelength plotted alongside a theoretical model for all the points in the cell at which I_{sat} was at least 0.1 W/cm^2

The wavelength dependent propagation results indicated that when the cell was pumped with the laser at line center, there was a very brief, distinct transition between the bleached region and the Beer's Law Region. Therefore, if the entire length of the cell exhibited side fluorescence at this specific wavelength of 780.245 nm, the entire cell was bleached. The trial with the highest rubidium concentration in which the cell was entirely

bleached was the case with the Matisse at 500 mW with the 25 cm lens at 135°C, corresponding to an alkali metal vapor concentration of 6.0×10^{13} cm^{-3}. Assuming a sufficient spin-orbit relaxation rate, the population inversion for the three-level system would be 1.5×10^{13} cm^{-3}, which would indicate a gain of 21 cm^{-1} at line center. As this figure is far greater than the cavity losses, poor gain can be eliminated as an explanation as to why the rubidium cell did not lase when optically pumped.

For the system achieve the necessary population inversion and lase, the spin-orbit relaxation rate from the $^2P_{3/2}$ state to the $^2P_{1/2}$ state between the alkali metal and the buffer gas must be much larger than the spontaneous emission rate of the alkali metal from the $^2P_{3/2}$ state to the $^2S_{1/2}$ state. At 135°C, the spin-orbit relaxation rate coefficient of this transition between rubidium and neon was 2.231×10^{-14} cm^3/s [13], which indicated a spin-orbit relaxation rate of 0.3676 MHz for a cell with 500 torr Ne. The spontaneous emission rate of rubidium is 38.12 MHz, so not enough rubidium transitioned to the $^2P_{1/2}$ state to create a detectable level of radiation at the D_1 line. Replacing the 500 torr Ne with 500 torr He would have changed the spin-orbit relaxation rate to 23.21 MHz [13], which would also have been lower than the spontaneous emission rate. A previous study with only helium buffer gas had to use 2050 torr to achieve a DPAL with a slope efficiency of 20% [2].

Figure 30 bore a superficial resemblance to the pressure-broadened absorption spectrum of the cell. Dividing the absorption spectrum of the cell by the total length of the cell gave the absorbance per length in units of inverse millimeters. Taking the inverse of the propagation length also gave units of inverse millimeters, so both of these values

indicated absorbance per unit length. Both of these values were plotted together in Figure 34 in order to compare their respective FWHM values.

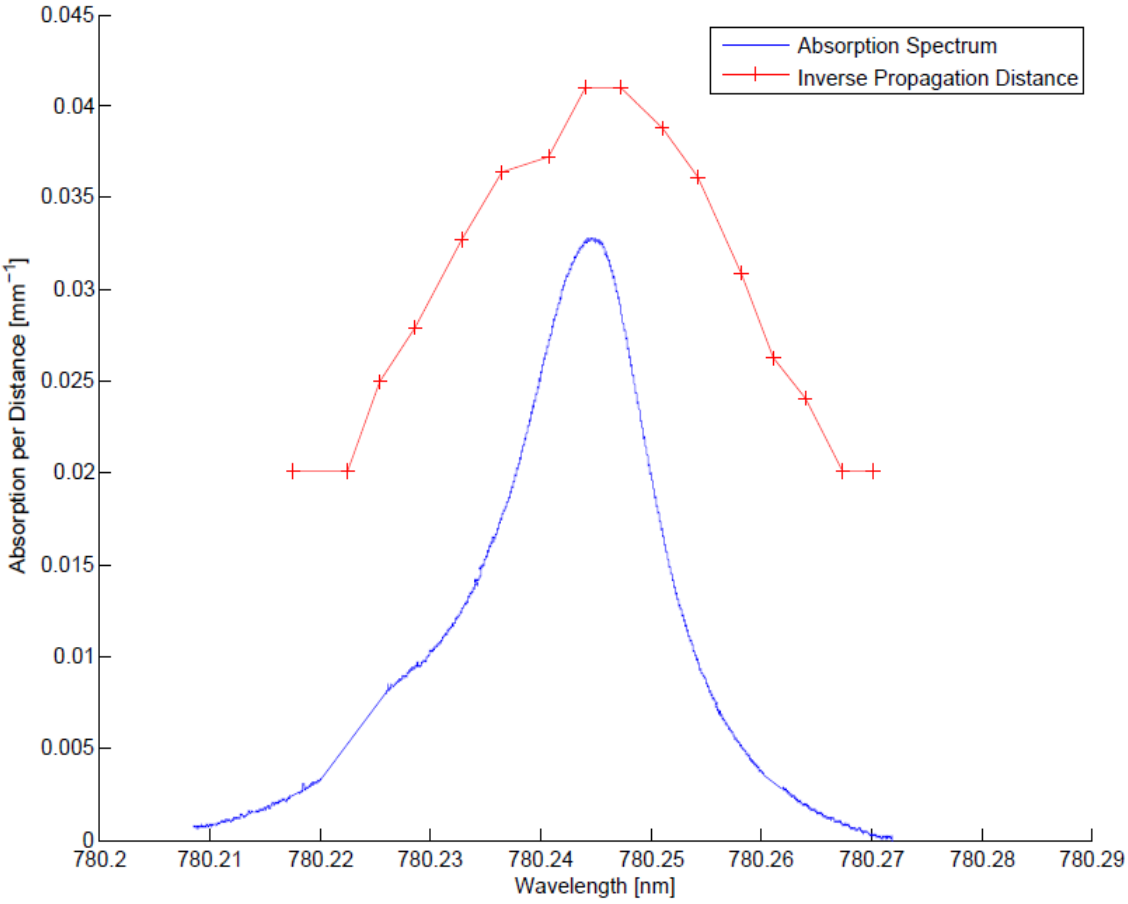

Fig. 34. The inverse of the horizontal stopping distance plotted in Figure 30 plotted alongside the absorption spectrum divided by cell length of the pressure-broadened rubidium sample at 50°C from Figure 15, for which the units of both come out to inverse millimeters. The FWHM of the stopping distance was approximately 3 times that of the absorption spectrum, which is consistent with the expected saturation broadening.

The pressure-broadened FWHM of the rubidium was approximately 0.012 nm. The rise in temperature from 50°C to 120°C would introduce an increase in pressure (and therefore pressure-broadening) proportional to the increase in absolute temperature, bringing the adjusted FWHM at 120°C to about 0.015nm. The plot of inverse propagation

distance indicated a FWHM value of approximately 0.045 nm, so the ratio between these two values was approximately 3. The minimum saturation intensity was about 5.6 W/cm^2 and the initial intensity at beam center with no lens was about 56 W/cm^2, giving S = 10 and the $(1 + S)^{1/2}$ saturation broadening factor about 3.3, which is consistent with the ratio between the saturated and unsaturated FWHM values. These results confirm that there was bleaching at the beginning of the cell before the intensity dropped into the Beer's Law region.

Conclusions

The cell parameters of this study matched those of the previous studies, but no radiation in the output beam at the Rb D_1 795 nm was observed, due to the fact that neon was a poor buffer gas. Other studies used gases with very high spin orbit relaxation rates, such as hydrocarbons, or used much higher pressures of rare gases.

The comparison of the wavelength dependent propagation distance and the pressure-broadened absorption spectrum confirm that bleaching and saturation broadening occurred. Therefore, the cell was bleached at high pump intensity and had the buffer gas been a viable spin-orbit relaxation partner at a sufficient pressure, the gain would have been around 21 cm^{-1}, easily enough to lase with only one or two passes through the cell.

The discrepancy between the observed total bleached volumes of the cell with and without a lens placed before the beam suggest that a stricter indicator of bleaching is necessary before an observation can be recorded as such. Both the model for the bleached volume based on the horizontal propagation length and observation of the images

indicated that for samples taken with identical beam power and rubidium vapor density, at least 10 times as much volume exhibited side fluorescence when no lens was used. The wavelength dependent scan in Figure 30 indicated that not every region that exhibited side fluorescence was completely bleached. A future study should obtain a data set of side fluorescence brightness in a cell as a function of intensity to compare against the calculated saturation intensity for each wavelength.

The data suggested that for a given laser power, far more atoms were bleached than that power should have been able to bleach, by about an order of magnitude. Either the observed bleached volume was larger than the actual bleached volume as indicated by Figure 30, the calculated rubidium vapor density was higher than the actual density, or some combination of both these factors. The temperature and therefore the rubidium concentration were much lower due to the use of the open heater block, which introduced a large disparity between the temperature of the thermocouple in the heater block and the temperature of the Pyrex cell. This allowed a temperature loss of 15^{o}C, which is great enough to account for such a change in concentration. This would not have prevented a laser from being demonstrated had there been an adequate buffer gas, as a wide enough range of high temperatures were used, and even if there were an offset in the rubidium vapor density for an expected input temperature, Figure 19 indicated that the rubidium vapor densities still scaled linearly as the temperature increased, so the desired rubidium vapor density would have been achieved at a point at which the thermocouple read 15^{o}C hotter.

The nonlinearity in the curves for propagation distance with respect to power indicated that the $w(z)$ model was not sufficient to describe this system. A future study

should develop a more rigorous model able to map the beam radius for each lens at each point in the cell. Such a model would have to calculate the intensity from the radial dependence from Maxwell's equations for each case to determine the beam's propagation.

To determine the intensity at each point in a cell for each lens configuration, a future study concerning rubidium cell bleaching should make an attempt to obtain a more accurate data set of the shape of the total bleached volume, and determine a numerical value for intensity of a given point based on the image. Capturing adequate images in which pixel index is proportional to side fluorescence intensity still poses issues; any transparent cell filled with heated alkali metal will have precipitates form on the windows. A study to obtain this better data set would have to be focused on data analysis and building a program with robust code capable of sorting out window contamination and radiation scattering to return the shape of the bleached volume. Such a study should also attempt to determine the intensity threshold at which a region in an absorption cell would stop exhibiting side fluorescence, and the linear rate at which the intensity decreases as the beam propagates through the cell. Once these values are determined, there will be an explanation for the greater loss of intensity at higher powers in a DPAL cell.

Appendix A: Tables

Table 1. Vacuum wavelengths for each rubidium D_2 hyperfine transition [9] [10]

Transition	*λ (nm)*
^{85}Rb F'' = 3 → F' = 2	780.24411
^{85}Rb F'' = 3 → F' = 3	780.24398
^{85}Rb F'' = 3 → F' = 4	780.24373
^{85}Rb F'' = 2 → F' = 1	780.23800
^{85}Rb F'' = 2 → F' = 2	780.23794
^{85}Rb F'' = 2 → F' = 3	780.23781
^{87}Rb F'' = 2 → F' = 1	780.24688
^{87}Rb F'' = 2 → F' = 2	780.24656
^{87}Rb F'' = 2 → F' = 3	780.24602
^{87}Rb F'' = 1 → F' = 0	780.23315
^{87}Rb F'' = 1 → F' = 1	780.23300
^{87}Rb F'' = 1 → F' = 2	780.23268

Table 2. Parameters of Various Rubidium DPAL Systems Compared Against Those of this Study

Parameter	Krupke [1]	Wu [2]	Zhdanov [14]	This Study
Temperature	120°C	170°C	105°C	70-150°C
Rb Concentration	1.7×10^{13} cm^{-3}	2.2×10^{14} cm^{-3}	1.9×10^{13} cm^{-3}	$\leq 1.4\times10^{14}$ cm^{-3}
Pump Power	500 mW	2.7 W	17.5 W	1.4 W
Spot Diameter	400 µm	220 µm	500 µm	200 µm
Intensity	100 W/cm^2	1.8 kW/cm^2	2 kW/cm^2	1 kW/cm^2
Buffer Gas(es)	75 torr ethane 525 torr helium	2050 torr helium	600 torr ethane	500 torr neon
Slope Efficiency	54%	21%	60%	N/A

Appendix B: Additional Figures

Additional data was taken with respect to rubidium density and pump power for lenses with focal lengths of 15 cm and 25 cm. Figures 35 through 40 correspond to Figures 18 through 20 for the horizontal propagation trials with no lens, and Figures 41 through 44 correspond to Figures 26 and 27 for the total bleached volume trials with no lens. These data sets are not as linear as the trials taken with no lens, but the plots are included in this appendix as a reference.

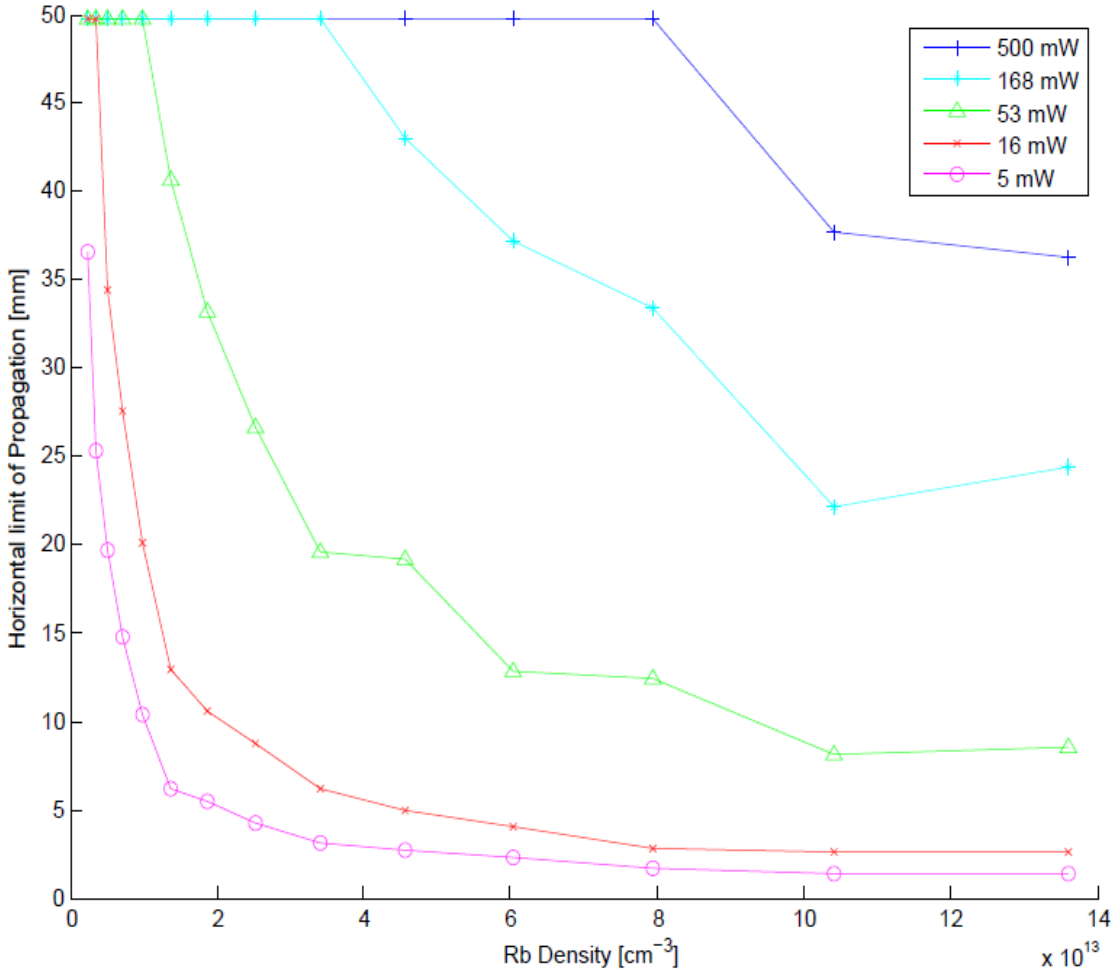

Fig. 35. The horizontal limit of beam propagation with respect to rubidium vapor concentration for a system at various powers and using a 15 cm lens.

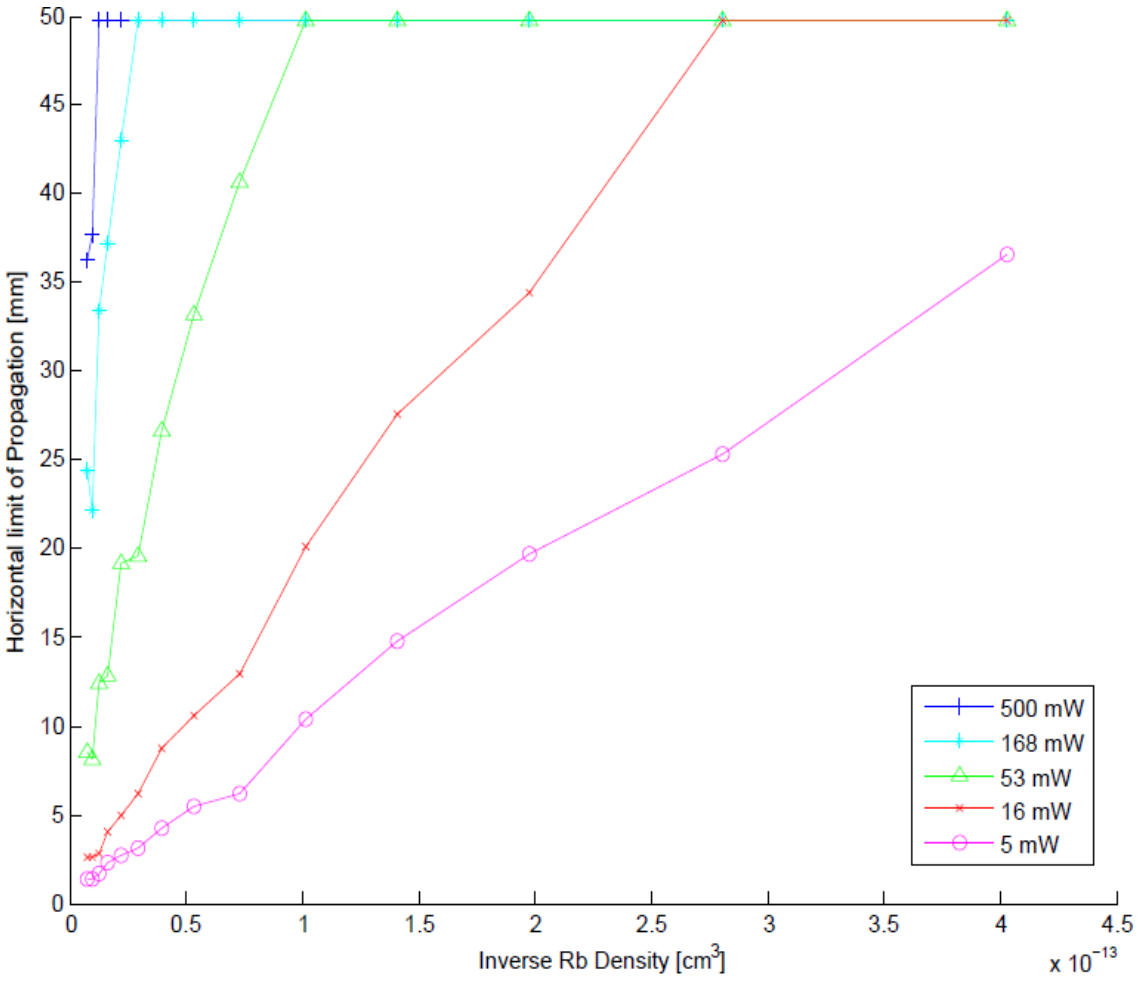

Fig. 36. The horizontal limit of beam propagation with respect to the inverse of rubidium vapor concentration for a system at various powers and using a 15 cm lens.

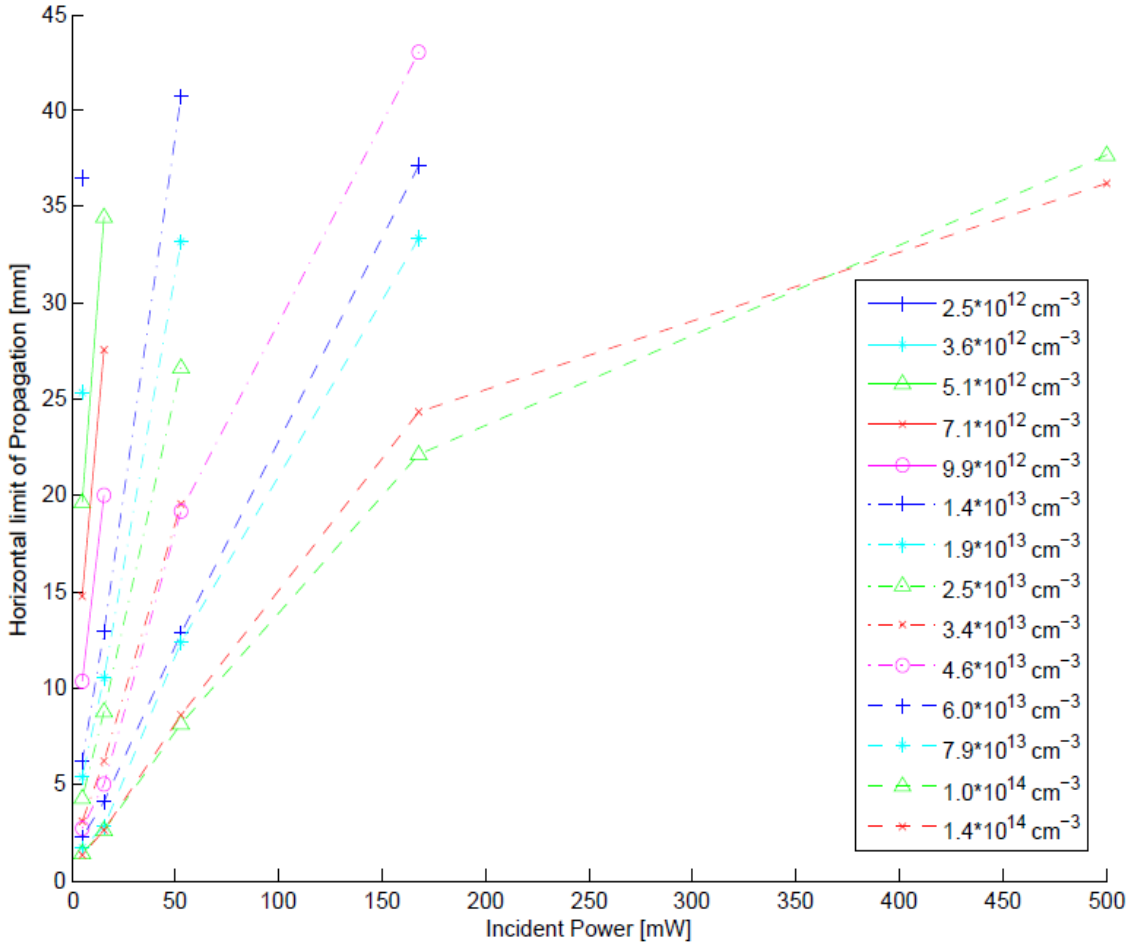

Fig. 37. The horizontal limit of beam propagation with respect Matisse power for a system at various rubidium concentrations and using a 15 cm lens.

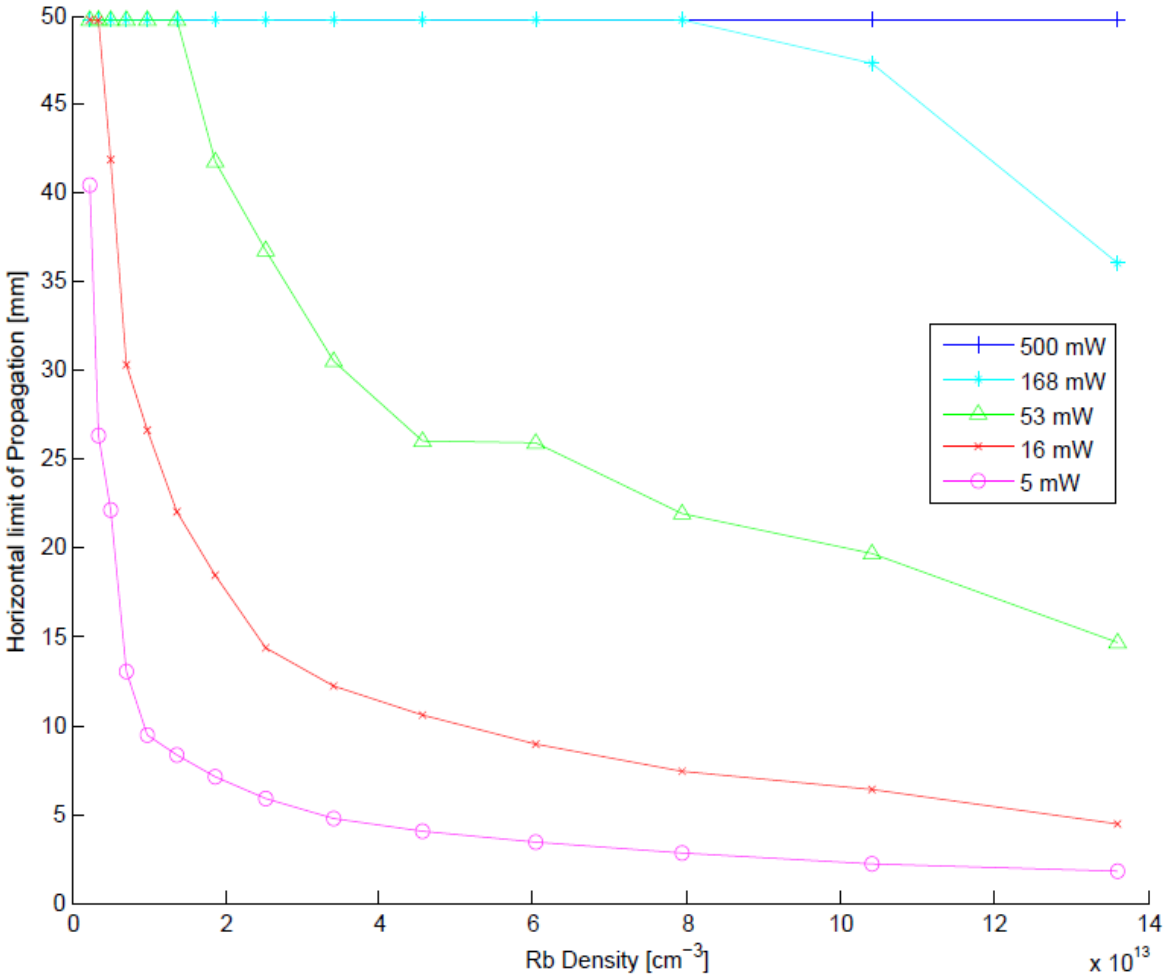

Fig. 38. The horizontal limit of beam propagation with respect to rubidium vapor concentration for a system at various powers and using a 25 cm lens.

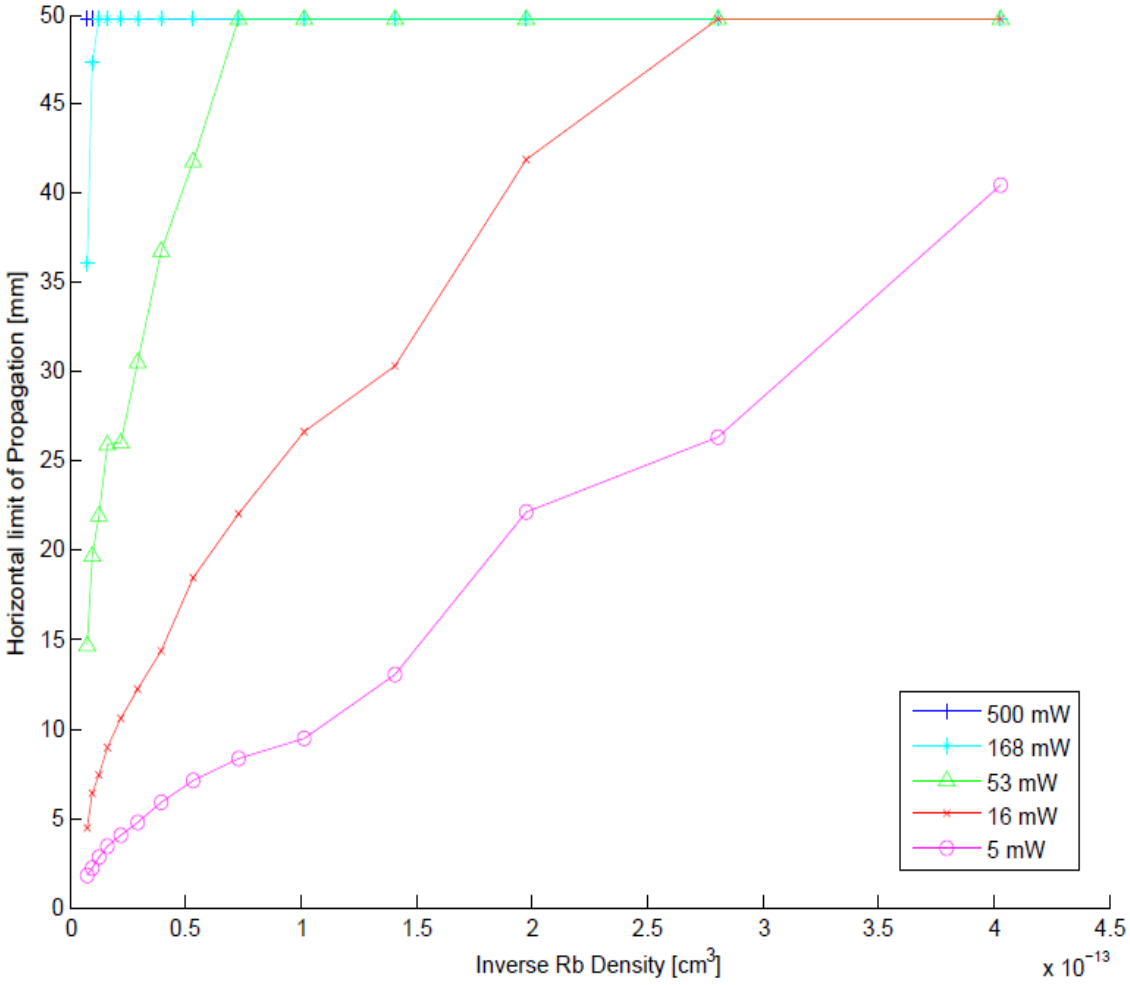

Fig. 39. The horizontal limit of beam propagation with respect to the inverse of rubidium vapor concentration for a system at various powers and using a 25 cm lens.

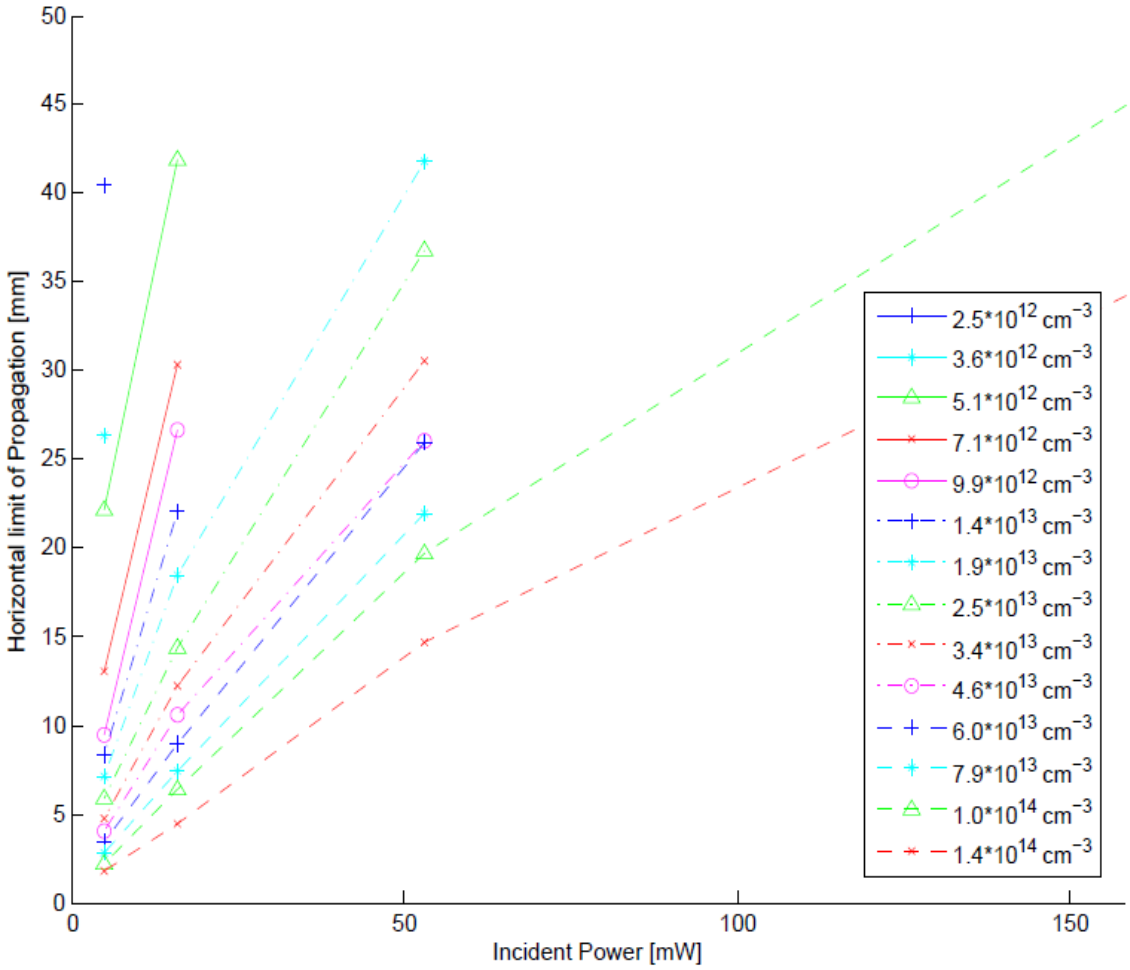

Fig. 40. The horizontal limit of beam propagation with respect to Matisse power for a system at various rubidium vapor concentrations and using a 25 cm lens.

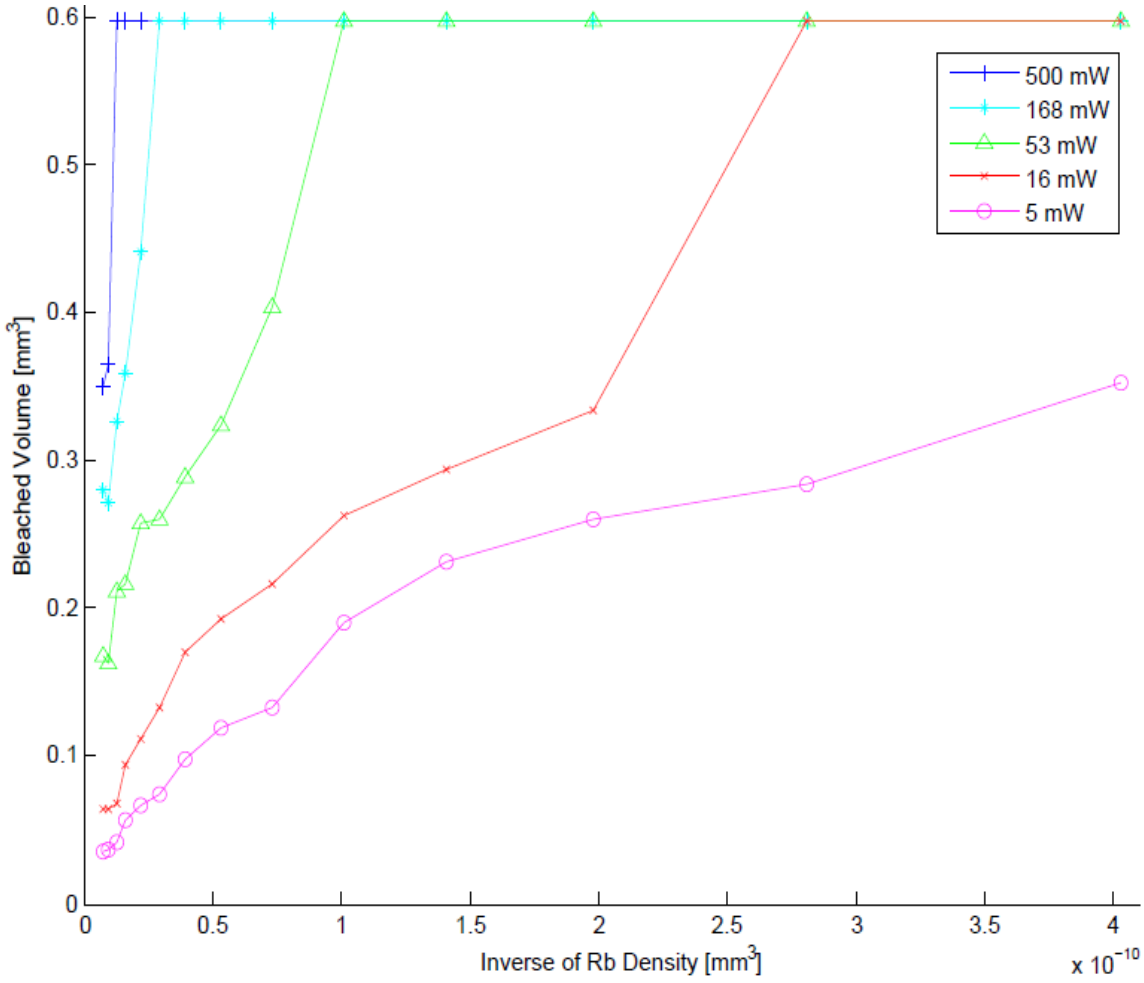

Fig. 41. The total bleached volume with respect to the inverse of rubidium vapor concentration for a system at various powers and using a 15 cm lens.

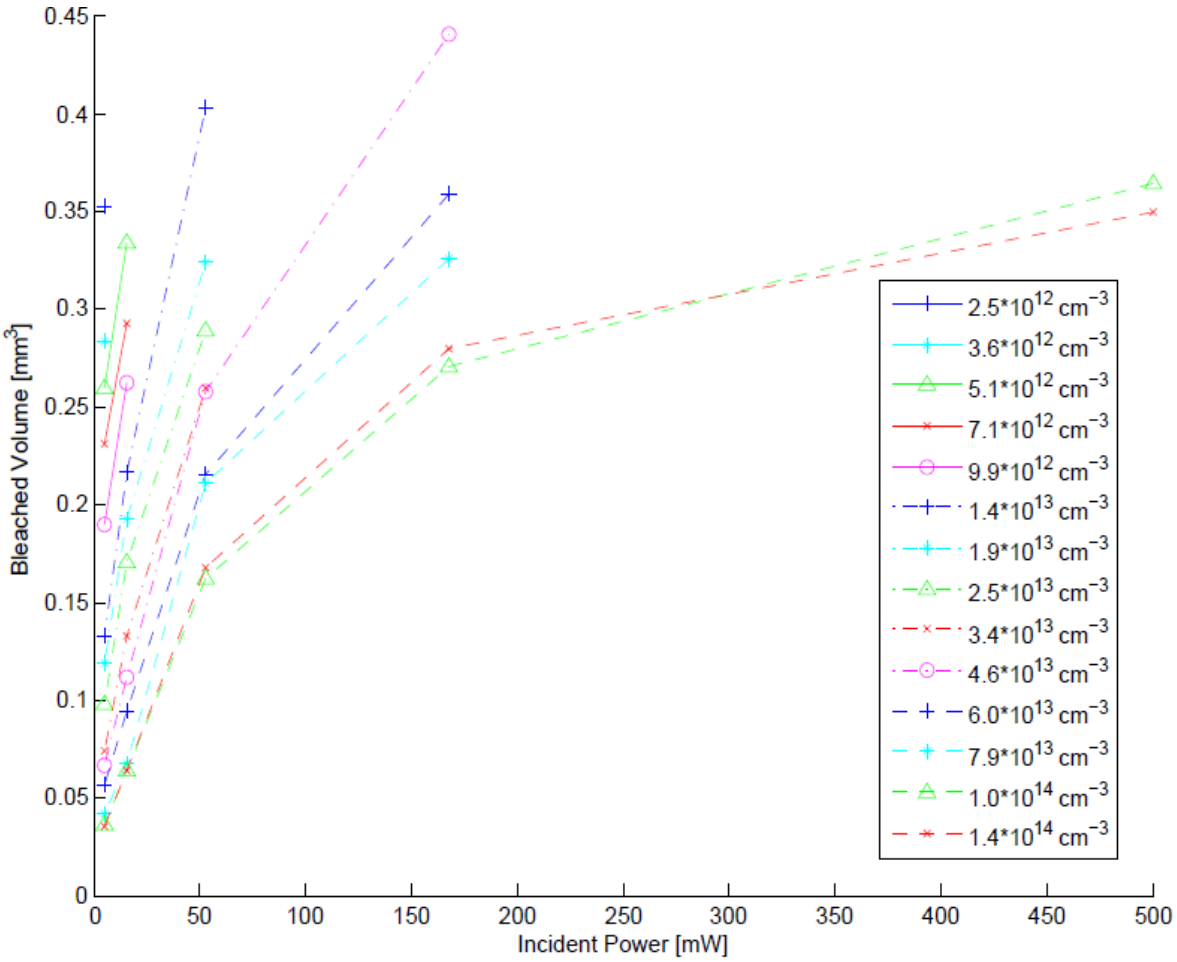

Fig. 42. The total bleached volume with respect to Matisse power for a system at various rubidium vapor concentrations and using a 15 cm lens.

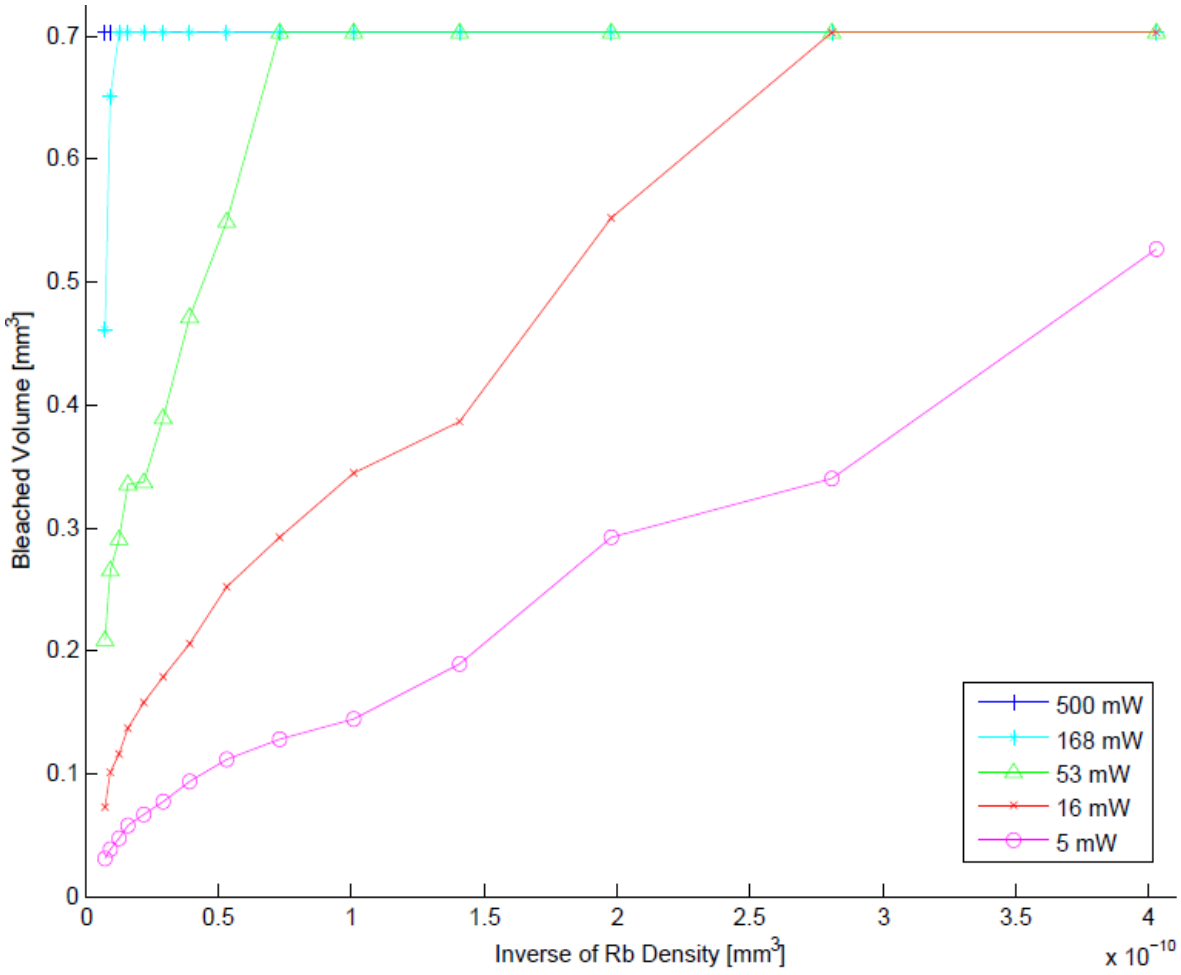

Fig. 43. The total bleached volume with respect to the inverse of rubidium vapor concentration for a system at various powers and using a 25 cm lens.

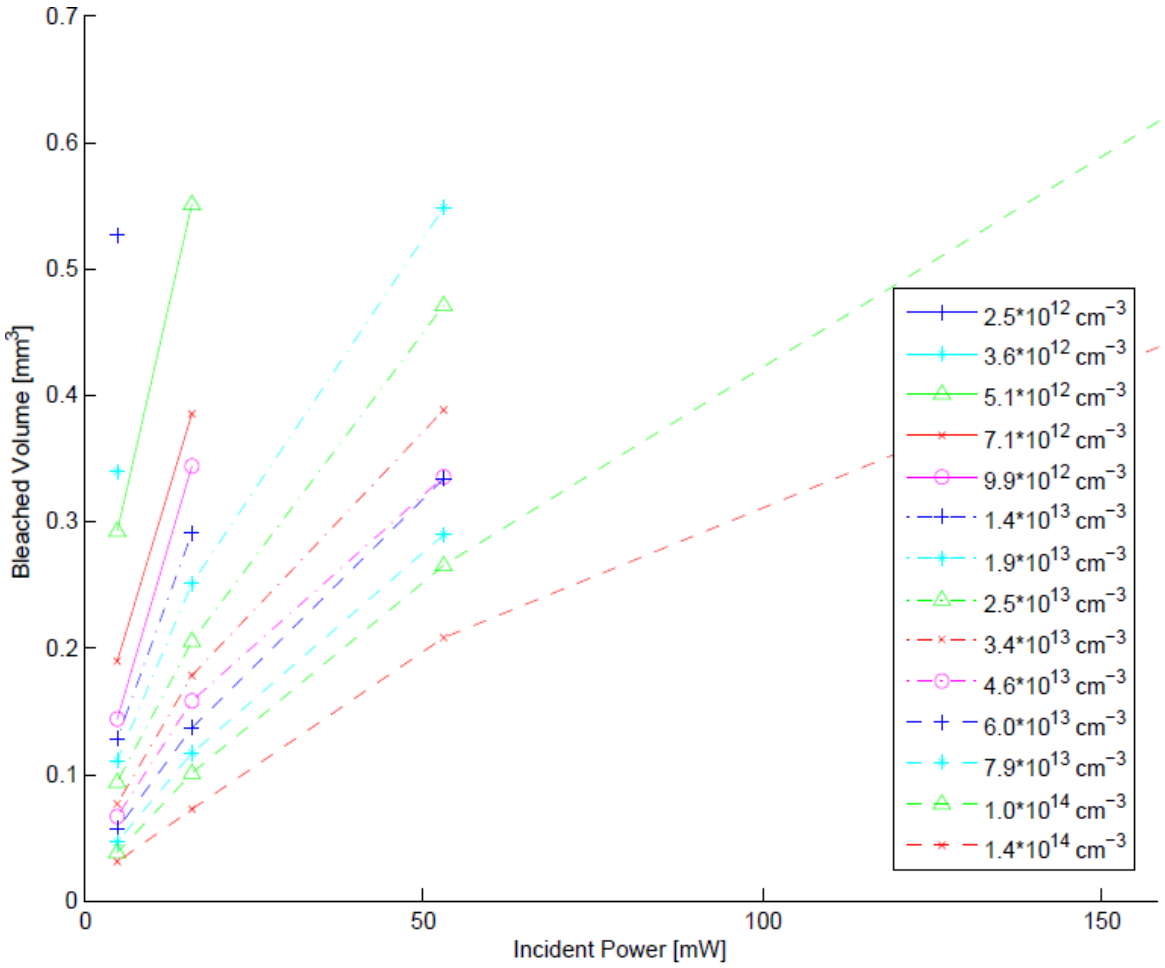

Fig. 44. The total bleached volume with respect to Matisse power for a system at various rubidium vapor concentrations and using a 25 cm lens.

Appendix C: Constants and Variables Used

Symbol	Quantity	Units
λ	Wavelength	[nm]
v	Frequency	[s^{-1}]
g_J	Electronic Angular Momentum Degeneracy	(unitless)
A	Spontaneous Emission Einstein Coefficient	[s^{-1}]
$S_{F''\rightarrow F'}$	Hyperfine Line Strength	(unitless)
$g(v)$	Lineshape	[s]
f_{iso}	Relative Natural Isotope Abundance	(unitless)
$f_{F''}$	Distribution of Ground F States	(unitless)
n	Concentration	[(particles)/cm^3]
γ_L	Pressure-Broadening Coefficient	[MHz/torr]
δ	Pressure Shift Coefficient	[MHz/torr]
z	Horizontal Distance	[mm]
I	Intensity	[W/cm^2]
I_{sat}	Saturation Intensity	[W/cm^2]
σ	Absorption Cross Section	[cm^2]
h	Planck Constant	[J-s]
P_0	Incident Power	[W]
w	Beam Radius	[mm]
S	I to I_{sat} ratio	(unitless)

Appendix D: Abbreviations Used

- FWHM: Full Width at Half Maximum
- CW: Continuous Wave
- DPAL: diode pumped alkali laser
- AMD: alkali metal dispenser
- ABL: Airborne Laser
- Ti:Sapph: Titanium Sapphire
- SNR: Signal-to-Noise Ratio
- ND: Neutral Density

References

[1] W. F. Krupke, R. J. Beach, V. K. Kanz, and S. A. Payne, "Resonance Transition 795-nm Rubidium Laser," Opt. Lett. **28**, 2336-2338 (2003).

[2] S. S. Q. Wu, T. F. Soules, R. H. Page, S. C. Mitchell, V. K. Kanz, and R. J. Beach, "Resonance Transition 795-nm Rubidium Laser using He Buffer Gas," Proc. of SPIE **7005**, 700523-1 (2008).

[3] C. V. Sulham, "Laser Demonstration and Performance Characterization of Optically Pumped Alkali Laser Systems", PhD Dissertation, Air Force Institute of Technology (2010).

[4] P. della Porta, C. Emili, and S. J. Hellier, "Alkali Metal Generation and Gas Evolution from alkali metal dispensers", IEEE Technical Report TR 18 (1968).

[5] A. L. Eichenbaum and M. E. Moi, "Cesium Vapor Dispenser", Rev. of Sci. Inst. **35**. (1964).

[6] K. L. Moore, T. P. Purdy, K. W. Murch, S. Leslie, S. Gupta, and D. M. Stamper-Kurn, "Collimated, Single-Pass Atom Source from a Pulsed alkali metal dispenser for Laser-Cooling Experiments", Rev. of Sci. Inst. **76**. 023106 (2005).

[7] P. F. Bernath, *Spectra of Atoms and Molecules.* New York, Oxford University Press (2003).

[8] G. A. Pitz and G. P. Perram, "Pressure Broadening of the D1 and D2 lines in Diode Pumped Alkali Lasers", Proc. of SPIE **7005** 700526-7 (2008).

[9] D. A. Steck, "Rubidium 85 D Line Data," available online at http://steck.us.alkalidata (revision 2.1.6, 20 September 2013).

[10] D. A. Steck, "Rubidium 87 D Line Data," available online at http://steck.us.alkalidata (revision 1.6, 14 October 2003).

[11] M. D. Rotondaro and G. P. Perram, "Collisional Broadening and Shift of the Rubidium D_1 and D_2 Lines ($5^2S_{1/2} \rightarrow 5^2P_{1/2}$, $5^2P_{3/2}$) by Rare Gases, H_2. D_2, N_2, CH_4 and CF_4", J. Quant. Spectrosc. Radiat. Transfer. **57**. 497-507 (1997).

[12] R. Calder and G. Lewin, "Reduction of Stainless-Steel Outgassing in Ultra-High Vacuum", Brit. J. Appl. Phys. **18**. 1459-1472 (1967).

[13] A. Gallagher, "Rubidium and Cesium Excitation Transfer in Nearly Adiabatic Collisions with Inert Gases", Phys. Rev. **172**. 88-96 (1968).

[14] B. V. Zhdanov, A. Stooke, G. Boyadjian, A. Voci, and R. J. Knize, "Laser Diode Array Pumped continuous wave Rubidium Vapor Laser", Opt. Exp. **16.** 751 (2008).

[15] W. Demtröder, *Laser Spectroscopy: Basic Concepts and Instrumentation.* Berlin, Springer-Verlag (2003).

[16] C. D. Lewis, "A Theoretical Model Analysis of Absorption of a Three Level Diode Pumped Alkali Laser", Master's Thesis, Air Force Institute of Technology (2009).

REPORT DOCUMENTATION PAGE

Form Approved
OMB No. 0704-0188

1. REPORT DATE *(DD-MM-YYYY)*	**2. REPORT TYPE**	**3. DATES COVERED** *(From - To)*
26-03-2015	Master's Thesis	June 2014 - March 2015

4. TITLE AND SUBTITLE
Absorption Spectroscopy of Rubidium in an Alkali Metal Dispenser Cell and Bleached Wave Analysis

5a. CONTRACT NUMBER

5b. GRANT NUMBER

5c. PROGRAM ELEMENT NUMBER

6. AUTHOR(S)
Rosenthal, James M, 2d Lt, USAF

5d. PROJECT NUMBER

5e. TASK NUMBER

5f. WORK UNIT NUMBER

7. PERFORMING ORGANIZATION NAME(S) AND ADDRESS(ES)
Air Force Institute of Technology
Graduate School of Engineering and Management (AFIT/ENP)
2950 Hobson Way
WPAFB OH 45433-7765

8. PERFORMING ORGANIZATION REPORT NUMBER
AFIT-ENP-MS-15-M-102

9. SPONSORING/MONITORING AGENCY NAME(S) AND ADDRESS(ES)
Dr. Harro Ackermann
Senior Technical Advisor
HEL Joint Technology Office
801 University Blvd. SE, Suite 209
Albuquerque, NM 87106
505-248-8208 / harro.ackermann@jto.hpc.mil

10. SPONSOR/MONITOR'S ACRONYM(S)
HEL-JTO

11. SPONSOR/MONITOR'S REPORT NUMBER(S)

12. DISTRIBUTION/AVAILABILITY STATEMENT
DISTRIBUTION STATEMENT A. APPROVED FOR PUBLIC RELEASE; DISTRIBUTION UNLIMITED

13. SUPPLEMENTARY NOTES
This material is declared a work of the U.S. Government and is not subject to copyright protection in the United States

14. ABSTRACT

An absorption spectrum of a rubidium alkali metal dispenser (AMD) cell was obtained in order to determine the system's suitability for use in a diode pumped alkali laser (DPAL) and use in high-temperature spectroscopic studies. The AMD produced a concentration of $3.65 \pm 0.16 \times 10^{10}$ cm^{-3}, which is in the ideal range for Beer's Law region absorption spectroscopy, but too low to make a high-power DPAL in a 10 cm cell with a poor Q resonator. Before AMDs can be used to determine pressure broadening and shifting coefficients, issues concerning contamination and producing rubidium vapor at pressure must be resolved. A separate portion of this study focused on a sealed rubidium Pyrex cell with neon buffer gas. A continuous wave titanium sapphire beam was focused into the cell with various lenses to maximize pump intensity through the cell. Images were taken of the side fluorescence of the cell to determine the bleached regions. The total horizontal propagation of the bleached region for each image was proportional to the pump laser power and the inverse of the rubidium vapor density. Disparity between the bleached volume estimated from the beam parameters and the theoretical bleached volume suggested the beam intensity had a strong radial dependence. When the pump wavelength was changed, visible side fluorescence occurred in regions where the laser intensity was at least 0.125 times the saturation intensity and therefore not in the regions where the decay was determined by Beer's Law.

15. SUBJECT TERMS
Diode Pumped Alkali Laser, Alkali Metal Dispenser, Rubidium, Bleaching

16. SECURITY CLASSIFICATION OF:			**17. LIMITATION OF ABSTRACT**	**18. NUMBER OF PAGES**	**19a. NAME OF RESPONSIBLE PERSON**
a. REPORT	**b. ABSTRACT**	**c. THIS PAGE**			Dr. Glen Perram – ENP
U	U	U	UU	91	**19b. TELEPHONE NUMBER** *(Include area code)*
					(937) 255-3636 Ext. 4504